

UNIVERSITÀ DEGLI STUDI DI BOLOGNA

---

SCUOLA DI DOTTORATO DI INGEGNERIA INDUSTRIALE  
Dottorato in Meccanica e Scienze Avanzate dell' Ingegneria:  
Ingegneria delle Macchine e dei Sistemi Energetici – XXV ciclo  
09/C1 ING/IND-08

Dipartimento di Ingegneria Industriale

Tesi di Dottorato in Motori a Combustione Interna

A NUMERICAL  
METHODOLOGY FOR THE  
MULTI-OBJECTIVE  
OPTIMIZATION OF THE DI  
DIESEL ENGINE COMBUSTION

**Dott. Ing. Marco Costa**

Tutore  
Chiar.mo Prof. Ing. Piero Pelloni

Coordinatore del corso di dottorato  
Chiar.mo Prof. Ing. Vincenzo Parenti Castelli

---

TRIENNIO 2009-2012



# Abstract

DI Diesel engine are widely used both for industrial and automotive applications due to their durability and fuel economy. Nonetheless, increasing environmental concerns force that type of engine to comply with increasingly demanding emission limits, so that, it has become mandatory to develop a robust design methodology of the DI Diesel combustion system focused on reduction of soot and NO<sub>x</sub> simultaneously while maintaining a reasonable fuel economy. In recent years, genetic algorithms and CFD three-dimensional combustion simulations have been successfully applied to that kind of problem. However, combining GAs optimization with actual CFD three-dimensional combustion simulations can be too onerous since a large number of calculations is usually needed for the genetic algorithm to converge, resulting in a high computational cost and, thus, limiting the suitability of this method for industrial processes. In order to make the optimization process less time-consuming, CFD simulations can be more conveniently used to generate a training set for the learning process of an artificial neural network which, once correctly trained, can be used to forecast the engine outputs as a function of the design parameters during a GA optimization performing a so-called virtual optimization.

In the current work, a numerical methodology for the multi-objective virtual optimization of the combustion of an automotive DI Diesel engine, which relies on artificial neural networks and genetic algorithms, was developed.

# Table of contents

|   |            |
|---|------------|
| <b>Abstract</b>   | <b>iii</b> |
| <b>1 Introduction</b>                                       | <b>5</b>   |
| 1.1 Diesel combustion and its optimization . . . . .        | 6          |
| 1.2 Review of research activities . . . . .                 | 7          |
| 1.2.1 University of Wisconsin-Madison, USA . . . . .        | 7          |
| 1.2.2 Doshisha University, Japan . . . . .                  | 8          |
| 1.2.3 University of Salento, Italy . . . . .                | 8          |
| 1.3 Motivation and objectives of the present work . . . . . | 9          |
| <b>2 Subject of investigation</b>                           | <b>10</b>  |
| 2.1 Engine specifications . . . . .                         | 13         |
| 2.2 Investigated input parameters . . . . .                 | 13         |
| 2.3 Investigated operating point . . . . .                  | 13         |
| <b>3 The 3D CFD model</b>                                   | <b>16</b>  |
| 3.1 The CFD code KIVA-3D . . . . .                          | 16         |
| 3.1.1 Governing equations . . . . .                         | 17         |
| 3.1.2 Source terms due to chemical reactions . . . . .      | 19         |
| 3.1.3 Source terms due to the spray . . . . .               | 20         |
| 3.1.4 Physical models . . . . .                             | 20         |
| 3.2 Computational meshes . . . . .                          | 21         |
| 3.3 Initial conditions . . . . .                            | 23         |
| <b>4 The artificial neural network</b>                      | <b>25</b>  |
| 4.1 RBF neural networks . . . . .                           | 26         |
| 4.2 Learning strategy . . . . .                             | 27         |
| 4.2.1 Centers selection . . . . .                           | 27         |
| 4.2.2 Widths selection . . . . .                            | 29         |
| 4.2.3 Weight selection . . . . .                            | 30         |

|          |  |           |
|----------|--|-----------|
| <b>5</b> | <b>The genetic algorithm</b>                                       | <b>31</b> |
| 5.1      | The NSGA-II genetic algorithm . . . . .                            | 32        |
| 5.1.1    | Sorting algorithm . . . . .  | 32        |
| 5.1.2    | Density estimation . . . . .                                       | 33        |
| 5.1.3    | Crowded comparison operator . . . . .                              | 35        |
| 5.1.4    | The main loop . . . . .  | 35        |
| <b>6</b> | <b>RBF neural networks training</b>                                | <b>37</b> |
| 6.1      | Influence of the input variables on engine gross-IMEP . . . . .    | 38        |
| 6.2      | Influence of the input variables on engine NOx emission . . . . .  | 40        |
| 6.3      | Influence of the input variables on engine soot emission . . . . . | 42        |
| 6.4      | RBF neural networks validation . . . . .                           | 44        |
| <b>7</b> | <b>Multi-objective optimization of the piston bowls</b>            | <b>46</b> |
| 7.1      | Comparison between the Pareto frontiers . . . . .                  | 51        |
| <b>8</b> | <b>Combustion analysis of the optimal solutions</b>                | <b>54</b> |
| 8.1      | Emissions and performance . . . . .                                | 55        |
| 8.2      | Combustion development . . . . .                                   | 55        |
| 8.3      | NOx emission . . . . .   | 64        |
| 8.4      | Soot emission . . . . .  | 70        |
| <b>9</b> | <b>Conclusion</b>  | <b>79</b> |
|          | <b>Bibliography</b>  | <b>81</b> |

# List of figures

|      |  |    |
|------|--|----|
| 1.1  | Renner’s phenomenological model of Diesel combustion . . . . .   | 6  |
| 2.1  | Investigated engine . . . . .                                    | 10 |
| 2.2  | Piston bowl G012 . . . . .                                       | 11 |
| 2.3  | Piston bowl VHP011 . . . . .                                     | 12 |
| 2.4  | Piston bowl NE . . . . .   | 12 |
| 2.5  | Injection profile . . . . .                                      | 15 |
| 3.1  | G012 piston bowl mesh . . . . .                                  | 21 |
| 3.2  | NE piston bowl mesh . . . . .                                    | 22 |
| 3.3  | VHP011 piston bowl mesh . . . . .                                | 22 |
| 4.1  | RBF neural network lay-out . . . . .                             | 26 |
| 4.2  | An example of K-means clustering . . . . .                       | 28 |
| 4.3  | p-nearest neighbor . . . . .                                     | 29 |
| 5.1  | Crowding distance . . . . .                                      | 34 |
| 6.1  | G012: influence of the input variables on gross-IMEP . . . . .   | 38 |
| 6.2  | VHP011: influence of the input variables on gross-IMEP . . . . . | 39 |
| 6.3  | NE: influence of the input variables on gross-IMEP . . . . .     | 39 |
| 6.4  | G012: influence of the input variables on NOx . . . . .          | 40 |
| 6.5  | VHP011: influence of the input variables on NOx . . . . .        | 41 |
| 6.6  | NE: influence of the input variables on NOx . . . . .            | 41 |
| 6.7  | G012: influence of the input variables on soot . . . . .         | 42 |
| 6.8  | VHP011: influence of the input variables on soot . . . . .       | 43 |
| 6.9  | NE: influence of the input variables on soot . . . . .           | 43 |
| 6.10 | G012 neural network validation . . . . .                         | 44 |
| 6.11 | VHP011 neural network validation . . . . .                       | 45 |
| 6.12 | NE neural network validation . . . . .                           | 45 |
| 7.1  | soot - NOx . . . . .   | 48 |

|      |  |    |
|------|--|----|
| 7.2  | NOx - IMEP . . . . .   | 48 |
| 7.3  | soot - NOx . . . . .   | 49 |
| 7.4  | NOx - IMEP . . . . .   | 49 |
| 7.5  | soot - NOx . . . . .   | 50 |
| 7.6  | NOx - IMEP . . . . .   | 50 |
| 7.7  | Pareto frontiers: soot-NOx . . . . .   | 51 |
| 7.8  | Pareto frontiers: NOx-IMEP . . . . .   | 52 |
|      |  |    |
| 8.1  | In-cylinder pressure . . . . .   | 56 |
| 8.2  | Net rate of heat release . . . . .   | 56 |
| 8.3  | Isosurface of $\phi = 1$ coloured by temperature at -4.0 CA deg. ATDC .                      | 57 |
| 8.4  | Isosurface of $\phi = 1$ coloured by temperature at -1.5 CA deg. ATDC .                      | 58 |
| 8.5  | Isosurface of $\phi = 1$ coloured by temperature at 1.0 CA deg. ATDC .                       | 59 |
| 8.6  | Isosurface of $\phi = 1$ coloured by temperature at 6.0 CA deg. ATDC .                       | 60 |
| 8.7  | Isosurface of $\phi = 1$ coloured by temperature at 11.0 CA deg. ATDC .                      | 61 |
| 8.8  | Isosurface of $\phi = 1$ coloured by temperature at 21.0 CA deg. ATDC .                      | 62 |
| 8.9  | Isosurface of $\phi = 1$ coloured by temperature at 26.0 CA deg. ATDC .                      | 63 |
| 8.10 | NOx emission . . . . .   | 65 |
| 8.11 | Mean chamber temperature . . . . .   | 65 |
| 8.12 | Hot spots . . . . .  | 66 |
| 8.13 | Isosurface of $T = 2200K$ coloured by oxygen mass fraction at 11.0<br>CA deg. ATDC . . . . . | 67 |
| 8.14 | Isosurface of $T = 2200K$ coloured by oxygen mass fraction at 21.0<br>CA deg. ATDC . . . . . | 68 |
| 8.15 | Isosurface of $T = 2200K$ coloured by oxygen mass fraction at 31.0<br>CA deg. ATDC . . . . . | 69 |
| 8.16 | Soot emission . . . . .  | 71 |
| 8.17 | Percentage of fuel rich zones . . . . .  | 71 |
| 8.18 | In-cylinder oxygen mass fraction . . . . .   | 72 |
| 8.19 | Isosurface of $\phi = 3$ coloured by temperature at 21.0 CA deg. ATDC .                      | 73 |
| 8.20 | Isosurface of $\phi = 3$ coloured by temperature at 26.0 CA deg. ATDC .                      | 74 |
| 8.21 | Isosurface of $\phi = 3$ coloured by temperature at 31.0 CA deg. ATDC .                      | 75 |
| 8.22 | Isosurface of $\phi = 3$ coloured by temperature at 36.0 CA deg. ATDC .                      | 76 |
| 8.23 | Isosurface of $\phi = 3$ coloured by temperature at 41.0 CA deg. ATDC .                      | 77 |
| 8.24 | Isosurface of $\phi = 3$ coloured by temperature at 46.0 CA deg. ATDC .                      | 78 |

# List of tables

|     |   |    |
|-----|---|----|
| 2.1 | Engine specifications . . . . .   | 13 |
| 2.2 | Input parameters ranges . . . . .   | 13 |
| 2.3 | Injection strategy . . . . .  | 14 |
| 3.1 | EGR 5%, <i>Pboost</i> from 3.25 through 3.39: Species mass initialization . | 23 |
| 3.2 | EGR 10%, <i>Pboost</i> from 3.25 through 3.39: Species mass initialization  | 23 |
| 3.3 | EGR 15%, <i>Pboost</i> from 3.25 through 3.39: Species mass initialization  | 24 |
| 7.1 | Minimum NOx individuals . . . . .   | 47 |
| 7.2 | Trade-off individuals . . . . .   | 47 |
| 7.3 | Minimum soot individuals . . . . .  | 47 |
| 7.4 | G012 trade-off individual validation . . . . .                              | 53 |
| 7.5 | VHP011 trade-off individual validation . . . . .                            | 53 |
| 7.6 | NE trade-off individual validation . . . . .                                | 53 |
| 8.1 | Comparison between the real trade-off individuals . . . . .                 | 55 |

# Nomenclature

**ANN** Artificial neural network

**RBF** Radial basis function

**GA** Genetic algorithm

**CFD** Computational fluid dynamics

**ICE** Internal combustion engine

**DI** Direct injection

**IMEP** Indicated mean effective pressure

**CA** Crank angle

**TDC** Top dead crank

**ATDC** After top dead crank

**CR** Compression ratio

**SR** Swirl ratio

**MFB** Burnt fuel mass

**RNG** Renormalisation group

**SOI** Start of injection

**HSOI** Hydraulic start of injection

$\lambda$  Air/fuel equivalence ratio

$\Phi$  Fuel/air equivalence ratio

$\kappa$  Turbulent kinetic energy

$\epsilon$  Eddy dissipation rate

# Chapter 1

## Introduction

DI Diesel engine are widely used both for industrial and automotive applications due to their durability and fuel economy.

However, increasing environmental concerns force that type of engine to comply with increasingly demanding emission limits. From Euro2 emission standard through Euro5 emission standard, both NO<sub>x</sub> and soot emission have been drastically decreased and the upcoming Euro6 emission standard is even more pressing, so that, although Diesel engine are more and more equipped with one or more after-treatment devices, a significant combustion improvement is needed to meet the latest emission standards.

In such a scenario, it has become mandatory to develop a robust design methodology of the DI Diesel combustion system focused on reduction of soot and NO<sub>x</sub> simultaneously while maintaining a reasonable fuel economy.

With the current status of CPU speed and model development, combustion modeling of the DI Diesel engine by means of a CFD code is becoming a necessary tool in order to optimize the Diesel combustion system, both in terms of emissions and performance, allowing to investigate a large number of possible configurations in a very short time, thus, overcoming limitations and drawbacks of experimentally executed parametric searches which need huge expenses and huge time.

However, since there are trade-off relationships between engine performance, NO<sub>x</sub> and soot emissions numerically executed parametric searches can not find a unique solution which optimizes all the objectives of a good design at the same time but rather there will exist different solutions, all representing an efficient allocation of resources, known as Pareto optimal solutions.

In other words, the design process of the DI Diesel engine should be handled as multi-objective optimization problem.

## 1.1 Diesel combustion and its optimization

In 1998 Renner proposed a phenomenological model, which is widely accepted, for Diesel injection and combustion (fig. 1.1).

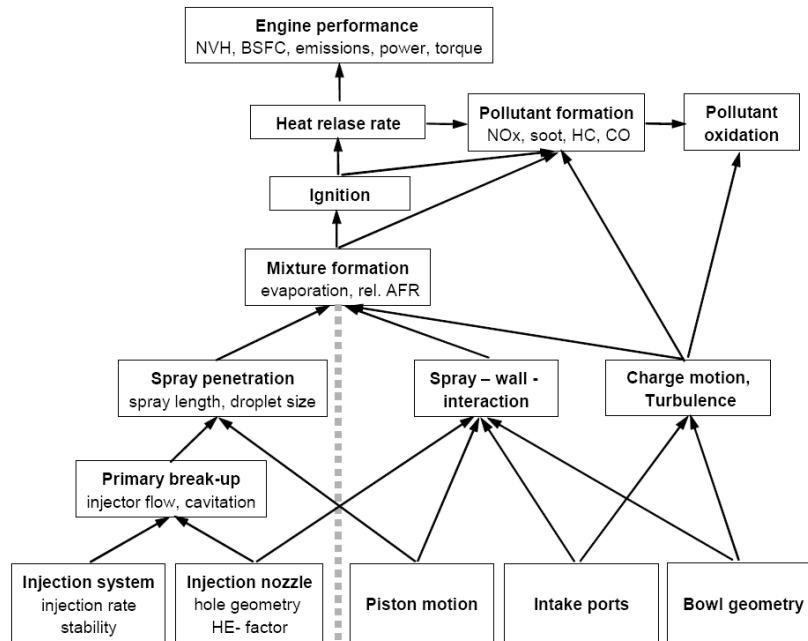


Fig. 2. Phenomenological model for Diesel injection and combustion according to Renner (1998)

Figure 1.1. Renner's phenomenological model of Diesel combustion

According to Renner's phenomenological model DI Diesel combustion is the result of very complex interactions between spray penetration, spray-wall interaction, different charge motions and turbulence which are appointed to promote a proper mixture formation and, then, a clean and efficient combustion. Mixture formation and charge motions also affect pollutant and oxydation.

Spray penetration, spray-wall interaction, charge motions and turbulence are in turn the result of very complex interactions between the input variables which are categorized in:

- variables related to the engine architecture (piston motion, intake ports, bowl geometry)
- variables related to the injection system (injection nozzle, injection system)

Injection nozzle and injection system affect the primary break-up. Piston motion and primary break-up affect the spray penetration. Injection nozzle, piston motion,

intake ports, bowl geometry influence spray-wall interaction. Intake ports and bowl geometry influence the in-cylinder charge motions.

Renner’s model can also be useful to clarify which are the main issues in developing an efficient low-emission/high performance combustion inside the DI Diesel engine:

- a large number of input variables has to be considered, some of those are related to geometrical parameters of the engine and, thus, can be experimentally investigated with difficulty since they need to build different intake ports, pistons and so on
- it is not trivial to evaluate how each input variable affects air/fuel mixing, ignition, heat release rate and, thus, emissions and performance of the engine
- it is even more difficult to evaluate how the input variables interact each others and how that interaction affects the combustion development
- typically there are trade-off relationships between NO<sub>x</sub>, soot and engine performance and, thus, it is not possible to find a unique set of input variables which optimizes all the engine outputs simultaneously

To overcome these issues, the design of an efficient DI Diesel combustion system can no longer rely exclusively upon experience, but rather should be mathematically represented as a multi-objective optimization problem, the objectives being the minimization of NO<sub>x</sub> and soot emissions and the maximization of engine performance, for which multi-objective genetic algorithms and CFD calculations have been successfully applied in recent years.

## 1.2 Review of research activities

### 1.2.1 University of Wisconsin-Madison, USA

At University of Wisconsin-Madison several studies on Diesel optimization have been conducted.

In [25] a computational methodology for engine design using multi-dimensional spray and combustion modeling was established. The KIVA-GA code incorporates an improved KIVA-3V CFD model within the framework of a  $\mu$ GA optimization technique. The design factors were: boost pressure, EGR level, start of injection, injection duration, mass in the first pulse, dwell between pulses. The  $\mu$ GA efficiently determined a set of input parameters resulting in significantly lower soot and No<sub>x</sub> emissions compared to the baseline case.

In [27] a non-dominated sorting algorithm (NSGA-II) was coupled the KIVA CFD code, as well as with an automated grid generation technique to conduct the multi-objective optimization with goals of low emissions and improved fuel economy. The study identifies the aspects of the combustion and pollutant formation that are affected by mixing, and offers guidance for better matching of the piston geometry with the spray plume for enhanced mixing.

### 1.2.2 Doshisha University, Japan

Doshisha University has focused on the multi-objective optimization of the Diesel engine using genetic algorithms and a phenomenological model [19]. SFC, NO<sub>x</sub> and soot are minimized by changing the rate of fuel injection. The HIDECS model [18], which is based on the phenomenological model, was used. An extended GA that is called the Neighborhood Cultivation Genetic Algorithm (NCGA) was used. The NCGA has the neighborhood crossover mechanism besides the mechanism of NSGA-II [24]. By this work, the NCGA can successfully derive the Pareto optimum solutions, although, many iterations are needed. Therefore, the phenomenological model is suitable for optimization by the GAs since it does not need a high calculation cost.

### 1.2.3 University of Salento, Italy

Research activities at University of Salento cover the multi-objective GA optimization of the DI Diesel engine combustion chamber and of the common rail injector. In [16] a GA optimization of some geometric features of the combustion chamber was performed. For all the investigated chambers, bowl volume and squish-to-volume ratio were kept constant in order to ensure the same compression ratio. The evaluation phase of the genetic algorithm was performed by simulating the behaviour of each chamber with a modified version of the KIVA-3V code. The optimization method was based on the use of genetic programming, a search procedure developed at the University of Michigan. The study also offered a comparison between the standard-GA procedure and the so called  $\mu$ GA procedure proposed in [25]

In [15] the same optimization method was applied to the optimization of a common rail injector. Three different methods, based on variable weights combination, distance from the global optimum and individuals' rank respectively, were implemented for the calculation of the overall fitness. The evaluation phase of the genetic algorithm was performed by running the fluid dynamic code PROFLUID, which is able to simulate the injection event according to the common rail operating conditions and injector geometrical data. The optimization aimed at identifying the values of seven geometrical parameters which gave a needle lift law as close as possible to the current impulse governing the injection event.

### 1.3 Motivation and objectives of the present work

For the DI Diesel engine to comply with the upcoming emission limits a robust design methodology is needed since, in order to achieve a significant combustion improvement, the designer must fully master a deep understanding of how each input variable affects engine emissions and performance. Although their usefulness, experimental investigations face serious limitations. In fact, only a small number of different combustion chambers and/or intake ports can be simultaneously compared with experimental studies while a wide parametric study can be easily performed with the use of CFD code, and, thus, the development of a numerical methodology for engine design would significantly aid in the pursuit of cleaner and more efficient engines.

To that purpose, since there are trade-off relationships between NO<sub>x</sub>, soot and gross-IMEP, several authors (see 1.2.1, 1.2.2, 1.2.3) have proposed different methodologies relying upon multi-objective genetic algorithms for the optimization of the DI Diesel engine and have shown the effectiveness of that mathematical approach. However, in the studies proposed by the University of Wisconsin-Madison and the University of Salento the evaluation phase of the multi-objective genetic algorithm is entirely demanded to CFD calculations making the optimization procedure time-expensive since a large number of calculations is needed for the genetic algorithms to converge. On the contrary, in the studies proposed by the Doshisha University the evaluation phase of the genetic algorithm relies upon the HIDECS Diesel injection and combustion phenomenological model since it does not need a high computational cost. Nonetheless, a phenomenological model presents serious limitations while investigating piston bowl change-in-shape.

The aim of the current study was to develop and validate a hybrid approach for the multi-objective optimization of the DI Diesel engine which was, at the same time, fast and accurate. At the base of the methodology, three-dimensional CFD calculations were used to generate a valid training set for the learning process of an artificial neural network. Artificial neural network were chosen amongst other statistical modeling tools due to their ability to model complex relationships between inputs and outputs like those which tie up design parameters and objectives inside the DI Diesel engine (see 1.1). Then, once properly trained, the artificial neural networks were used during the evaluation phase of the genetic algorithm to foresee NO<sub>x</sub>, soot and gross-IMEP as a function of the input parameters. The NSGA-II genetic algorithm [24] was used due to its ability to find Pareto optimal solutions in one single run with a low computational cost. At the final stage, only the best individuals were verified through actual three-dimensional CFD simulations and a deep investigation of their combustion development was carried out.

## Chapter 2

### Subject of investigation

In the present study, the numerical methodology for the multi-objective optimization was used to aid the design process of a DI Diesel engine targeted for automotive applications. The investigated engine was a 4-cylinders/4-valve for cylinder engine with a total displacement of 2.4 liters (fig. 2.1).



Figure 2.1. Investigated engine

During the development process of the engine, three different piston bowls (figg. 2.2, 2.3, 2.4) were tested. All the piston bowls had the same volume resulting in a compression ratio of 15.5. Nonetheless, they were quite different in shape in order to develop different combustion concepts which need different operating conditions to be optimized.

Thus, it was to mandatory, in order to correctly evaluate the piston bowls performances, to investigate the three piston bowls under a range of operating conditions as wide as possible.

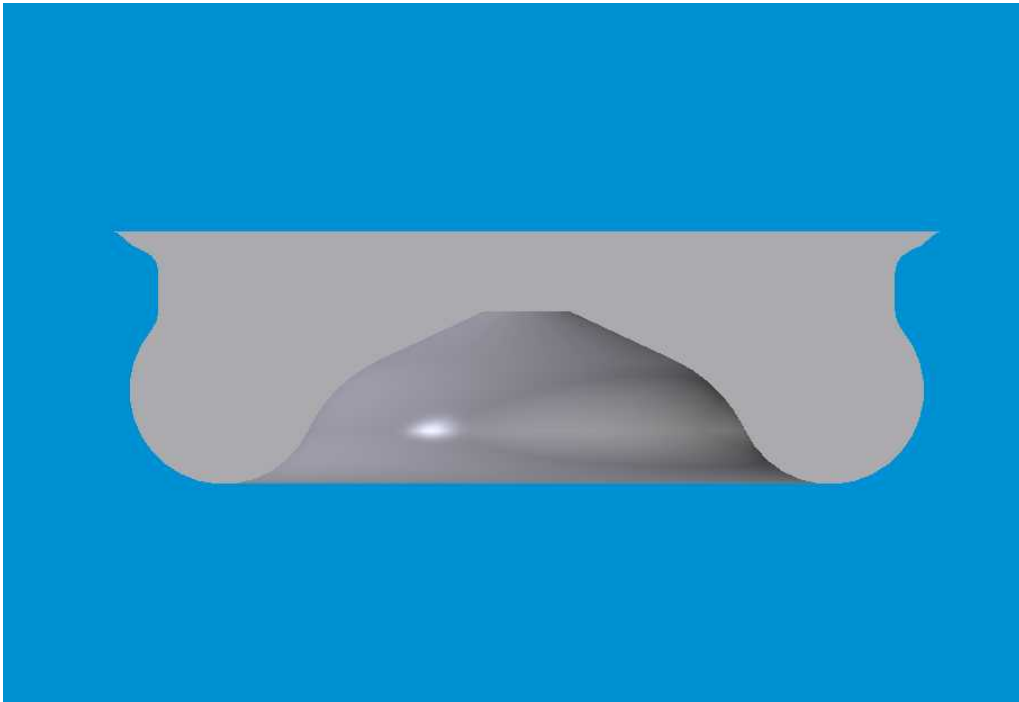


Figure 2.2. Piston bowl G012

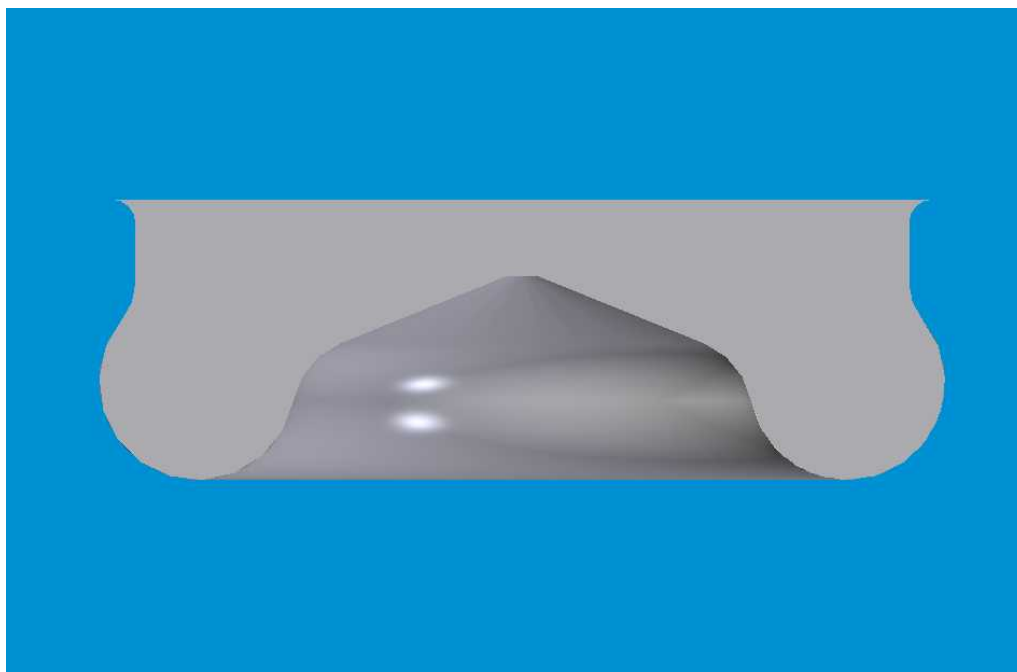


Figure 2.3. Piston bowl VHP011

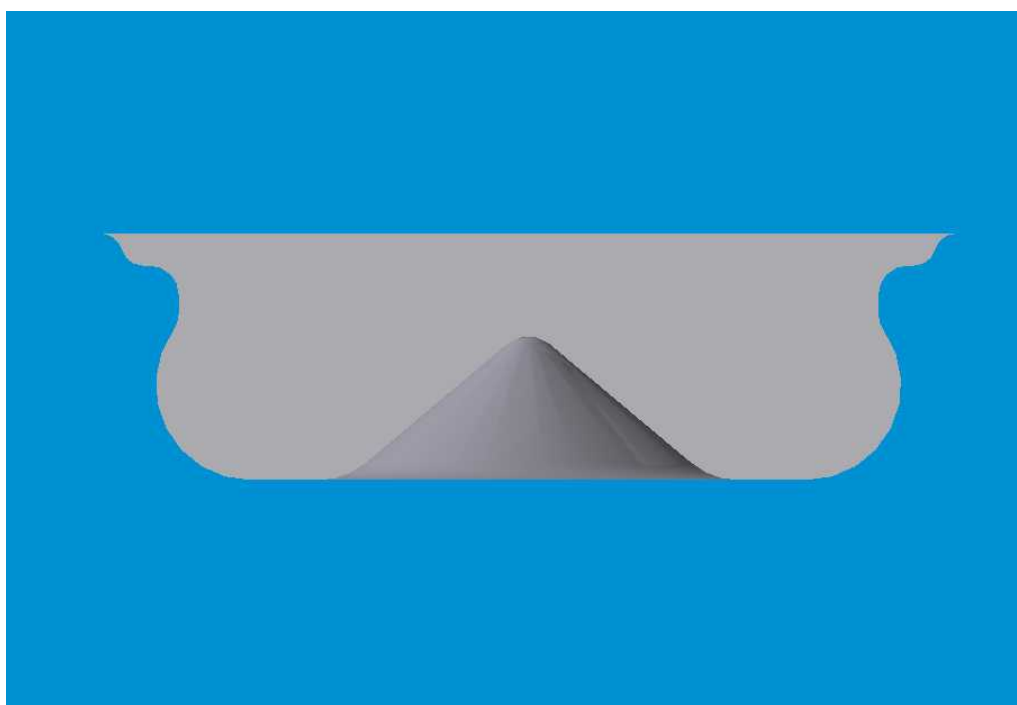


Figure 2.4. Piston bowl NE

## 2.1 Engine specifications

In table 2.1 are reported the main engine specifications:

|                                   |      |
|-----------------------------------|------|
| <b>Bore</b> [mm]                  | 92   |
| <b>Stroke</b> [mm]                | 92   |
| <b>Connecting rod</b> [mm]        | 159  |
| <b>Squish height</b> [mm]         | 0.7  |
| <b>IVC</b> [deg. ATDC]            | -130 |
| <b>EVO</b> [deg. ATDC]            | 114  |
| <b>Maximum power regime</b> [rpm] | 4000 |

Table 2.1. Engine specifications

## 2.2 Investigated input parameters

Input parameters were chosen, as reported in table 2.2, in order to focus the optimization on the engine on the variables which were more strongly related to design choice.  $P_{boost}$  represented the in-cylinder pressure at intake valve closure. SR was the swirl ratio at intake valve closure. EGR was the in-cylinder exhaust gas mass fraction at intake valve closure. SOI was referred to the hydraulic start of injection. The range of each input variable was chosen to ensure a wide exploration of the design space.

|                                      |       |      |      |
|--------------------------------------|-------|------|------|
| <b><math>P_{boost}</math></b> [ bar] | 3.25  | 3.32 | 3.39 |
| <b>SR</b>                            | 1.0   | 1.5  | 2.0  |
| <b>EGR</b> [%]                       | 5.0   | 10.0 | 15.0 |
| <b>SOI</b> [ CA deg. ATDC]           | -12.0 | -9.0 | 6.0  |

Table 2.2. Input parameters ranges

## 2.3 Investigated operating point

In the current study, input variables were optimized at the maximum power operating condition of the investigated engine since such a condition is usually the more challenging to achieve a good trade-off between engine emissions and performance. In fact, when working under that operating condition the high rotational velocity of the engine and the high fuel delivery per stroke, needed to meet the desired power target, severely limit the use of multiple injection per cycle which can be useful at

lower working regime. Moreover, due to the high rotational velocity of the engine and the high injection pressure the squish motion, the reverse squish motion, the swirl motion and motions aerodynamically generated by the air/spray interaction become the driving force in the combustion development [3].

In table 2.3 is reported the reference injection strategy used in the current work. Particularly, the injector was a 7 holes injector with a delivery rate of  $400\text{cm}^3/30\text{s}$ . Starting from the reported values the injection profile shown in figure 2.5 was generated using a phenomenological model for Common rail injections developed at the University of Bologna.

|  |           |
|--|-----------|
| <b>HSOI</b> [deg. ATDC]                        | -9.0      |
| <b>Injection duration</b> [deg. ATDC]          | 40.0      |
| <b>Rail pressure</b> [bar]                     | 2000      |
| <b>Injected mass</b> [mg/stroke]               | 76.5      |
| <b>Fuel temperature</b> [K]                    | 360       |
| <b>Spray angle</b> [deg.]                      | 74        |
| <b>Actual injection area</b> [ $\text{cm}^2$ ] | 0.138E-03 |
| <b>Sauter mean ratio</b> [cm]                  | 0.663E-02 |
| <b>Injector holes</b>                          | 7         |

Table 2.3. Injection strategy

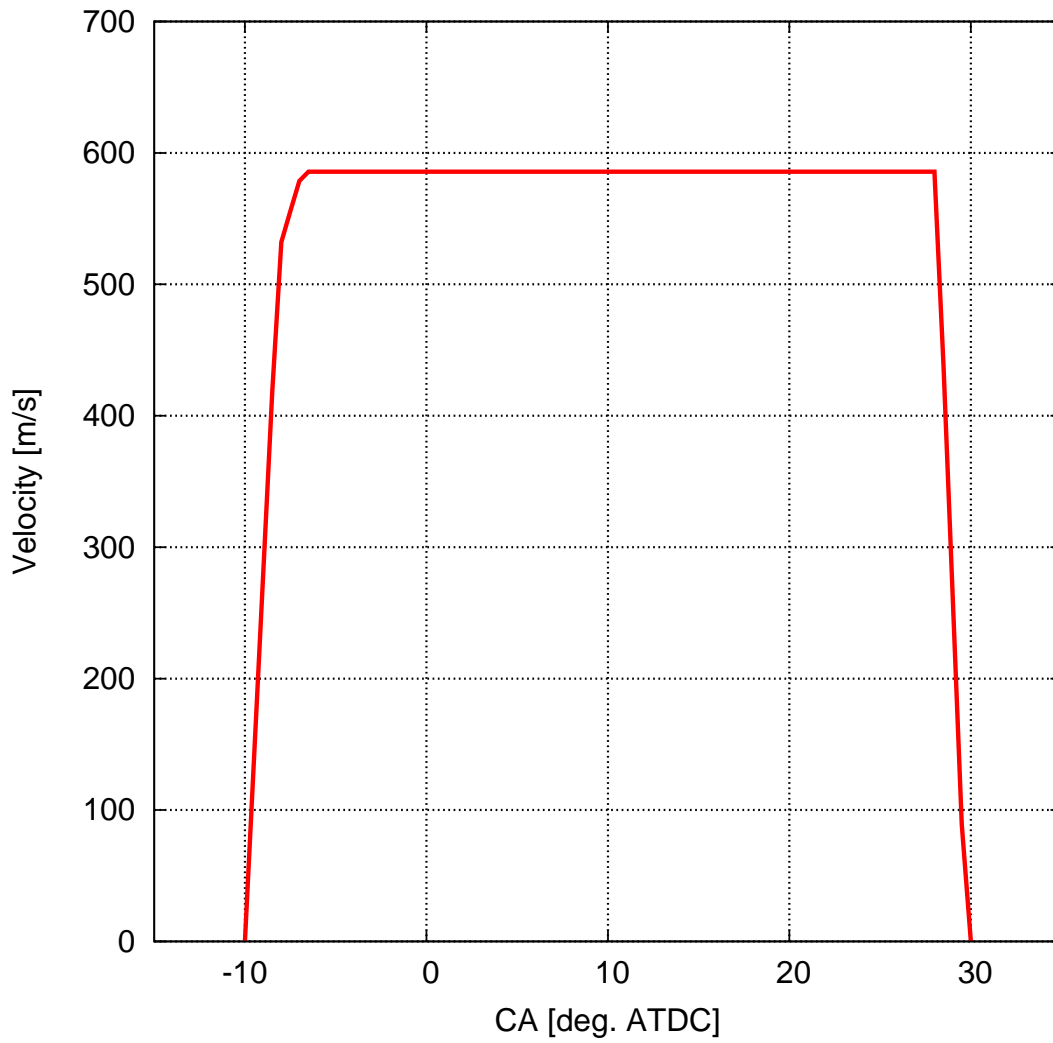


Figure 2.5. Injection profile

# Chapter 3

## The 3D CFD model

Fluid dynamics of internal combustion engines have to be considered as unsteady, compressible, turbulent and reactive species flows. In order to describe temporal and spatial evolution of density, temperature, velocity and mass fraction of the reacting species three-dimensional combustion calculations have to be performed.

In the present work, the CFD code KIVA-3D, a modified version of the KIVA-3 code [2], developed at the University of Bologna since 1996, was used to describe the physical problem.

### 3.1 The CFD code KIVA-3D

Over the past several years, computational fluid dynamics (CFD) has been increasingly accepted as an adjunct to experimentation in the design and understanding of practical combustion system.

The original KIVA program was publicly released in 1985, and was replaced by the improved KIVA-II in 1989. These earlier version of KIVA lend themselves well to confined in-cylinder flows and a variety of open combustion systems, but can become quite inefficient to use in complex geometries that contain such features as inlet ports and valves, diesel prechambers and entire transfer ports.

KIVA-3 was specifically developed to overcome this inefficiency by employing a block-structured mesh that eliminates the necessity of maintaining large regions of deactivated cells and results in a reduction of both storage and computer time for complex geometries.

Since 1996 the CFD code KIVA-3 has been modified at the University of Bologna, following the work of several researchers. The turbulence RNG k-eps linear model was updated following the work of Han and Reitz [17], and Bianchi et al. [9]. The fuel liquid dispersed phase was treated according to a Lagrangian approach using the hybrid spray breakup model proposed and validated by Bianchi et al.

[6]. The latter accounts for both the atomization of the liquid jet and the droplet secondary breakup. The spray-wall interaction was modelled according to Cazzoli et al. [12]. The fuel auto-ignition was simulated using the Shell model in the implementation proposed by Kong et al. [20]. The high-temperature combustion part follows the characteristic-time combustion model developed by Abraham et al. [1], with the correction proposed by Bianchi et al. [8] to account for non-equilibrium turbulence effects of the energy cascade and thus on the turbulence time scales. Finally the extended Zeldovich mechanism is used to model NO<sub>x</sub> formation while the Hiroyasu's formation model [18] and the Strickland-Constable's model for the oxidation [22] have been used to predict in-cylinder soot.

### 3.1.1 Governing equations

The numerical simulation of combustion phenomena is an extremely complex problem. In this kind of problem there are essentially three separate (but coupled) systems evolving during the combustion process: the fluid, which is described by the conservation equations of continuum mechanics; the interaction of the various chemical species making up the fluid, which react both at equilibrium and kinetically; the interaction between the injected fluid droplets and the reacting fluid.

The fully coupled system of governing equations consists of:

- the equation of compressible fluid dynamics
- kinetic and equilibrium chemical reactions
- spray droplet interactions

The following are the governing equations in KIVA-III for chemically reacting fluid flow in three-dimension.

Conservation of mass:

$$\frac{\partial \rho}{\partial t} + \nabla \cdot (\rho \mathbf{u}) = \dot{\rho}^s \quad (3.1)$$

Conservation of momentum:

$$\frac{\partial(\rho \mathbf{u})}{\partial t} + \nabla \cdot (\rho \mathbf{u} \mathbf{u}) = \rho g + F^s - \frac{1}{\alpha^2} \nabla p + \nabla \cdot \bar{\sigma} - A_0 \nabla \left( \frac{2}{3} \rho \kappa \right) \quad (3.2)$$

Conservation of energy:

$$\frac{\partial(\rho I)}{\partial t} + \nabla \cdot (\rho \mathbf{u} I) = -\nabla \cdot J + \dot{Q}^c + \dot{Q}^s - p \nabla \cdot \mathbf{u} + (1 - A_0) \bar{\sigma} : \nabla \mathbf{u} + A_0 \rho \epsilon \quad (3.3)$$

Turbulent kinetic energy:

$$\frac{\partial(\rho\kappa)}{\partial t} + \nabla \cdot (\rho\mathbf{u}\kappa) = -\frac{2}{3}\rho\kappa\nabla \cdot \mathbf{u} + \bar{\sigma} : \nabla\mathbf{u} + \nabla \cdot \left[ \left( \frac{\mu}{Pr_\kappa} \right) \nabla\kappa \right] - \rho\epsilon + \dot{W}^s \quad (3.4)$$

Turbulent kinetic energy dissipation:

$$\frac{\partial(\rho\epsilon)}{\partial t} + \nabla \cdot (\rho\mathbf{u}\epsilon) = -\left( \frac{2}{3}c_{\epsilon_1} - c_{\epsilon_2} \right) \rho\epsilon\nabla \cdot \mathbf{u} + \nabla \cdot \left[ \left( \frac{\mu}{Pr_\epsilon} \right) \nabla\epsilon \right] + \frac{\epsilon}{\kappa} \left( c_{\epsilon_1}\bar{\sigma} : \nabla\mathbf{u} - c_{\epsilon_2}\rho\epsilon + c_s\dot{W}^s \right) \quad (3.5)$$

Heat flux:

$$J = -K\nabla T - \rho D \sum_m h_m \nabla \left( \frac{\rho_m}{\rho} \right) \quad (3.6)$$

Equations of state:

$$p = R_0 T \sum_m \left( \frac{\rho_m}{\rho} \right) \quad (3.7)$$

$$I(T) = \sum_m \left( \frac{\rho_m}{\rho} \right) I_m(T) \quad (3.8)$$

$$c_p(T) = \sum_m \left( \frac{\rho_m}{\rho} \right) c_{pm}(T) \quad (3.9)$$

$$h_m(T) = I_m(T) + \frac{R_0 T}{W_m} \quad (3.10)$$

Mass consistency:

$$\sum_{m=1}^{N_c} \frac{\rho_m}{\rho} = 1 \quad (3.11)$$

Conservation of mass for chemical species m (one equation for each of the  $N_c$  species):

$$\frac{\partial(\rho_m)}{\partial t} + \nabla \cdot (\rho_m \mathbf{u}) = \nabla \cdot \left[ \rho D \nabla \left( \frac{\rho_m}{\rho} \right) \right] + \dot{\rho}_m^c + \dot{\rho}_m^s \delta_{m1} \quad (3.12)$$

The eleven equation from 3.1 through 3.11 and  $N_c$  occurrences of equation 3.11 for  $N_c$  chemical species yields  $N_c+11$  equations for the  $N_c+10$  unknowns  $\rho, \mathbf{u}, I, \kappa, \epsilon, J, p, T, \rho_1, \dots, \rho_{N_c}$ . Since one of the mass equations is redundant due to the consistency equation, it is discarded, leaving  $N_c + 10$  equations and unknowns.

### 3.1.2 Source terms due to chemical reactions

The following source terms appear due to the chemical reactions:

- $\dot{\rho}_m^c$ , mass density source term species  $m$  due to chemical reactions
- $\dot{Q}^c$ , chemical heat release due to kinetic reaction

The mass density source terms  $\dot{\rho}_m^c$  depend on the reaction rates  $\dot{\omega}_r$  as follows:

$$\dot{\rho}_m^c = W_m \sum_r (b_{mr} - a_{mr}) \dot{\omega}_r \quad (3.13)$$

where reaction  $r$  is in the form:



where  $x_m$  represents one mole of chemical species  $m$  and  $a_{mr}$ ,  $b_{mr}$  represent integer stoichiometric coefficients for species  $m$  in reaction  $r$ . For mass to be conserved, we must have for each reaction  $r$  that:

$$\sum_m (a_{mr} - b_{mr}) W_m = 0 \quad (3.15)$$

where  $W_m$  is the molecular weight of species  $m$ .

For equilibrium reactions, the reaction rates  $\dot{\omega}_r$  are determined implicitly by the constraint that the mass densities  $\rho_m$  of all the chemical species satisfy the following relationship at all the times:

$$\prod_m \left( \frac{\rho_m}{W_m} \right)^{b_{mr} - a_{mr}} = K_c^r(T) \quad (3.16)$$

where the *concentration equilibrium constant*  $K_c^r$  for reaction  $r$  takes the form:

$$K_c^r = e^{[A_r \ln T_a + (\frac{B_r}{T_a}) + C_r + D_r T_a + E_r T_a^2]} \quad (3.17)$$

For kinetic reactions, the reaction rate  $\dot{\omega}_r$  for reaction  $r$  is defined as:

$$\dot{\omega}_r = \kappa_{fr} \prod_m \left( \frac{\rho_m}{W_m} \right)^{a'_{mr}} - \kappa_{br} \prod_m \left( \frac{\rho_m}{W_m} \right)^{b'_{mr}} \quad (3.18)$$

where the coefficients involved are *Arrhenius* in form:

$$\kappa_{fr} = A_{fr} T^{\xi_{fr}} e^{-\frac{E_{fr}}{T}} \quad (3.19)$$

$$\kappa_{br} = A_{br} T^{\xi_{br}} e^{-\frac{E_{br}}{T}} \quad (3.20)$$

The constants  $A_{fr}, A_{br}, T^{\xi_{fr}}$  and  $T^{\xi_{br}}$  are defined for each reaction and assumed given. The values  $E_{fr}$  and  $E_{br}$  are activation temperatures for reaction  $r$ . The stoichiometric coefficients  $a'_{mr}$  and  $b'_{mr}$  are allowed to vary from  $a_{mr}$  and  $b_{mr}$  to allow the use of empirically determined reaction coefficients.

In the case of kinetic reactions, chemical heat is released. The relationship between the heat source term  $\dot{Q}^c$  and the reaction rate  $\dot{\omega}_r$  is:

$$\dot{Q}^c = \sum_r Q_r \dot{\omega}_r \quad (3.21)$$

where  $Q_r$  is the negative of the heat of reaction at absolute zero for reaction  $r$ :

$$Q_r = \sum_m (a_{mr} - b_{mr}) (\Delta h_f^\circ)_m \quad (3.22)$$

where the given parameter  $(\Delta h_f^\circ)_m$  is the *heat of formation* of species  $m$  at  $T = 0$ .

### 3.1.3 Source terms due to the spray

The following source terms appear due to the spray:

- $\dot{\rho}_m^s$ , mass density source term due to sprayed species  $m$
- $F^s$ , rate of momentum gain per unit volume due to the spray
- $\dot{Q}^s$ , heat source due to spray interactions
- $\dot{W}^s$ , negative rate at which turbulent eddies do work dispersing spray droplets

### 3.1.4 Physical models

**Atomization and Break-Up:** Hybrid model (Bianchi e Pelloni)

**Wall-spray interaction:** Evaporating wall-film (Forte e Cazzoli)

**Turbulence:** RNG  $k - \epsilon$  Linear with wall function

**Ignition:** Shell model for diesel motors (Kong)

**Combustion:** Abraham modified (Bianchi et al.)

**Soot:** Hiroyasu + Nagle and Strickland-Constable

**Nox:** Zeldovich

## 3.2 Computational meshes

Due to the axi-symmetry of both geometry and flow each computational domain was composed of a  $51.43^\circ$  sector of the whole combustion chamber allowing to significantly decrease the computational costs of the calculations.

For each investigated piston bowl a block-structured mesh of about 30000 hexahedral cells was generated.

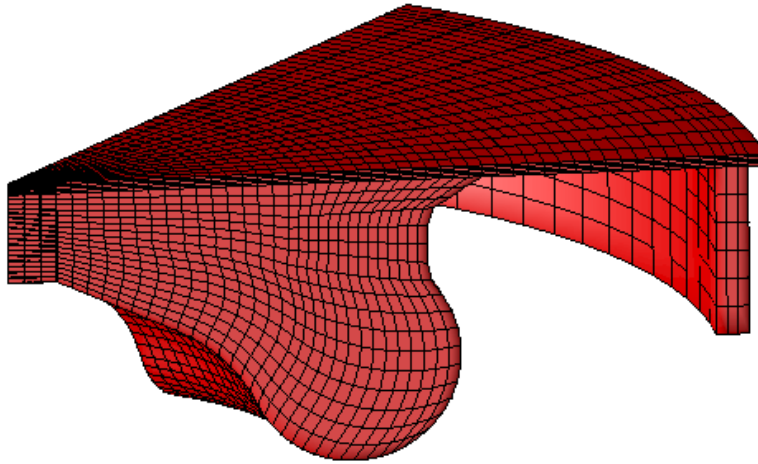


Figure 3.1. G012 piston bowl mesh

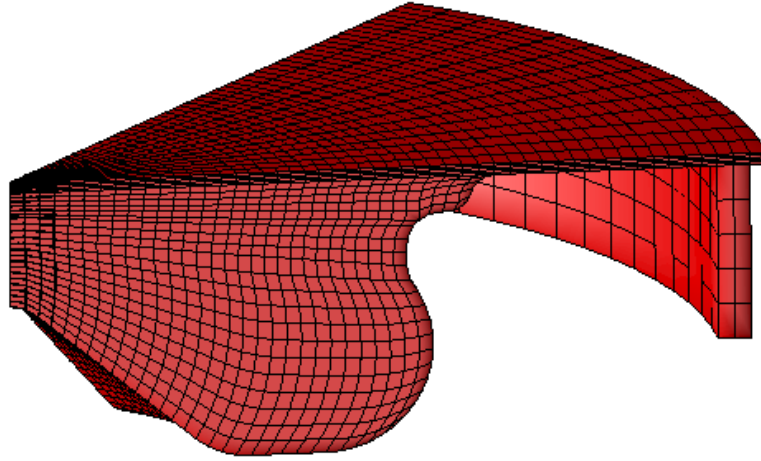


Figure 3.2. NE piston bowl mesh

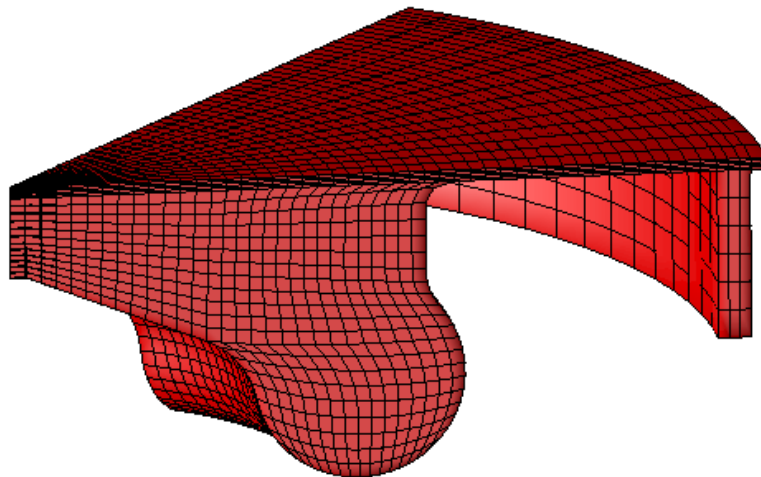


Figure 3.3. VHP011 piston bowl mesh

### 3.3 Initial conditions

The KIVA-3D performs in-cylinder combustion simulations between intake valve closure and exhaust valve opening. In the current work, species mass initialization for different values of in-cylinder pressure at intake valve closure ( $P_{boost}$ ) and EGR rate was generated as follows:

1. total trapped mass was calculated according the the requested in-cylinder pressure at intake valve closure for the given initial temperature (427 K)
2. air mass and EGR mass were calculated according to the requested EGR percentage
3. overall  $\lambda$  was calculated
4. exhaust gas composition was calculated knowing the EGR mass and the overall  $\lambda$

In tables 3.1, 3.2, 3.3 are shown the initial species at intake valve closure resulting from the chosen design of experiment:

| Species | Mass [g] | Species | Mass [g] | Species | Mass [g] |
|---------|----------|---------|----------|---------|----------|
| $O_2$   | 0.33354  | $O_2$   | 0.34107  | $O_2$   | 0.34695  |
| $N_2$   | 1.15412  | $N_2$   | 1.17921  | $N_2$   | 1.19880  |
| $CO_2$  | 0.01194  | $CO_2$  | 0.01195  | $CO_2$  | 0.01196  |
| $H_2O$  | 0.00524  | $H_2O$  | 0.00524  | $H_2O$  | 0.00525  |

Table 3.1. EGR 5%,  $P_{boost}$  from 3.25 through 3.39: Species mass initialization

| Species | Mass [g] | Species | Mass [g] | Species | Mass [g] |
|---------|----------|---------|----------|---------|----------|
| $O_2$   | 0.31796  | $O_2$   | 0.32551  | $O_2$   | 0.33136  |
| $N_2$   | 1.15067  | $N_2$   | 1.17586  | $N_2$   | 1.19542  |
| $CO_2$  | 0.02513  | $CO_2$  | 0.02516  | $CO_2$  | 0.02518  |
| $H_2O$  | 0.01102  | $H_2O$  | 0.01103  | $H_2O$  | 0.01104  |

Table 3.2. EGR 10%,  $P_{boost}$  from 3.25 through 3.39: Species mass initialization

| Species | Mass [g] | Species | Mass [g] | Species | Mass [g] |
|---------|----------|---------|----------|---------|----------|
| $O_2$   | 0.30066  | $O_2$   | 0.30816  | $O_2$   | 0.31401  |
| $N_2$   | 1.14693  | $N_2$   | 1.17206  | $N_2$   | 1.19159  |
| $CO_2$  | 0.03978  | $CO_2$  | 0.03983  | $CO_2$  | 0.03987  |
| $H_2O$  | 0.01745  | $H_2O$  | 0.01747  | $H_2O$  | 0.01748  |

Table 3.3. EGR 15%, *Pboost* from 3.25 through 3.39: Species mass initialization

## Chapter 4

# The artificial neural network

Artificial neural networks are non-linear statistical data modeling tools and can be used to model complex relationships between inputs and outputs or to find patterns in a dataset.

Since the end of the 1980's, neural networks have been successfully employed for analyzing data. Over the years, several models of neural networks have been proposed, among which, the multilayer perceptron and the radial basis function neural network are some of the most widely used. However, though its popularity, multi layer perceptron exhibits serious drawbacks and limitations such as the slow convergence of the learning algorithm, the potential convergence to a local minimum and the common chaotic behavior of nonlinear systems.

On the contrary, RBF neural networks can overcome some of these problems by relying on a rapid training phase, avoiding a chaotic behavior, and presenting systematic low responses to input patterns that have fallen into regions of the input space where there are no training samples and, thus, have attracted considerable attention and they have been widely applied in many science and engineering fields. Due to their characteristic RBF neural networks were used in current work as a fundamental tool for the meta-modeling of the engine combustion development as a function of the input variables.

Starting from the theoretical background of the radial basis functions neural networks, briefly described in section 4.1, and the learning strategy described in section 4.2 a specific software, written in Matlab/Octave language, was developed in order to train a RBF neural network from a set of CFD combustion calculations.

## 4.1 RBF neural networks

A radial basis function (RBF) network is a special type of feedforward neural network that uses a radial basis function as its activation function and is composed of three layer:

- the input layer
- the hidden layer
- the output layer

as shown in fig.4.1.

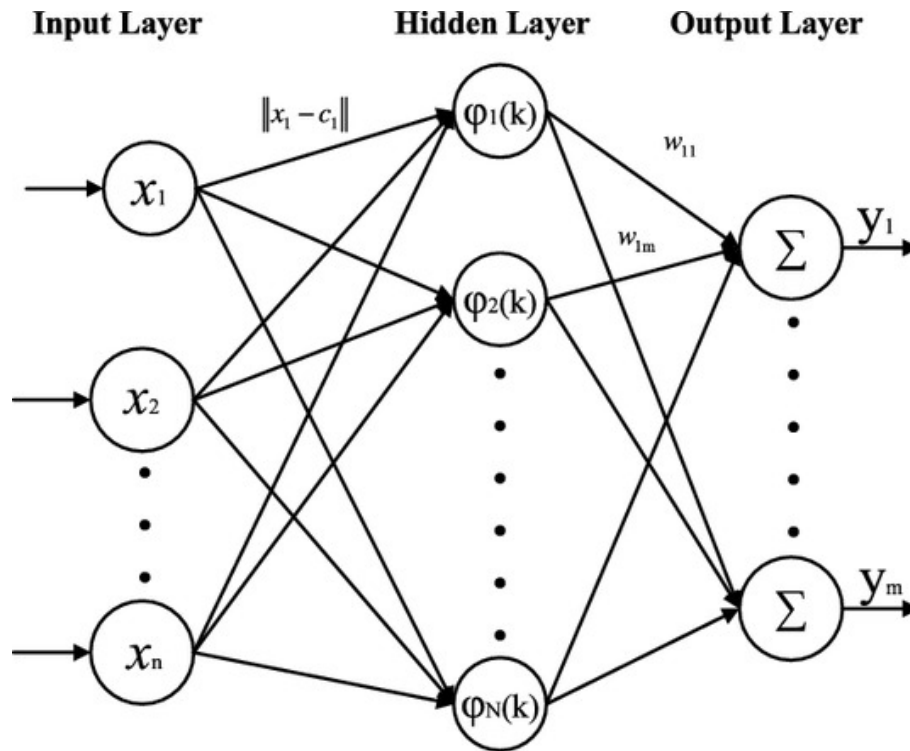


Figure 4.1. RBF neural network lay-out

The input layer relies on as many neurons as input features. Input neurons just propagate input features to the next layer.

The hidden layer is composed of a number of neurons  $m_1$  which must be lower or equal to  $N$ , where  $N$  is the number of training set data. Each neuron in the hidden layer is associated with a kernel function, in our case a Gaussian radial basis function, defined as:

$$G(x, x_i) = \exp\left(-\frac{1}{2\sigma_i^2} \|x - x_i\|^2\right) \quad (4.1)$$

where  $x_i$  is the center of the kernel function and  $\sigma_i$  its width.

The family of the hidden layer functions  $\Phi_i(x) | i = 1, 2, \dots, m_1$  can be represented as:

$$\Phi_i(x) = G(\|x - t_i\|) \quad (4.2)$$

where  $t_i | i = 1, 2, \dots, m_1$  are the center of the radial basis functions defined in 4.1.

When the number of training data can be easily worked those centers can be considered coincident with the training set input data. In other words,  $t_i = x_i$  for  $i = 1, 2, \dots, N$ .

The output layer is composed of as many neurons as the output of the observed system. Each output neuron is the weighted sum of the hidden layer functions and is given by:

$$F(x) = \sum_{i=1}^{m_1} w_{ij} G(x, t_i) \quad (4.3)$$

where  $w_{ij} | i = 1, 2, \dots, m_1$  are the weights of of each hidden neuron.

## 4.2 Learning strategy

According to scientific literature [10], in the current work, the learning strategy of the RBF neural network was performed in two steps:

1. the hidden layer is trained by selecting the centers and widths of the kernel functions associated with the hidden neurons
2. the weights corresponding to the connections between the hidden neurons and the output neurons are defined by solving the equation 4.11.

### 4.2.1 Centers selection

For relatively small training a neuron is generated for each data of the training set and the center  $x_i$  of each neuron is chosen randomly between the data of the training set. When the training set is composed of too many data, generating a neuron for each data of the training set might result in a too time-consuming artificial neural network. In that case, the number of generated hidden neuron might be lower than the number of training set data and the  $x_i$  of each neuron is chosen using the *K-means* clustering technique.

*K-means* clustering [28] is a method commonly used to automatically partition a dataset into  $\kappa$  groups. It proceeds by selecting  $\kappa$  initial cluster centers and, then, iteratively refining them as follows:

1. Each instance  $d_i$  is assigned to its closest cluster center
2. Each cluster center is updated to be the mean of its constituent instances

The algorithm converges when there is no further change in assignment of instances to cluster.

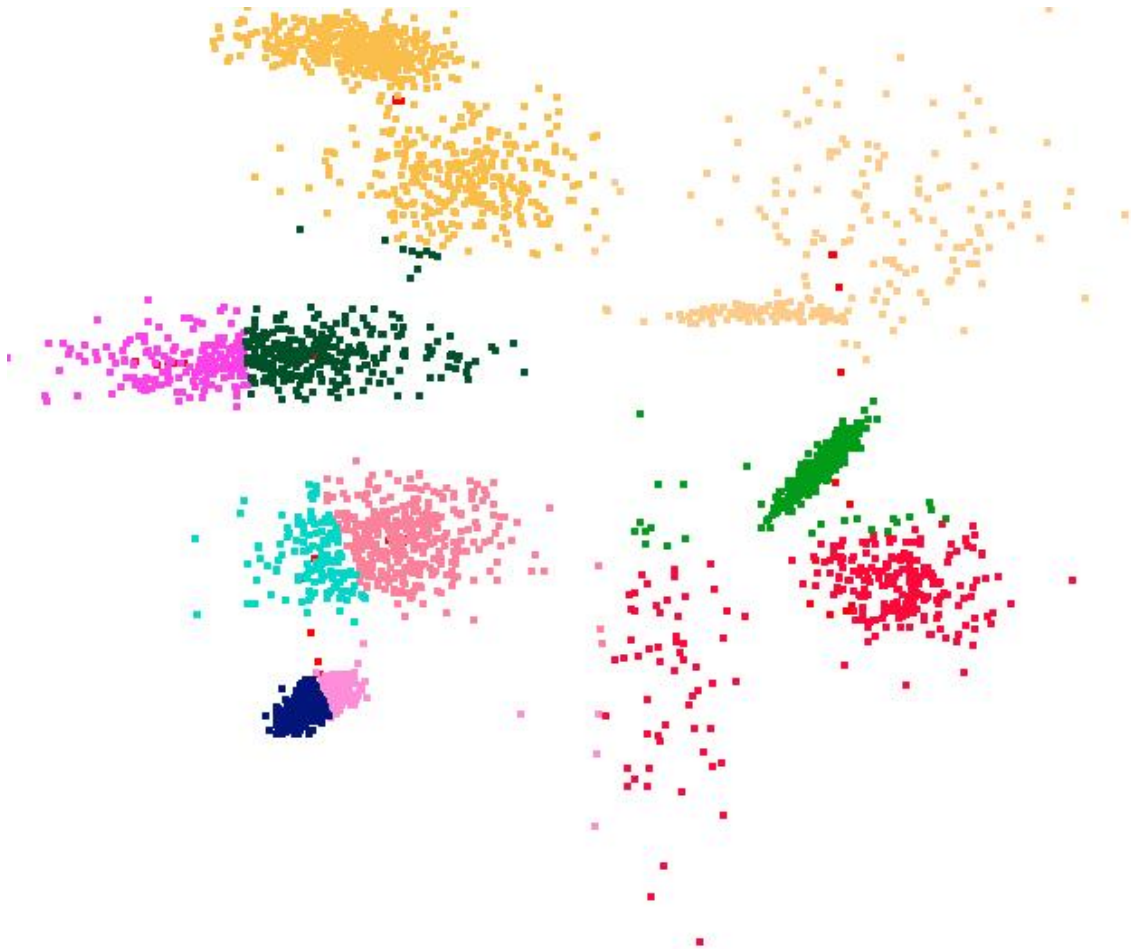


Figure 4.2. An example of K-means clustering

### 4.2.2 Widths selection

The width of a certain hidden neuron can be chosen as the standard deviation computed over all the training samples. However, this strategy may lead to the generation of narrow, not overlapping, radial basis functions and affect the generalization ability of the network. In order to overcome this problem, in the current study, the *p*-nearest neighbor (p-nn) technique was used [21].

The p-nearest neighbor algorithm finds, for each center  $x_i$  of the neural neural, the p-nearest centers (in our case  $p=4$ ) according to Euclidean norm. Then, the mean distance between  $x_i$  and the p-nearest centers is taken as the width  $\sigma_i$  of the  $i$ -th hidden neuron. This allows some overlapping between the hidden neurons and aims at increasing the generalization capabilities of the neural network.

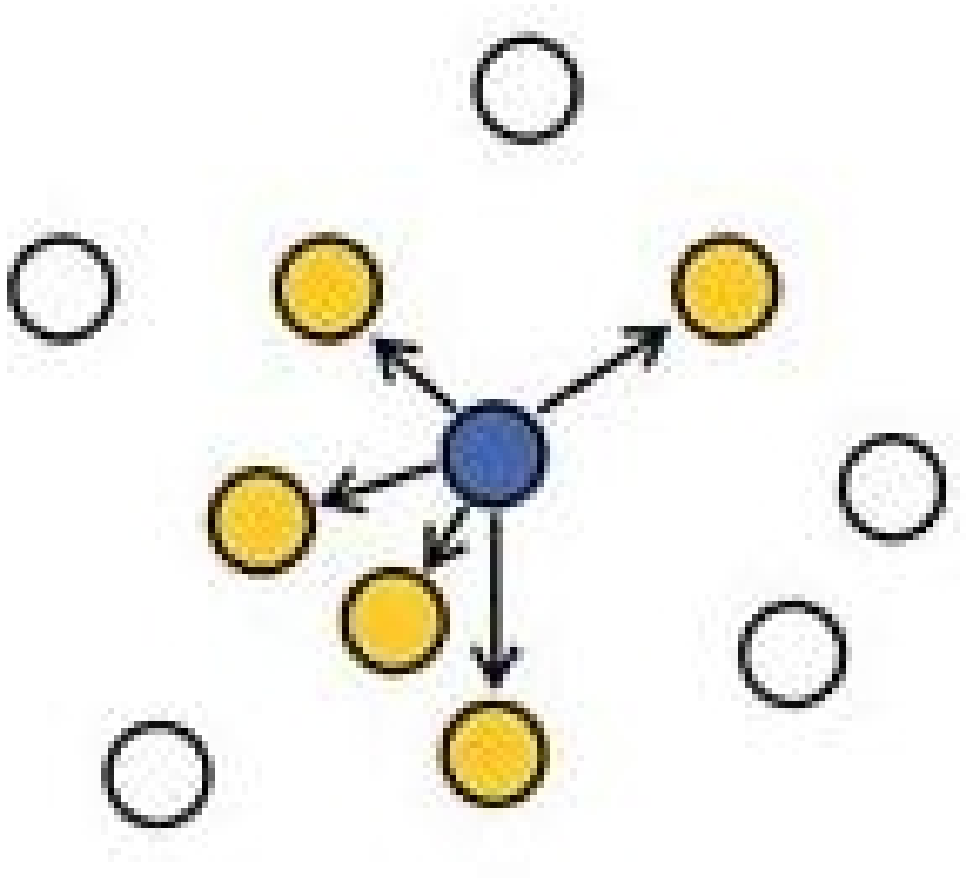


Figure 4.3. p-nearest neighbor

### 4.2.3 Weight selection

The weights  $w_i = 1, 2, \dots, m_1$  must be found in order to minimize the cost function:

$$\xi(F) = \sum_{i=1}^N \left( d_i - \sum_{j=1}^{m_1} w_j G(\|x - t_j\|) \right)^2 + \lambda \|DF\|^2 \quad (4.4)$$

The first term on the right of the equal sign can be expressed as the Euclidean norm of  $\|d - Gw\|^2$ , being:

$$d = [d_1 \quad d_2 \quad \dots \quad d_N] \quad (4.5)$$

$$G = \begin{bmatrix} G(x_1, t_1) & G(x_1, t_2) & \dots & G(x_1, t_{m_1}) \\ G(x_2, t_1) & G(x_2, t_2) & \dots & G(x_2, t_{m_1}) \\ \vdots & \vdots & \ddots & \vdots \\ G(x_N, t_1) & G(x_N, t_2) & \dots & G(x_N, t_{m_1}) \end{bmatrix} \quad (4.6)$$

$$w = [w_1 \quad w_2 \quad \dots \quad w_{m_1}] \quad (4.7)$$

which, overlooking some middle passages, becomes:

$$\|DF\|^2 = w^T G_0 w \quad (4.8)$$

where  $G_0$  is a symmetrical  $m_1 \times m_1$  matrix defined as:

$$G_0 = \begin{bmatrix} G(t_1, t_1) & G(t_1, t_2) & \dots & G(t_1, t_{m_1}) \\ G(t_2, t_1) & G(t_2, t_2) & \dots & G(t_2, t_{m_1}) \\ \vdots & \vdots & \ddots & \vdots \\ G(t_N, t_1) & G(t_N, t_2) & \dots & G(t_N, t_{m_1}) \end{bmatrix} \quad (4.9)$$

Finally, minimizing the equation 4.4 in respect to the weights vector  $w$  we arrive at:

$$(G^T G + \lambda G_0)w = G^T d \quad (4.10)$$

which, when  $\lambda \rightarrow 0$ , becomes:

$$w = G^+ d \quad (4.11)$$

which solves the learning of the neural network weights.  $G^+$  is the pseudo-inverse matrix of  $G$  defined as:

$$G^+ = (G^T G)^{-1} G^T \quad (4.12)$$

# Chapter 5

## The genetic algorithm

Several engineering problems have a multi-objective formulation for which is not possible to find a single solution which simultaneously optimizes all the objectives but rather alternative solutions lying on or near the Pareto optimal front.

For that reason, during the past decade, several multi-objective genetic algorithms have been proposed due to their ability to find multiple Pareto-optimal solutions in one single run as they mimic the evolutionary processes of ecosystems, which obey the Darwinian idea of *survival of the fittest*, moving the Pareto front towards the ideal optimal set of solutions as the optimization process evolves.

The non dominated sorting genetic algorithm NSGA-II [24], whose theoretical background is described in section 5.1, was used in current study since the optimal solutions of the DI Diesel combustion engine are the non dominated ones, being NO<sub>x</sub>, soot and gross-IMEP linked together by trade-off relationships.

Starting from the NSGA-II genetic algorithm, a specific software (in Matlab/Octave language) was developed in order to manage a main loop which relies upon RBF neural networks for the evaluation phase of the genetic algorithm while the determination of the fittest individuals, generation after generation, is demanded to the NSGA-II genetic algorithm.

## 5.1 The NSGA-II genetic algorithm

In order to sort a population of size  $N$  according to the level of non-domination, each solution must be compared with every other solution in the population to find if it is dominated. This requires  $O(mN)$  comparison for each solution, where  $m$  is the number of objectives. When this process is continued to find the members of the first non-dominated class for all population member, the total complexity is  $O(mN^2)$ . Then, the procedure must be repeated to find the subsequent fronts. In worst case the complexity of this algorithm is  $O(mN^3)$ .

The non-dominated sorting genetic algorithm (NSGA-II) proposed by Deb. et al. is a multi-objective genetic algorithm characterized by a fast non-dominated sorting approach which requires at most  $O(mN^2)$  and when applied on a population  $P$  returns a list of the non-dominated fronts  $F$ .

### 5.1.1 Sorting algorithm

First, for each solution two entities are calculated:

1.  $n_i$  the number of solutions which dominate the solution  $i$
2.  $S_i$  a set of solution which the solution  $i$  dominates

The calculation of these two entities requires  $O(mN^2)$  comparisons. Then, all those points having  $n_1 = 0$  are identified and put in a list  $F_1$  which forms the current front. Then, for each solution in the current front each member  $j$  in its  $S_i$  is visited and its  $n_j$  count is reduced by one. During this process, if for any member  $j$  the count becomes 0, this one is put in a separate list  $H$ . Then, the process continues using the newly identified front  $H$  as current front while the members in the list  $F_1$  are declared member of the first front. these iterations require  $O(N)$  computations. Finally, the process ends when all fronts are identified. The worst case complexity of this loop is  $O(N^2)$  and, thus, the overall complexity of the algorithm is  $O(mN^2) + O(N^2)$  or  $O(mN^2)$ .

A synthetic representation of the *fast non dominated sorting algorithm* is shown below:

```

for each  $p \in P$ 
for each  $q \in P$ 
if  $(p < q)$  then
     $S_p = S_p U q$ 
else if  $(q < p)$  then
     $n_p = n_p + 1$ 
    if  $n_p = 0$  then
         $F_1 = F_1 U p$ 
         $i = 1$ 
while  $F_i \neq 0$   $H = 0$ 
for each  $p \in F_1$ 
for each  $q \in S_p$ 
     $n_q = n_p + 1$ 
if  $n_q = 0$  then  $H = H U q$ 
     $i = i + 1$ 
     $F_i = H$ 

```

(5.1)

### 5.1.2 Density estimation

To get an estimate of the density of solutions surrounding a certain point in the population the average distance of the two points on either side of this point along each of the objectives is taken. The entity  $i_{distance}$  is taken as an estimate of the largest cuboid enclosing the point  $i$  without including any other point in the population and is called *crowding distance*. In fig. 5.1 the crowding distance of the  $i$  – *th* solution in its front (marked with solid circles) is the average side-length of the cuboid(represented by a dashed box).

In order to calculate the crowding distance of each point in the set  $I$  the following algorithm is used:

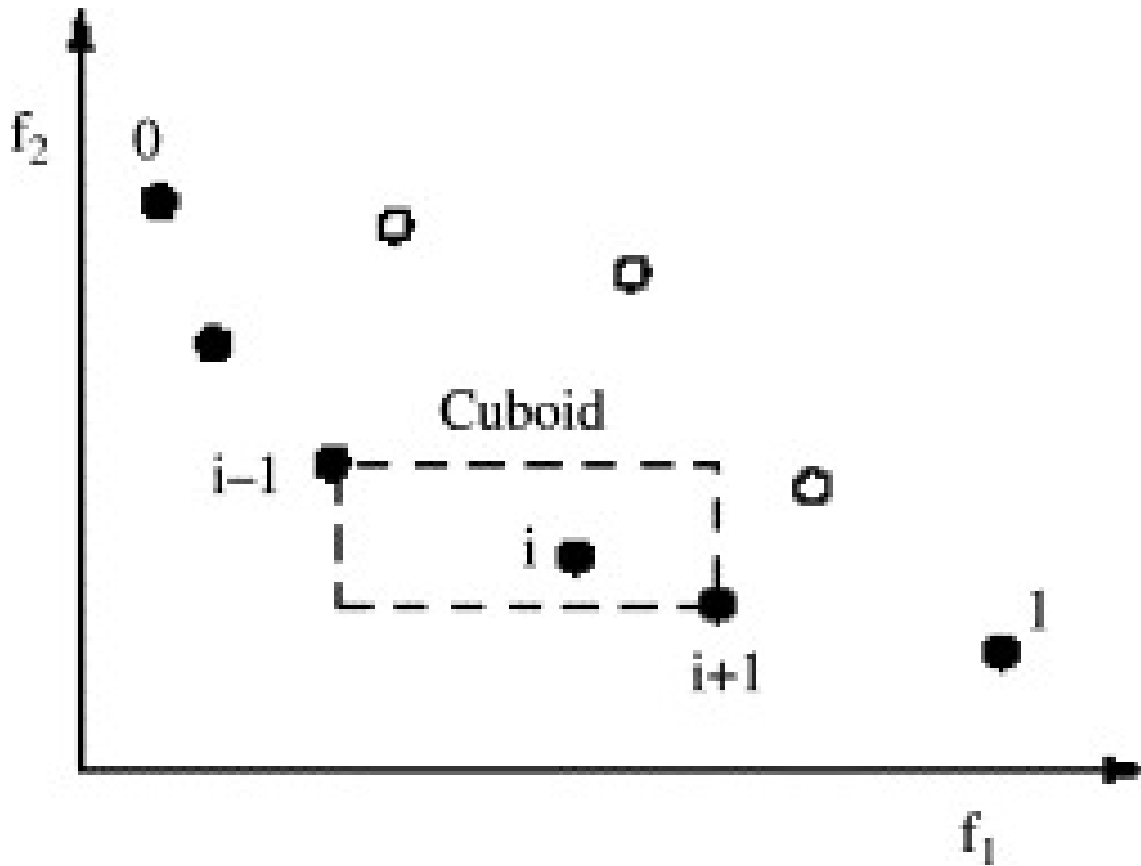


Figure 5.1. Crowding distance

$$\begin{aligned}
 l &= |I| \\
 &\text{for each } i \text{ set } I[i]_{\text{distance}} \\
 &\text{for each objective } m \\
 I &= \text{sort}(I, m) \\
 I[1]_{\text{distance}} &= I[l] = \text{inf} \\
 &\text{for } i = 2 \text{ to } (l - 1) \\
 I[1]_{\text{distance}} &= I[1]_{\text{distance}} + (I[i + 1].m - I[i - 1].m)
 \end{aligned} \tag{5.2}$$

where  $I[i].m$  refers to the  $m$ -th objective function value of the  $i$ -th individual in the set  $I$ . The complexity of this procedure is governed by the sorting algorithm. In the worst case, the sorting requires  $O(mN \log N)$  computations.

### 5.1.3 Crowded comparison operator

The crowded comparison operator ( $\geq_n$ ) the selection process at various stages of the algorithm towards a uniformly spread out Pareto-optimal front.

Each individual  $i$  in the population has two attributes:

- the non-domination rank ( $i_{rank}$ )
- the local crowding distance ( $i_{distance}$ )

Thus, a partial order  $\geq_n$  can be defined as:

$$\begin{aligned}
 & i \geq_n j \\
 & \text{if } (i_{rank} < j_{rank}) \text{ or } ((i_{rank} = j_{rank}) \text{ and } (i_{distance} > j_{distance}))
 \end{aligned} \tag{5.3}$$

which means that between two solutions with differing non-dominating rank the point with the lower rank is preferred. Otherwise, if both the points belong to the same front the point which is located in a region with lesser number of points is preferred (the highest crowding distance).

### 5.1.4 The main loop

Firstly, a parent population  $P_0$  is created. This population is sorted based on the non-domination. Each solution is assigned a fitness equal to its non-domination level. A non-domination level of 1 represents the best level, thus, minimization of fitness is assumed. Then, evolutionary operators such as binary tournament selection and mutation are used to create a child population  $Q_0$  of size  $N$ . From the first generation onward, in order to ensure elitism, the procedure is changed as follows:

$$\begin{aligned}
 & R_t = P_t \cup Q_t \\
 & F = \text{fast - nondominated - sort } (R_t) \\
 & \text{until } |P_{t+1}| < N \\
 & \text{crowding - distance - assignment } (F_i) \\
 & P_{t+1} = P_{t+1} \cup F_i \\
 & \text{Sort}(P_{t+1}, \geq_n) \\
 & P_{t+1} = P_{t+1}[0 : N] \\
 & Q_{t+1} = \text{make - new - pop } (P_{t+1}) \\
 & t = t + 1
 \end{aligned} \tag{5.4}$$

First, a combined population  $R_t = P_t \cup Q_t$  (where  $R_t$  is composed of  $2N$  members). Then, the population  $R_t$  is sorted according to non-domination. A new population  $P_{t+1}$  is formed by adding solutions from the first front till the size exceeds  $N$ . Thereafter, the solutions of the last accepted front are sorted according to  $\geq_n$  and the first  $N$  members are picked. This procedure builds the population  $P_{t+1}$  of size  $N$  which is used to create a new population  $Q_{t+1}$  of size  $N$  by means of selection, crossover and mutation operators.

The basic operations being performed and the worst case complexities associated with are as follows:

- non-dominated sort is  $O(mN^2)$
- crowding distance assignment is  $O(mN \log N)$
- sort on  $\geq_n$  is  $O(2N \log(2N))$

thus, the overall complexity of the algorithm is  $O(mN^2)$ .

The diversity among non dominated solutions is ensured by using the crowding comparison procedure.

# Chapter 6

## RBF neural networks training

Starting from the values of the input variables  $P_{boost}$ , SR, EGR SOI reported in table 2.2 a *full factorial* design of experiment of 81 CFD three-dimensional combustion calculations was generated for each investigated piston bowl in order to provide an adequate training set for the learning processes of the radial basis functions neural networks, resulting in a total of 243 CFD simulations. Training sets of the piston bowls G012, NE, VHP011 were kept separated to train different neural networks for each piston bowl. Proceeding in that way, each neural network was used as a meta-model of the combustion development inside a specific piston bowl allowing to clearly separate the influence of the piston shape, which affect the spray/wall interaction, from the influences of the input variables.

A *full factorial* design of experiment was chosen so that the input variables were non correlated each others which made it suitable for a statistical analysis of the influence of the input variables of the engine outputs.

Before the neural network training process, a Student test was used to verify that the chosen input variables could actually affect NOx, soot and gross-IMEP of the engine and, eventually, discard those variables having a small influence on engine outputs. Moreover, Student charts can provide an insight of how the combustion development inside each piston bowl react to a variation of the input variables in terms of emissions and performance.

## 6.1 Influence of the input variables on engine gross-IMEP

Figures 6.1, 6.2, 6.3 show the influence of the input variables on engine gross-IMEP for the piston bowls G012, VHP011 NE respectively.

All the three investigated piston bowls are affected, on a quality level, in the same way by a variation of the input variables:

- an increase of the boost pressure results in an increase of engine performance
- an increase of the swirl ratio results in a significant decrease of engine gross-IMEP
- an increase of the exhaust gas recirculation leads to a decrease of performance
- a variation of the start of injection has a small influence on gross-IMEP

However, gross-IMEP of the piston bowl NE is definitely less influenced by a variation of the swirl ratio (-0.8 bar) than the one of the piston bowls G012 and VHP011 (-2 bar,-2.6 bar respectively).

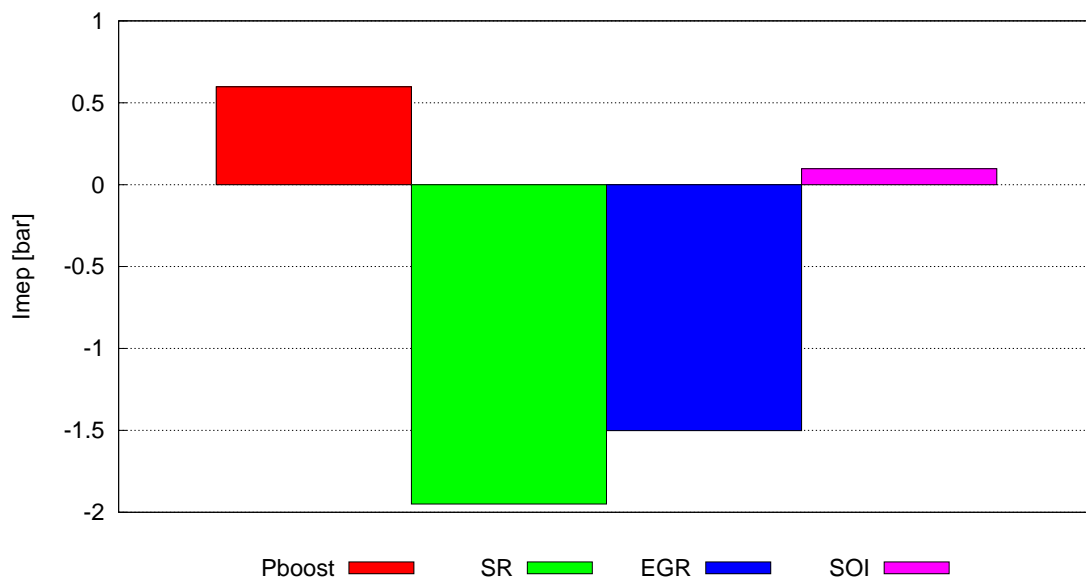


Figure 6.1. G012: influence of the input variables on gross-IMEP

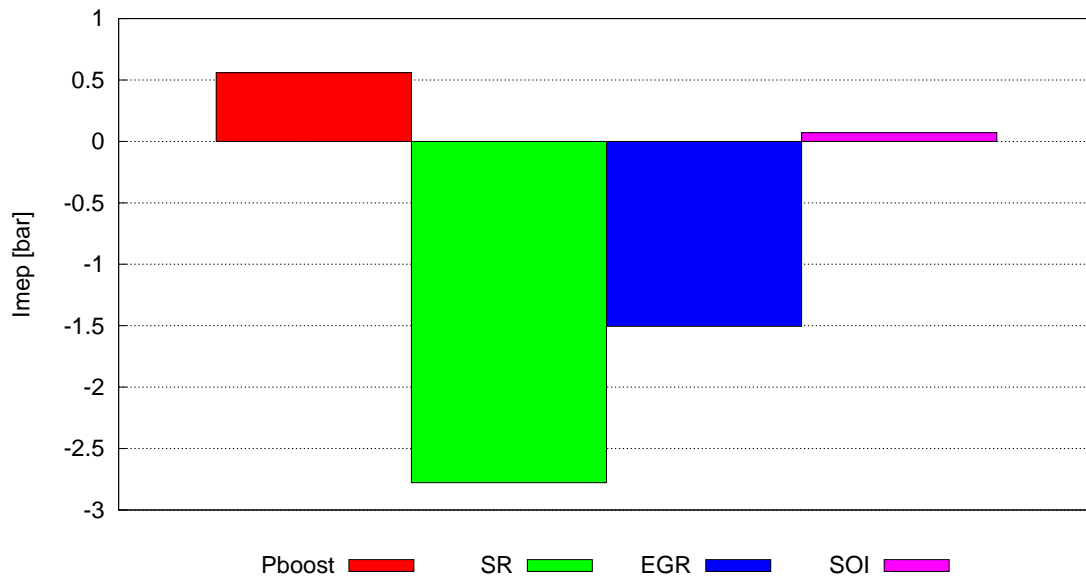


Figure 6.2. VHP011: influence of the input variables on gross-IMEP

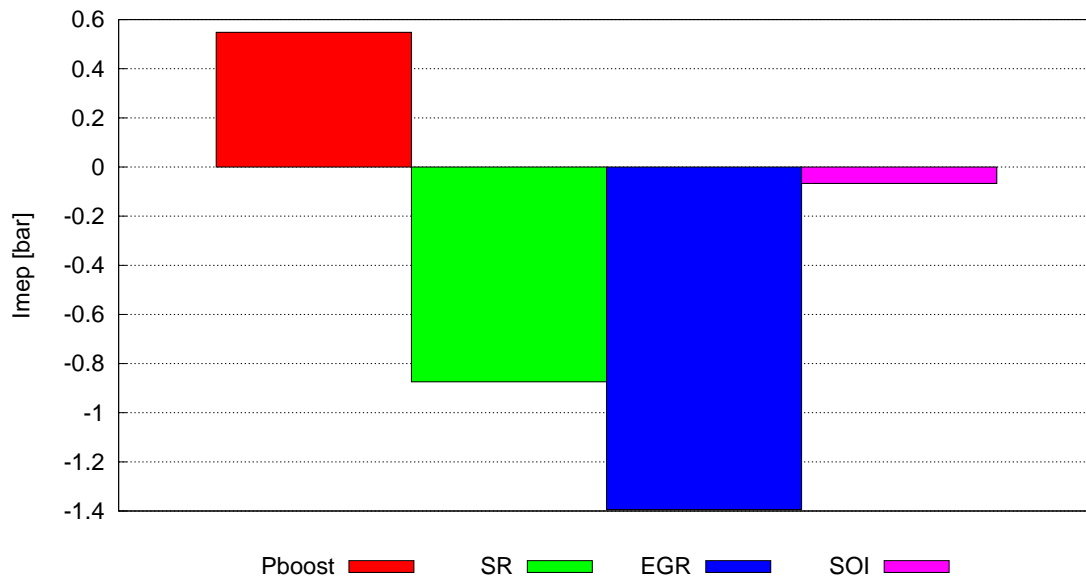


Figure 6.3. NE: influence of the input variables on gross-IMEP

## 6.2 Influence of the input variables on engine NOx emission

Figures 6.4, 6.5, 6.6 show the influence of the input variables on engine gross-IMEP for the piston bowls G012, VHP011 NE.

All the three investigated piston bowls show the approximately the same influence of the input variables on NOx emission:

- an increase of boost pressure has a small influence on engine NOx emission
- an increase of swirl ratio results in a decrease of NOx emission due to a less efficient combustion development
- an increase of exhaust gas recirculation allows a strong reduction of engine NOx emission
- An increase of start of injection (i.e. postponing the main injection) also allows a significant decrease of NOx emission

As far as NOx emission are concerned, the main differences between the investigated piston bowls responses were recorded for variation of the swirl ratio. Particularly, the effect of the swirl ratio on the piston bowl VHP011 was -1.4 g/kWh while the piston bowls G012 and NE recorded a decrease of -0.3 g/kWh and -0.5 g/kWh respectively.

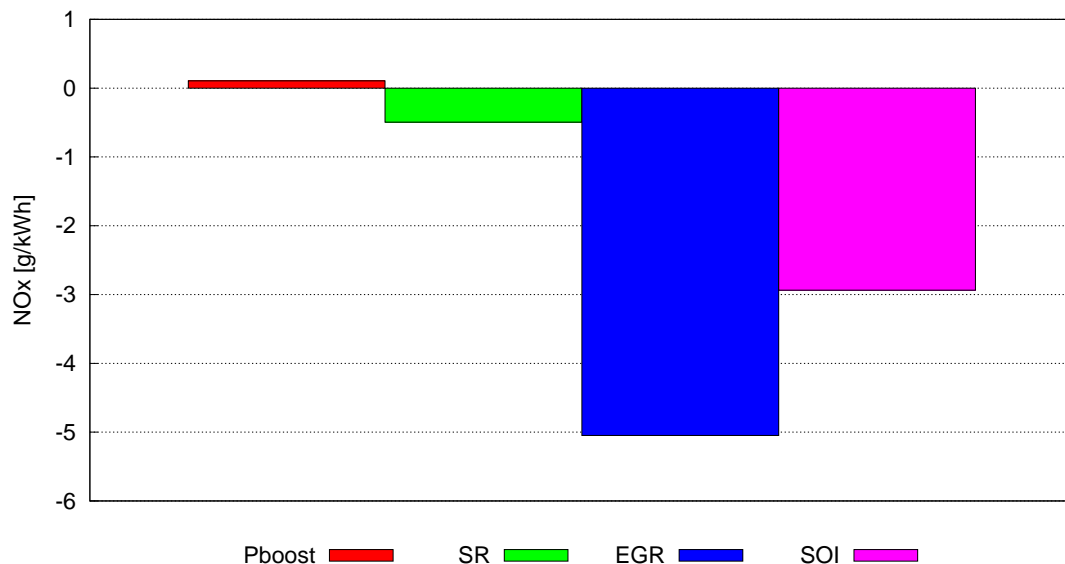


Figure 6.4. G012: influence of the input variables on NOx

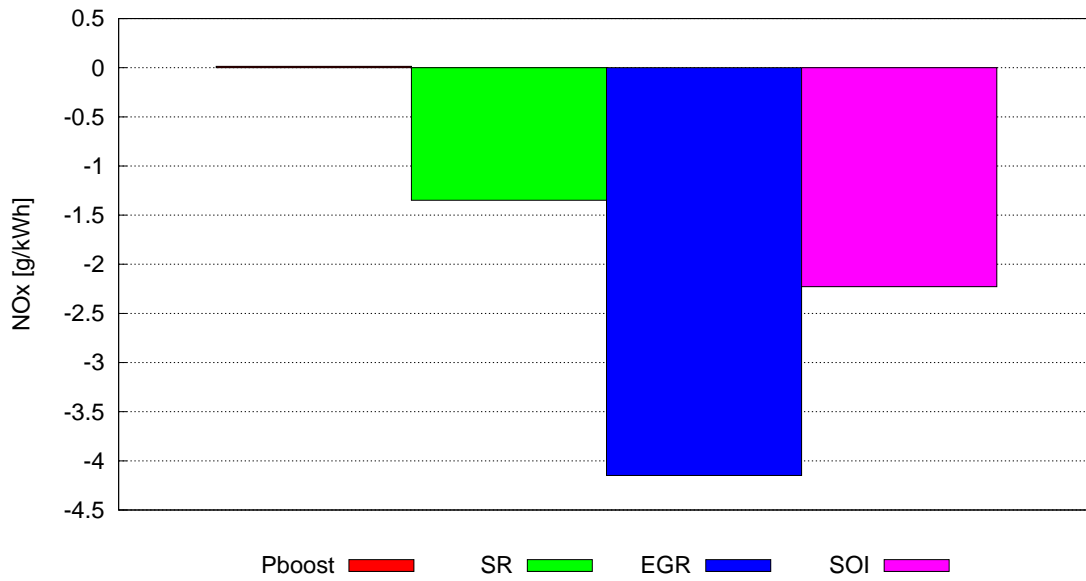


Figure 6.5. VHP011: influence of the input variables on NOx

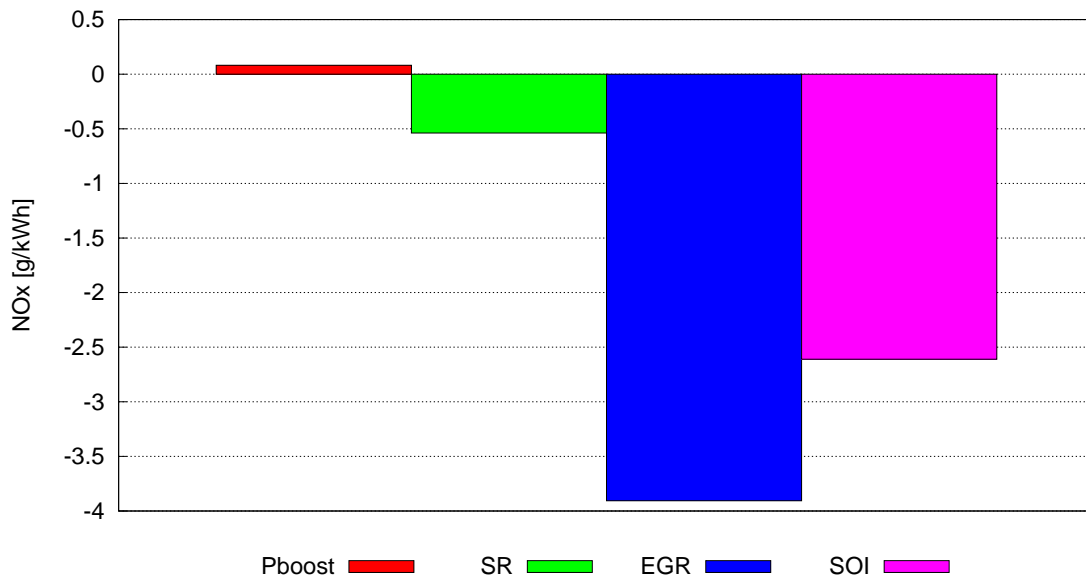


Figure 6.6. NE: influence of the input variables on NOx

### 6.3 Influence of the input variables on engine soot emission

Figures 6.7, 6.8, 6.9 show the influence of the input variables on engine gross-IMEP for the piston bowls G012, VHP011 NE.

Soot emission of the three piston bowls is affected in a similar way by a variation of the input variables:

- a variation of the boost pressure has a small influence on engine soot emission
- an increase of swirl ratio results in an increase of engine soot emission for the piston bowls G012 and VHP011 while the piston bowl NE react to an increase of swirl ratio with a decrease of soot emission
- an increase of exhaust gas recirculation leads to an increase of soot emission
- by postponing the start of injection a reduction of soot emission is recorded

As far as soot emission are concerned, the main differences between the responses of different piston bowls to a variation of the input parameters were recorded for variation of the swirl ratio. Particularly, the swirl ratio effect on the piston bowl VHP011 was +0.25 g/kWh while the piston bowls G012 and NE which show lower effects (+0.1 g/kWh, -0.02 g/kWh respectively).

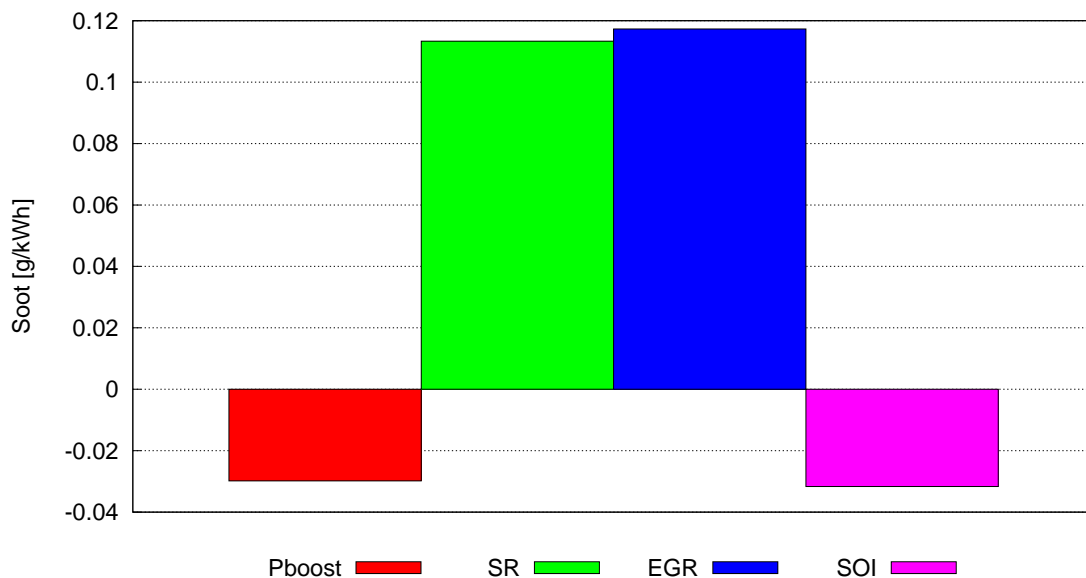


Figure 6.7. G012: influence of the input variables on soot

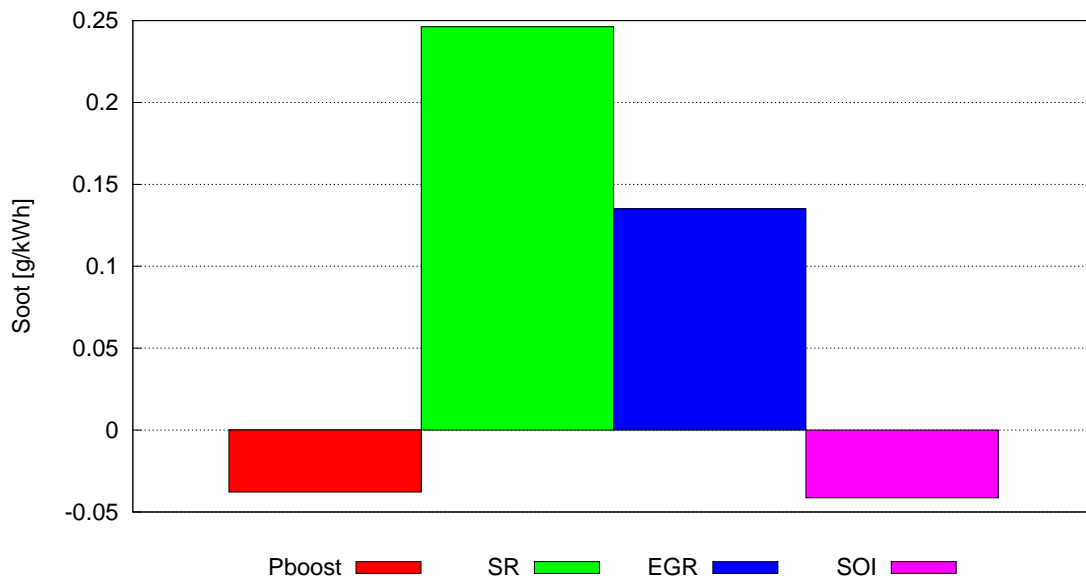


Figure 6.8. VHP011: influence of the input variables on soot

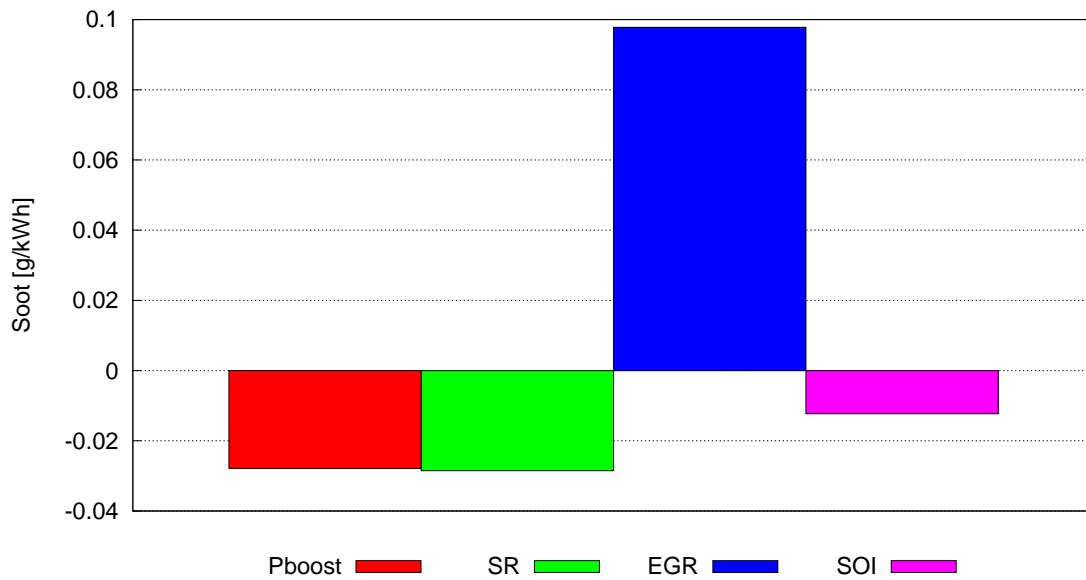


Figure 6.9. NE: influence of the input variables on soot

## 6.4 RBF neural networks validation

In order to validate the neural networks and to verify their capability to forecast engine performance and emissions as a function of the input variables, the training sets of 81 CFD three-dimensional calculations of each piston bowl were divided into two different parts:

- the first part of each training set, composed of 78 data, was used to train the related neural network
- the remaining part of each training set, composed of 3 data, was instead use to validate the related neural network

Figures 6.10, 6.11, 6.12 show the relative error between the forecasted values of NO<sub>x</sub>, soot and gross-IMEP of the neural networks and the actual ones of the validation sets.

As it can be seen, all the trained neural networks evaluate the engine gross-IMEP with a very good precision (the highest relative error was 1.5%) while the evaluation of engine emissions records highest relative errors varying from about 2% through about 8%.

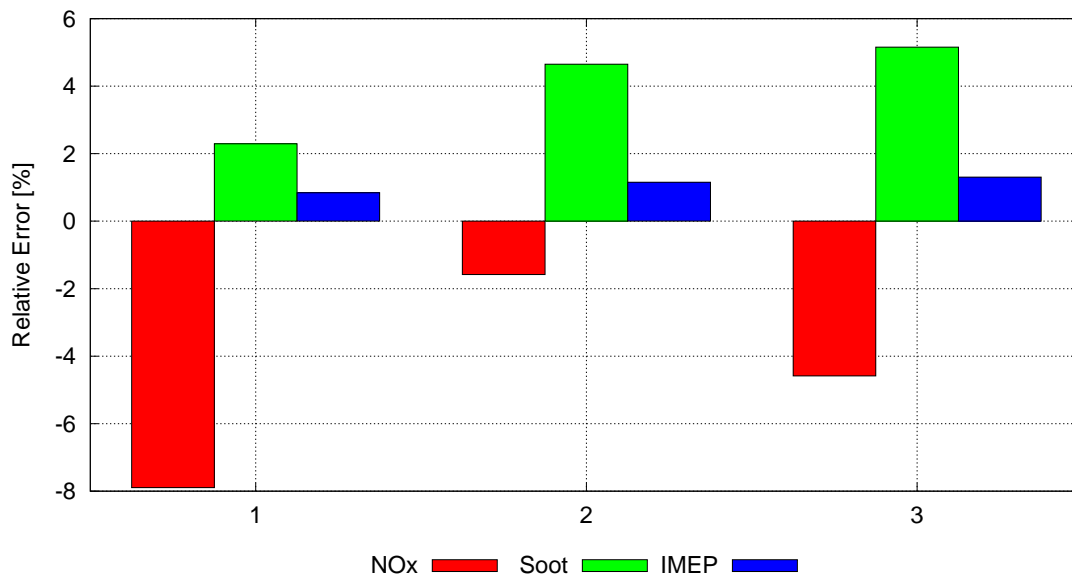


Figure 6.10. G012 neural network validation

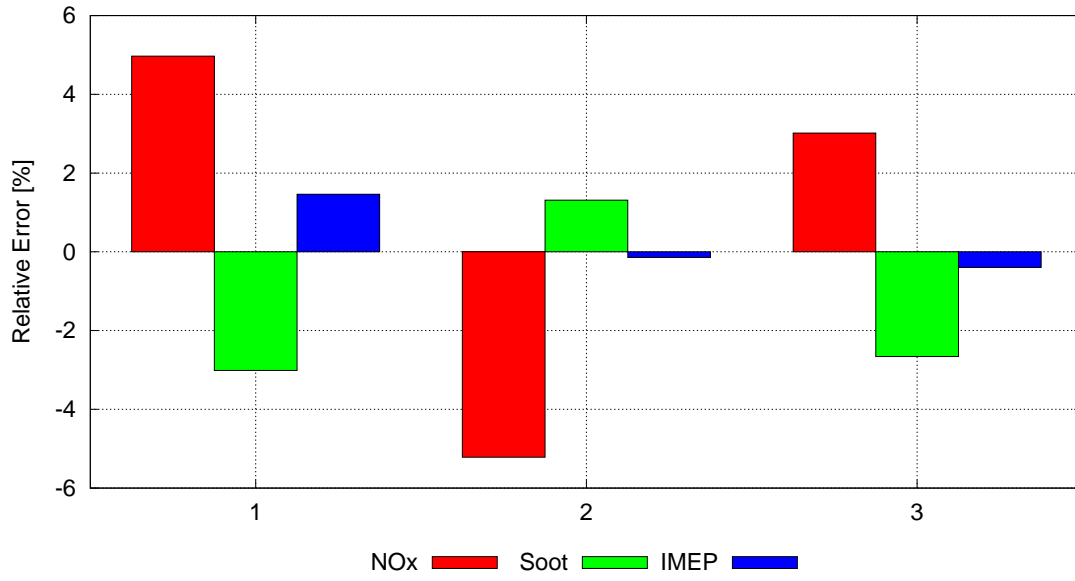


Figure 6.11. VHP011 neural network validation

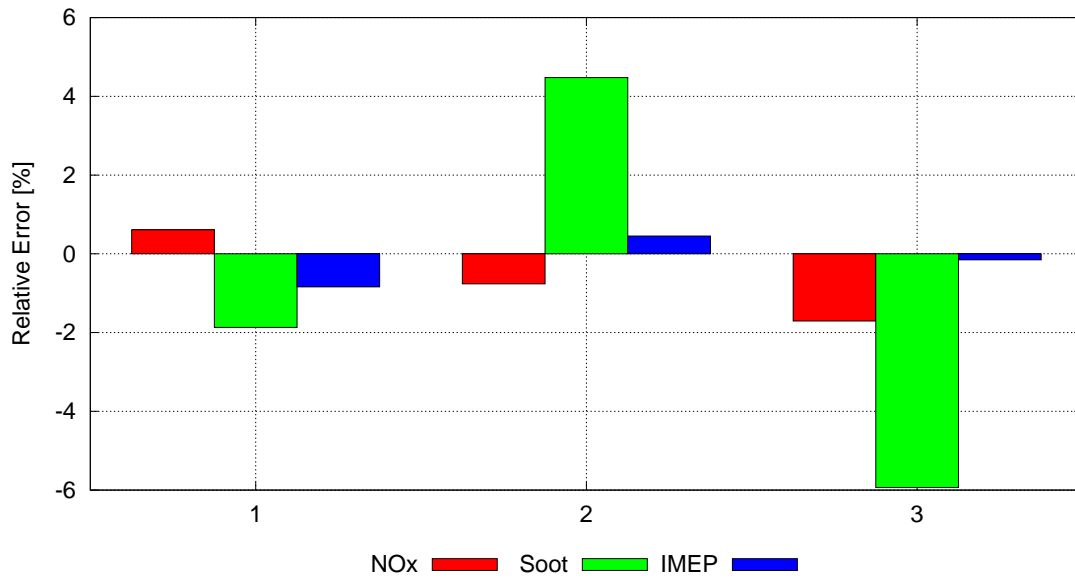


Figure 6.12. NE neural network validation

## Chapter 7

# Multi-objective optimization of the piston bowls

Once that three different neural networks were adequately trained, a multi-objective genetic algorithm optimization was performed for each piston bowl separately. For each optimization an initial population of seventy two individuals was randomly generated in order to provide the first generation which was needed as the beginning point for the optimization. Then, the evolutionary process advanced for one hundred generations aiming at the simultaneously reduction of soot and NOx emissions while increasing the engine gross-IMEP. Overall, seven thousands and two hundreds individuals, for each piston bowl, were *virtually* examined by means of the RBF neural networks, drastically cutting computational time.

In figures 7.1, 7.3, 7.5, which show the emissions in the soot-NOx plane, of each investigated individual for the piston bowls G012, VH011 and NE respectively, can be seen one of the main result of the genetic algorithm multi-objective optimization: the definition of the Pareto frontier of all the three piston bowls. In the current work, since the optimization had three different objectives (minimizing NOx and soot emissions and maximizing the gross-IMEP) the geometrical locus of the Pareto optimal solutions was actually a two dimensional surface, however, it was chosen to represent the Pareto frontier in the soot-NOx plane due to the fact that in industrial applications emissions are usually a more pressing commitment than the achievement of the power target of the engine which is, though, still desirable. Thus, during the evolutionary process, virtual individuals were advanced through generations according also to their gross-IMEP, as shown in 7.2, 7.4, 7.6.

Amongst the Pareto optimal solutions it is also possible to identify the minimum NOx individuals, the minimum soot individuals and the trade-off individuals whose input parameters and outputs are reported in tables 7.1, 7.2 , 7.3. It worth notice how, while the minimum NOx individuals of all the three investigated piston bowls

presented the same input parameters, trade-off individuals and minimum soot individuals were obtained with different input parameters for each piston bowls justifying the need of a wide range investigation in order to compare properly different bowl. Particularly, the piston bowl NE showed the tendency to require a higher swirl ratio (1.6 for the trade-off individual, 1.54 for the minimum soot individual) than the other two piston bowls. On the contrary, the piston bowl VHP011 trade-off and minimum soot individuals required a lower swirl ratio (1.3 for the trade-off individual, 1.2 for the minimum soot individual).

| Bowl   | $P_{boost}$ | SR  | EGR [%] | SOI [deg. ATDC] | NOx [g/kWh] | Soot [g/kWh] | IMEP [bar] |
|--------|-------------|-----|---------|-----------------|-------------|--------------|------------|
| G012   | 3.25        | 2.0 | 15.0    | -6.0            | 1.32        | 0.30         | 15.9       |
| VHP011 | 3.25        | 2.0 | 15.0    | -6.0            | 1.00        | 0.43         | 14.8       |
| NE     | 3.25        | 2.0 | 15.0    | -6.0            | 0.88        | 0.17         | 16.4       |

Table 7.1. Minimum NOx individuals

| Bowl   | $P_{boost}$ | SR  | EGR [%] | SOI [deg. ATDC] | NOx [g/kWh] | Soot [g/kWh] | IMEP [bar] |
|--------|-------------|-----|---------|-----------------|-------------|--------------|------------|
| G012   | 3.39        | 1.5 | 13.0    | -6.6            | 1.9         | 0.11         | 18.5       |
| VHP011 | 3.33        | 1.3 | 12.0    | -6.0            | 2.0         | 0.13         | 17.7       |
| NE     | 3.39        | 1.6 | 10.0    | -6.0            | 2.0         | 0.07         | 18.6       |

Table 7.2. Trade-off individuals

| Bowl   | $P_{boost}$ | SR   | EGR [%] | SOI [deg. ATDC] | NOx [g/kWh] | Soot [g/kWh] | IMEP [bar] |
|--------|-------------|------|---------|-----------------|-------------|--------------|------------|
| G012   | 3.39        | 1.3  | 5.1     | -11.4           | 9.6         | 0.04         | 20.0       |
| VHP011 | 3.39        | 1.2  | 5.0     | -9.6            | 6.9         | 0.06         | 19.0       |
| NE     | 3.39        | 1.54 | 5.0     | -9.0            | 5.0         | 0.05         | 19.6       |

Table 7.3. Minimum soot individuals

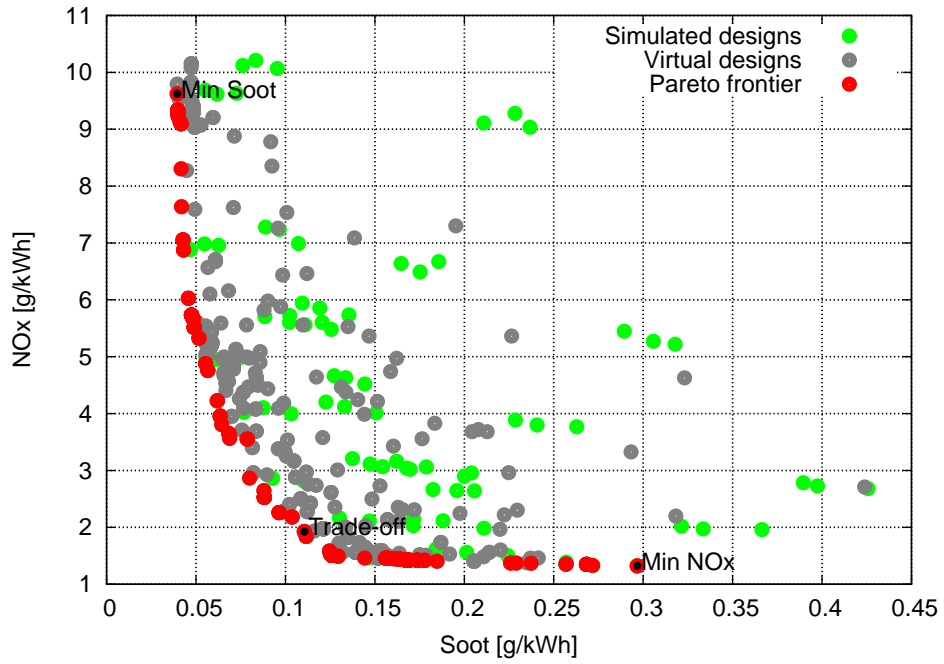


Figure 7.1. soot - NOx

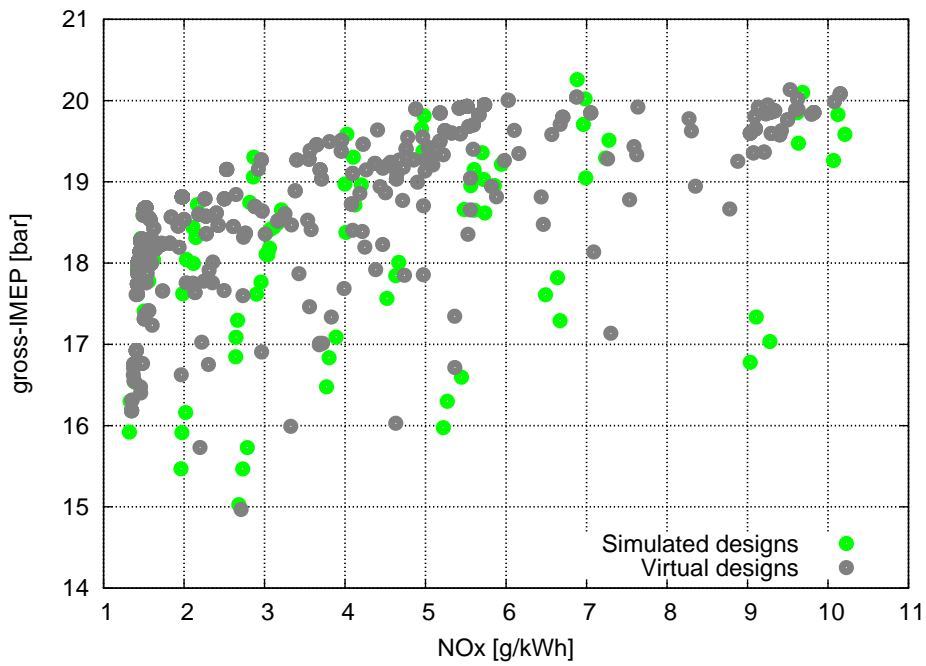


Figure 7.2. NOx - IMEP

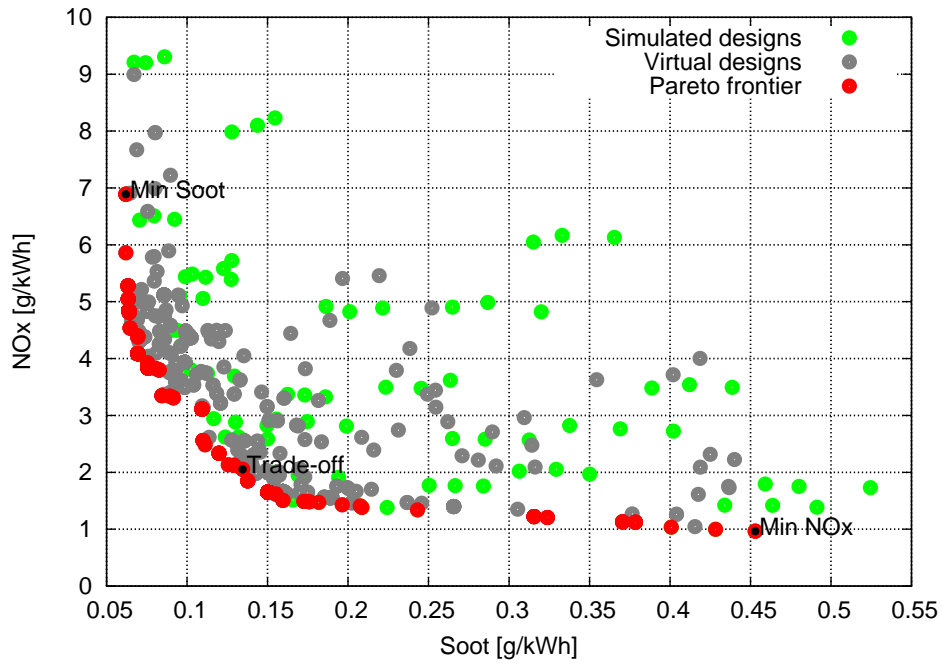


Figure 7.3. soot - NOx

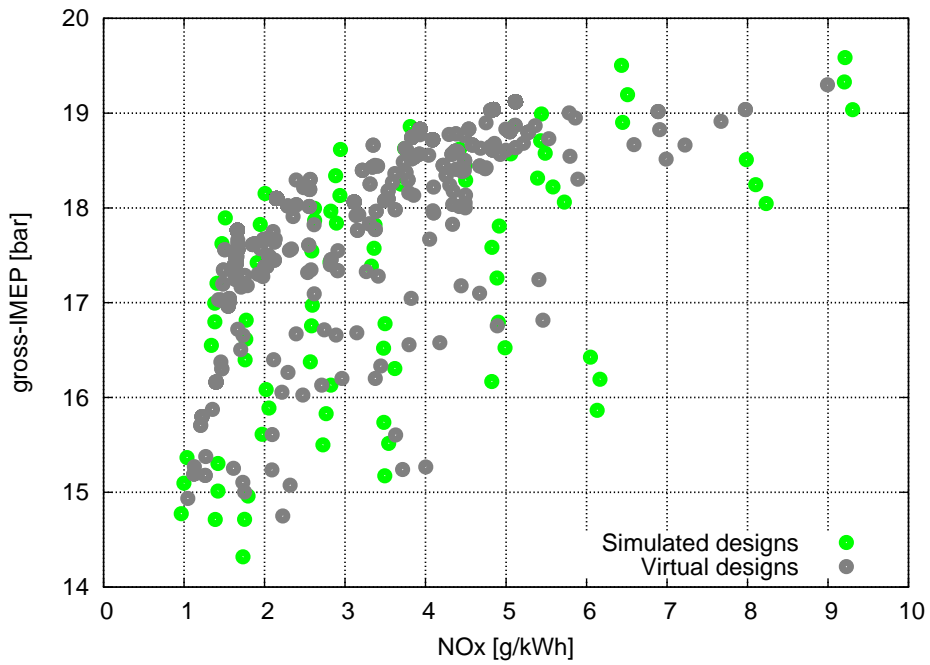


Figure 7.4. NOx - IMEP

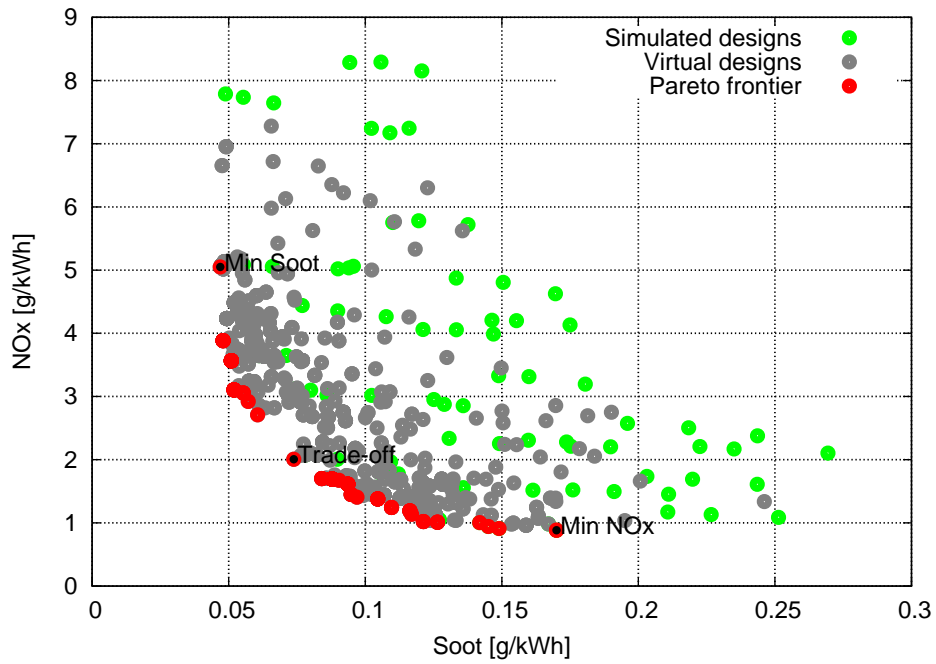


Figure 7.5. soot - NOx

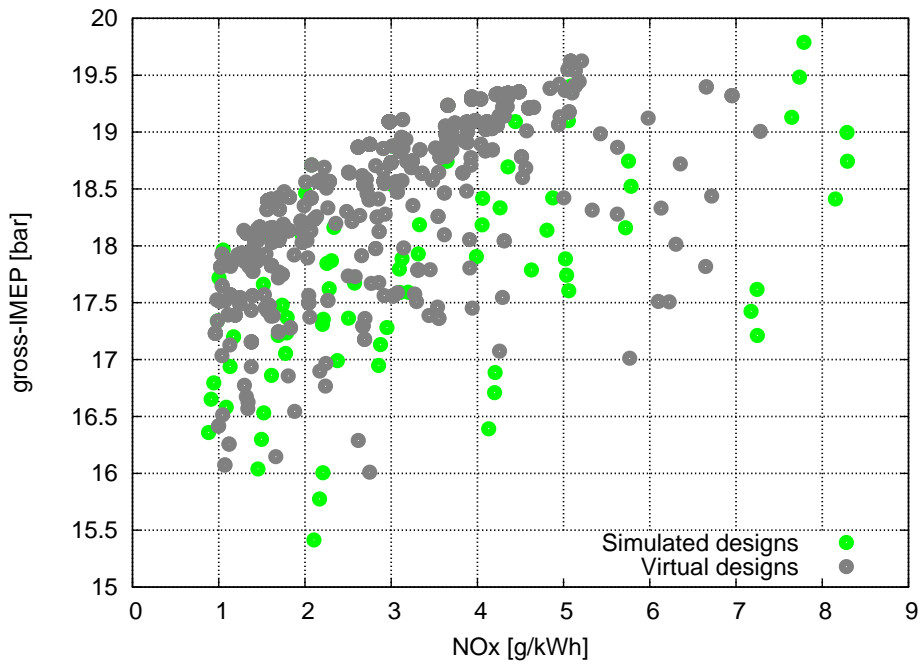


Figure 7.6. NOx - IMEP

## 7.1 Comparison between the Pareto frontiers

Since it exists a trade-off relationship between NO<sub>x</sub> and soot emissions the optimization of the combustion development inside a DI Diesel does not have a unique solution but rather different Pareto optimal solutions which might represent an equally valid choice for the engine depending on the chosen after-treatment devices. For that the reason, the definition of the Pareto frontier of each piston bowl by means of genetic algorithm multi-objective optimizations is of great practical value allowing to compare emissions and performance of the investigated piston bowls under a range of operating conditions as wide as possible and, eventually, to choose the best individual for each piston once that the after treatment strategy is defined.

Figure 7.7 shows a comparison between the Pareto frontiers of the piston bowl G012, VHP011 and NE in the soot-NO<sub>x</sub> plane. As it can be seen, the piston bowl NE is definitely better, in term of emissions, as its Pareto frontier lies south-west than the other ones which means that comparing individuals of the three Pareto frontiers having the same NO<sub>x</sub> emission, the one of the NE Pareto frontier will record a lower soot emission, otherwise, comparing individuals of the three Pareto frontiers having the same soot emission, the one of the NE Pareto frontier will record a lower NO<sub>x</sub> emission.

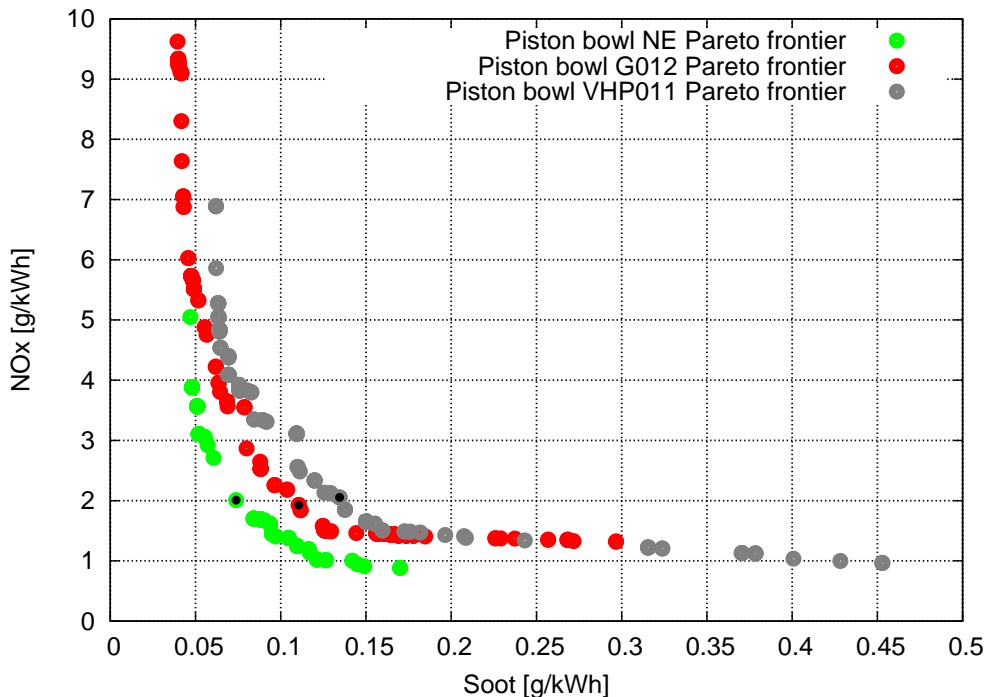


Figure 7.7. Pareto frontiers: soot-NO<sub>x</sub>

In figure 7.7 are also visible the NO<sub>x</sub>-soot trade-off individuals, pointed out by black dots. In the current study, these individuals were chosen in order to present a NO<sub>x</sub> under 2 g/kWh allowing to fulfil euro 5 NO<sub>x</sub> emission limit without the need of a specific DeNO<sub>x</sub> after-treatment device. The best individuals, one for each piston bowl were, then, validated by means of actual CFD three-dimensional combustion simulations.

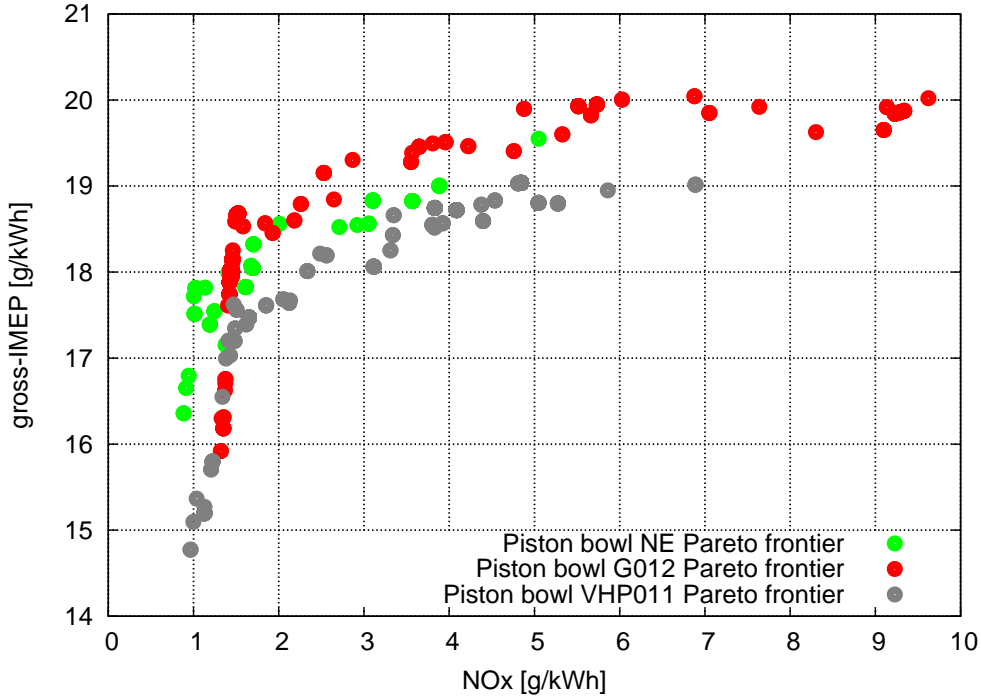


Figure 7.8. Pareto frontiers: NO<sub>x</sub>-IMEP

In tables 7.4, 7.5, 7.6 are reported the comparisons between the values of NO<sub>x</sub>, soot and gross-IMEP foreseen by means of the RBF neural networks and the actual values, resulting from CFD calculations of the best individuals. For all the three investigated piston bowls, the greatest relative error (about 10%) was made evaluating NO<sub>x</sub> emissions. Particularly, as far as NO<sub>x</sub> emissions were concerned, all the trade-off individuals recorded a lower emission than the one foreseen by the RBF neural network. On the contrary, a very good agreement between neural networks and CFD results was found both for soot emission, where a maximum relative error of 7.7% was recorded, and gross-IMEP, for which a maximum error of 2.8% was recorded.

| Results   | NOx <sub>[g/kWh]</sub> | Soot <sub>[g/kWh]</sub> | IMEP <sub>[bar]</sub> |
|-----------|------------------------|-------------------------|-----------------------|
| Virtual   | 1.9                    | 0.11                    | 18.5                  |
| Simulated | 1.7 (-10.5%)           | 0.11 (-0.0%)            | 18.9 (+2.2%)          |

Table 7.4. G012 trade-off individual validation

| Results   | NOx <sub>[g/kWh]</sub> | Soot <sub>[g/kWh]</sub> | IMEP <sub>[bar]</sub> |
|-----------|------------------------|-------------------------|-----------------------|
| Virtual   | 2.0                    | 0.13                    | 17.7                  |
| Simulated | 1.8 (-10.0%)           | 0.12 (-7.7%)            | 18.2 (+2.8%)          |

Table 7.5. VHP011 trade-off individual validation

| Results   | NOx <sub>[g/kWh]</sub> | Soot <sub>[g/kWh]</sub> | IMEP <sub>[bar]</sub> |
|-----------|------------------------|-------------------------|-----------------------|
| Virtual   | 2.0                    | 0.07                    | 18.6                  |
| Simulated | 1.8 (-10.0%)           | 0.07 (-0.0%)            | 18.9 (+1.6%)          |

Table 7.6. NE trade-off individual validation

## Chapter 8

# Combustion analysis of the optimal solutions

The genetic algorithm NSGA-II, coupled to with radial basis functions neural networks, allowed to define the best individuals of the piston bowls G012, VHP011 and NE with a small number of CFD calculations performing a multi-objective virtual optimization. Seven thousands and two hundreds individuals, for each piston bowl, were investigated during the evolutionary process allowing the definition of the Pareto frontier of the piston bowl G012, VHP011 and NE. Amongst Pareto optimal solutions, three individuals, one for each piston bowl, were chosen as the NO<sub>x</sub>-soot trade-off. Then, the best individuals were validated by actual CFD calculations so that, at the final stage of the work, it was possible to compare the obtained results and investigate deeply the combustion development and the emissions of these solutions with the typical post-processing instruments of a CFD analysis.

## 8.1 Emissions and performance

In tables 8.1 are reported the values of NO<sub>x</sub>, soot and gross-IMEP of the NO<sub>x</sub>-soot trade-off individuals of each investigated piston bowl along with their input parameters.

As it can be seen, the combustion chamber NE can meet the NO<sub>x</sub> emission limit with a lower exhaust gas recirculation (10.0%) than the one needed by the other two piston bowls (13.0% for the piston bowl G012, 12.0% for the piston bowl VHP011) and a higher swirl ratio (1.6), allowing a significant decrease of soot emission (-36%) while maintaining a good performance and approximately the same NO<sub>x</sub> emission.

| Bowls  | $P_{boost}$ | SR  | EGR [%] | SOI [deg. ATDC] | NO <sub>x</sub> [g/kWh] | Soot [g/kWh] | IMEP [bar] |
|--------|-------------|-----|---------|-----------------|-------------------------|--------------|------------|
| G012   | 3.39        | 1.5 | 13.0    | -6.6            | 1.7                     | 0.11         | 18.9       |
| VHP011 | 3.33        | 1.3 | 12.0    | -6.0            | 1.8 (+5%)               | 0.12 (+9%)   | 18.2 (-4%) |
| NE     | 3.39        | 1.6 | 10.0    | -6.0            | 1.8 (+5%)               | 0.07 (-36%)  | 18.9 (-0%) |

Table 8.1. Comparison between the real trade-off individuals

## 8.2 Combustion development

Figure 8.1 shows the in-cylinder pressure evolution between intake valve closure and exhaust valve opening.

Figure 8.2 shows the net rate of heat release calculated from the pressure curve. Figures from 8.3 through 8.9 show an isosurface having equivalence ratio equals to one, coloured by temperature, for different crank angle.

All the three investigated piston bowls show a similar combustion development from the start of injection till approximately top dead center (see figures 8.1 and 8.2). During this time, the fuel spray inside the piston bowl G012, VHP011, NE is covering the free path between the point of injection and the piston bowl lip as shown in figures 8.3 and 8.4. As the fuel plume reaches the piston bowl lip, it begin to interact with the chamber walls (figure 8.5) and the combustion development inside the investigated piston bowls begin to differ due to different spray/walls interactions (figures from 8.5 through 8.9) originated by different piston shapes. Between 0 Ca deg. ATDC and 20 CA deg. ATDC, as a result of a better interaction, the combustion development inside the piston bowl G012 is enhanced resulting in higher net rate of heat release (figure 8.2) and in a higher in-cylinder pressure (figure 8.1). It worth notice that the SOI of the chamber G012 is slightly advanced (see table 8.1) easing the propagation of the combustion inside the piston bowl. However, starting from about 20 CA deg. ATDC, the piston bowl NE shows (figures 8.8, 8.9) a better diffusion of the fuel spray inside the squish volume, due to the swirl

motion, resulting in a better combustion as proved by the higher net rate of heat release during the tail of combustion (figure 8.2). As a result, starting from about 30 CA deg. ATDC the combustion chamber NE records a higher in-cylinder pressure.

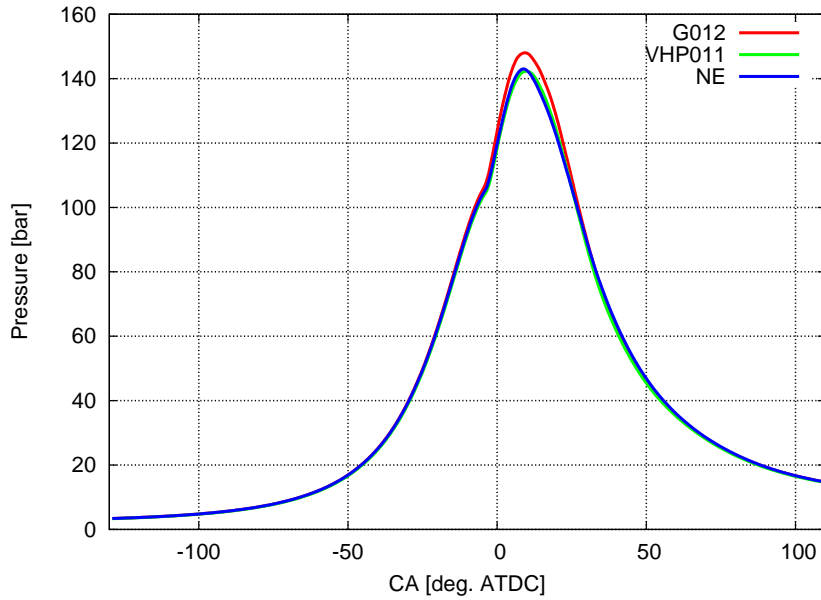


Figure 8.1. In-cylinder pressure

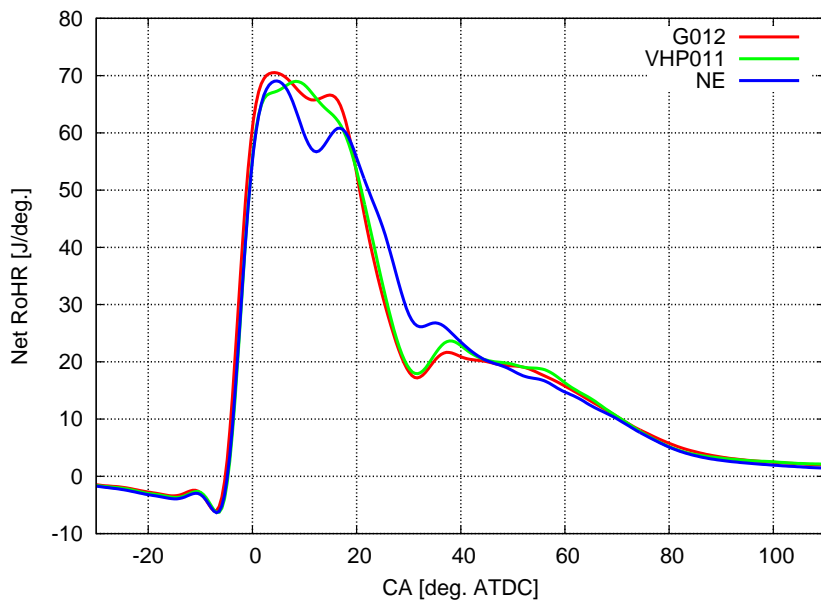


Figure 8.2. Net rate of heat release

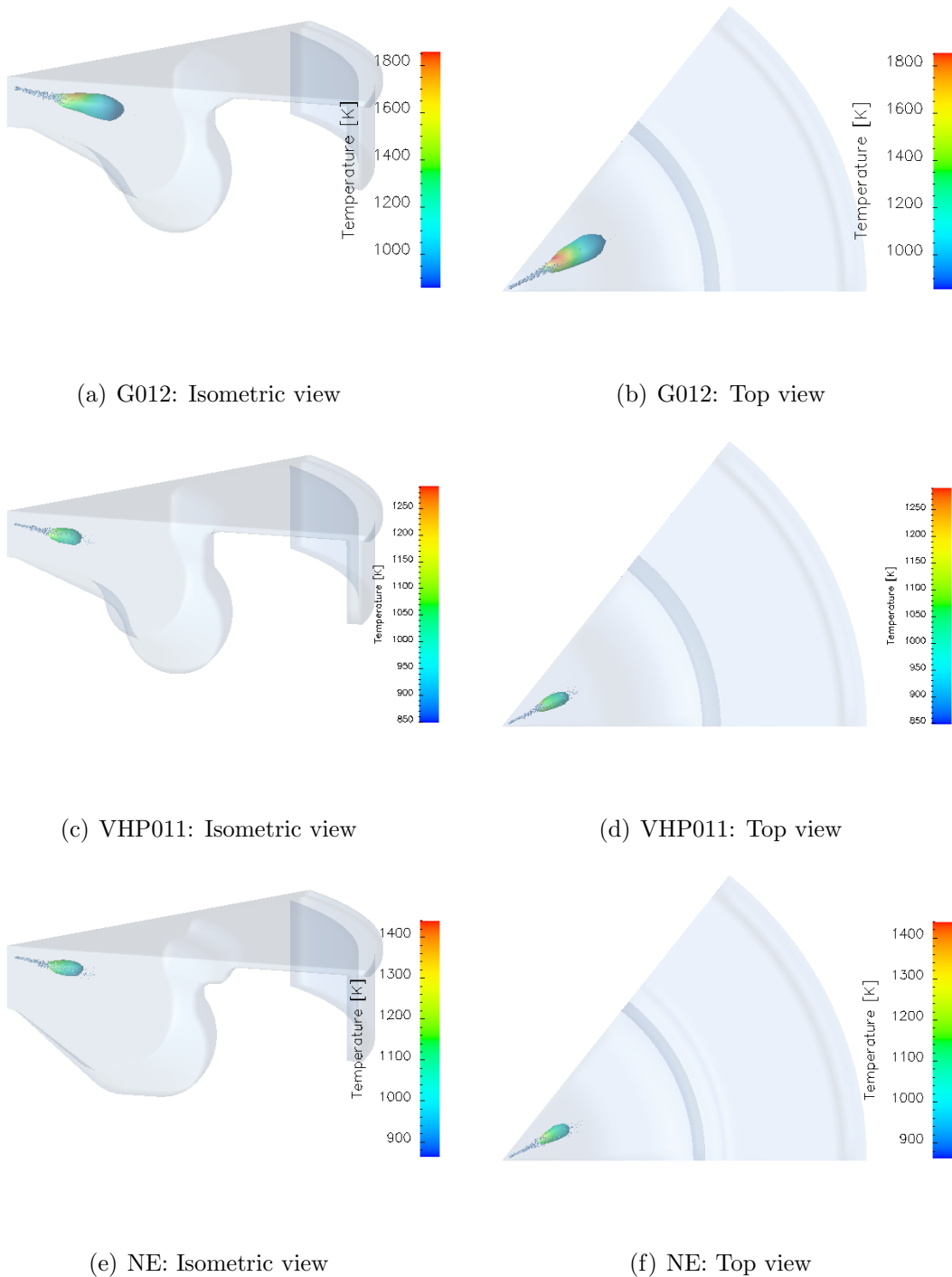


Figure 8.3. Isosurface of  $\phi = 1$  coloured by temperature at -4.0 CA deg. ATDC

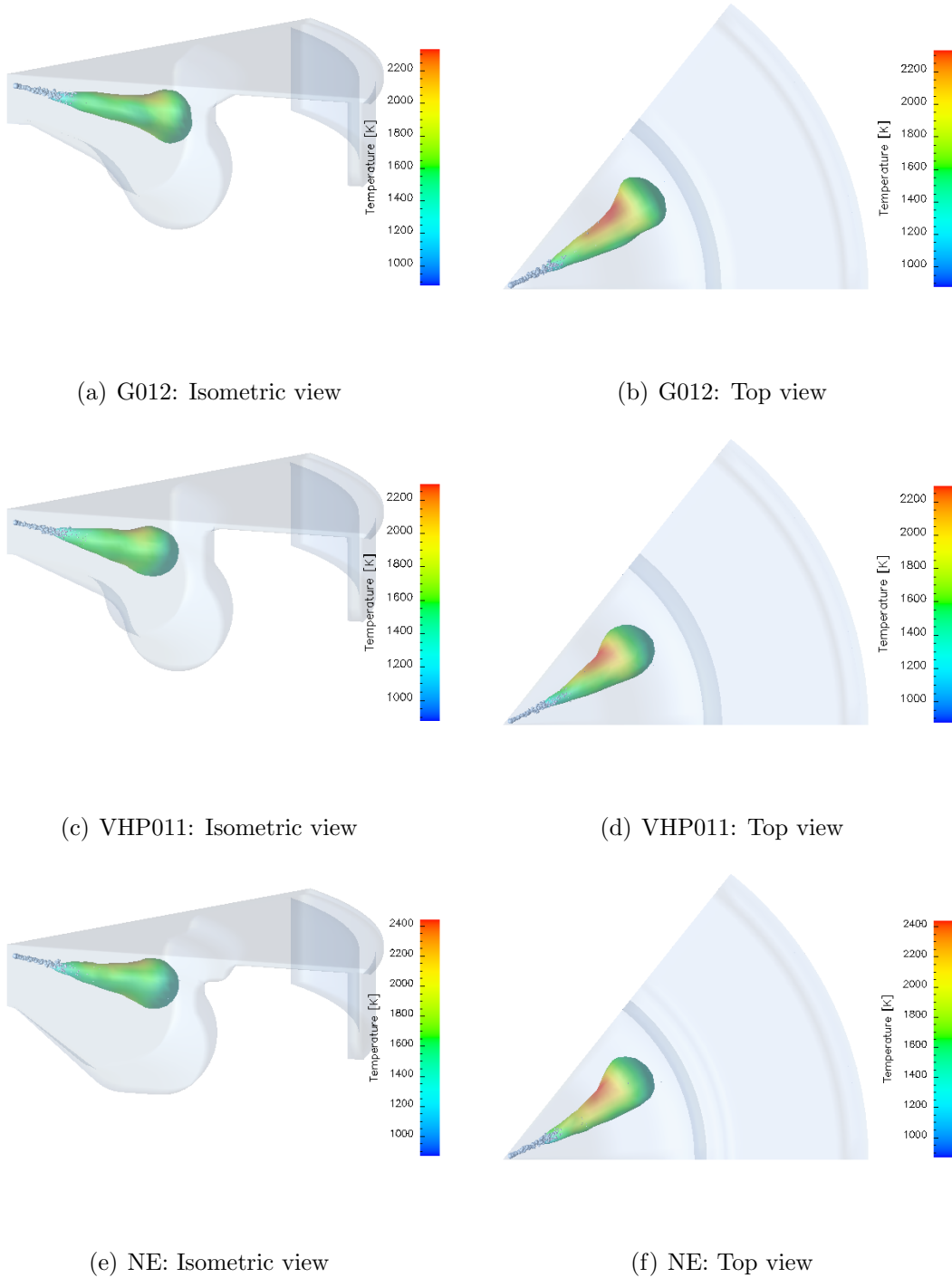


Figure 8.4. Isosurface of  $\phi = 1$  coloured by temperature at -1.5 CA deg. ATDC

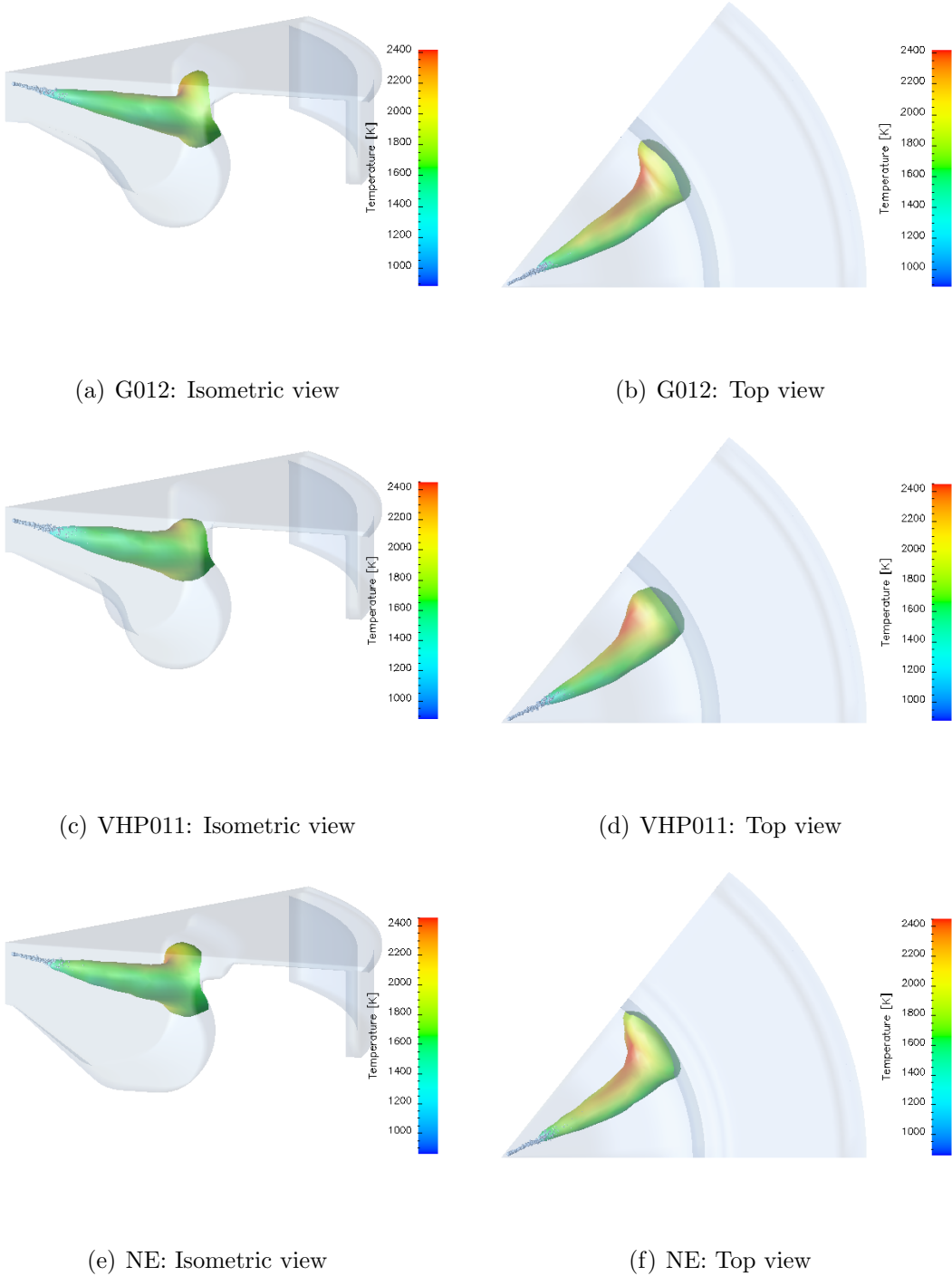
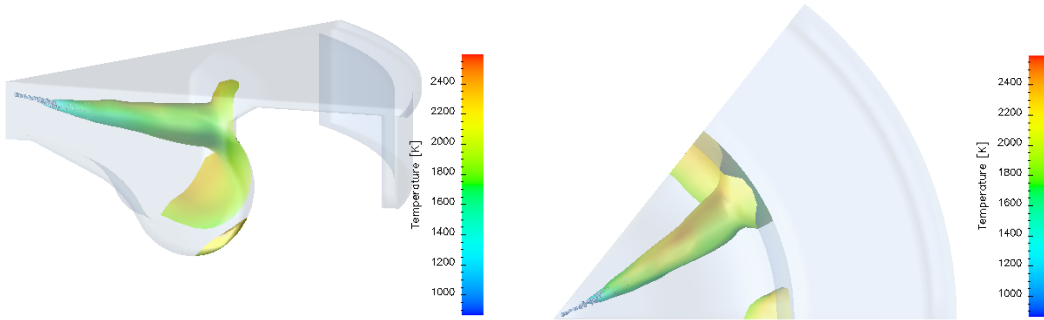
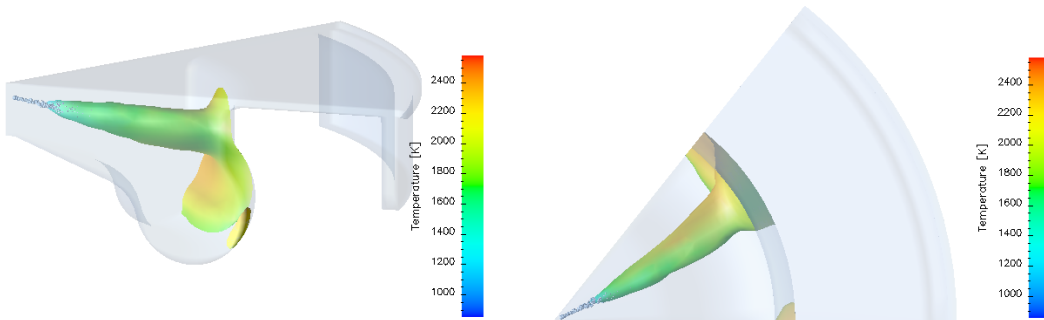


Figure 8.5. Isosurface of  $\phi = 1$  coloured by temperature at 1.0 CA deg. ATDC



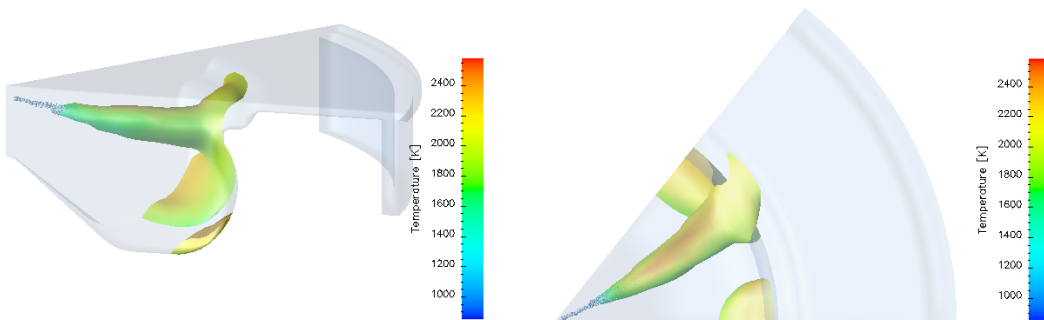
(a) G012: Isometric view

(b) G012: Top view



(c) VHP011: Isometric view

(d) VHP011: Top view



(e) NE: Isometric view

(f) NE: Top view

Figure 8.6. Isosurface of  $\phi = 1$  coloured by temperature at 6.0 CA deg. ATDC

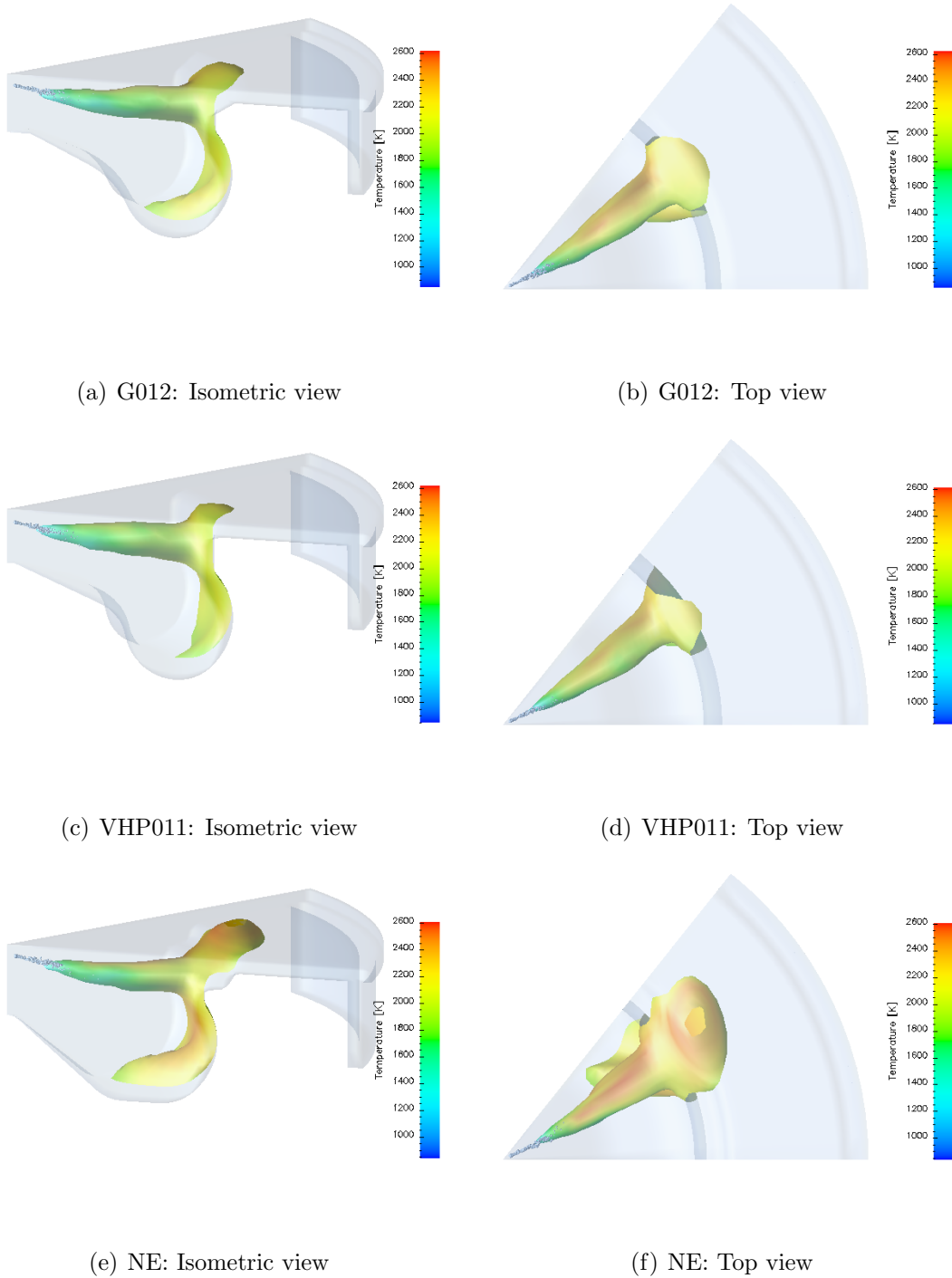


Figure 8.7. Isosurface of  $\phi = 1$  coloured by temperature at 11.0 CA deg. ATDC

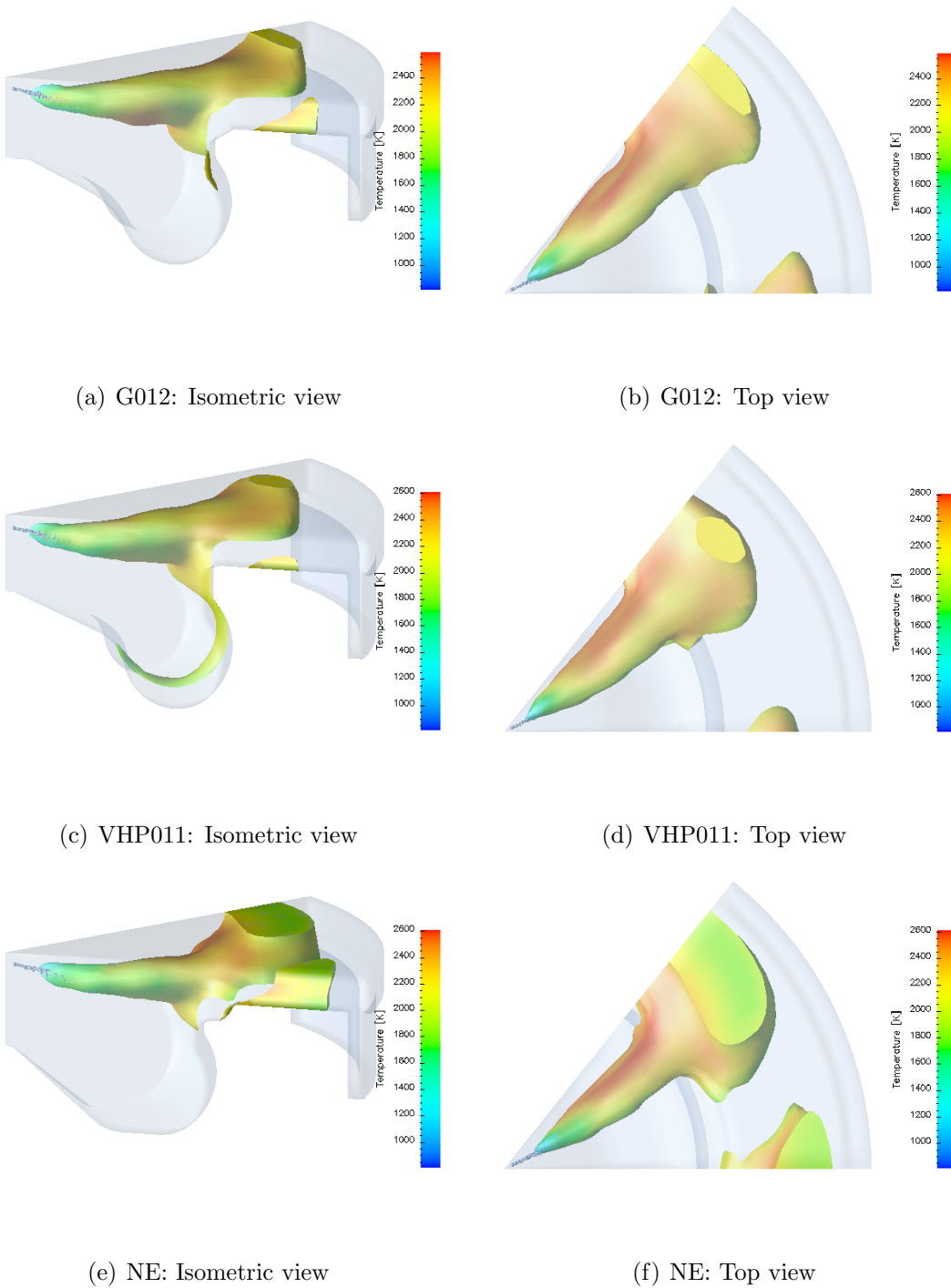


Figure 8.8. Isosurface of  $\phi = 1$  coloured by temperature at 21.0 CA deg. ATDC

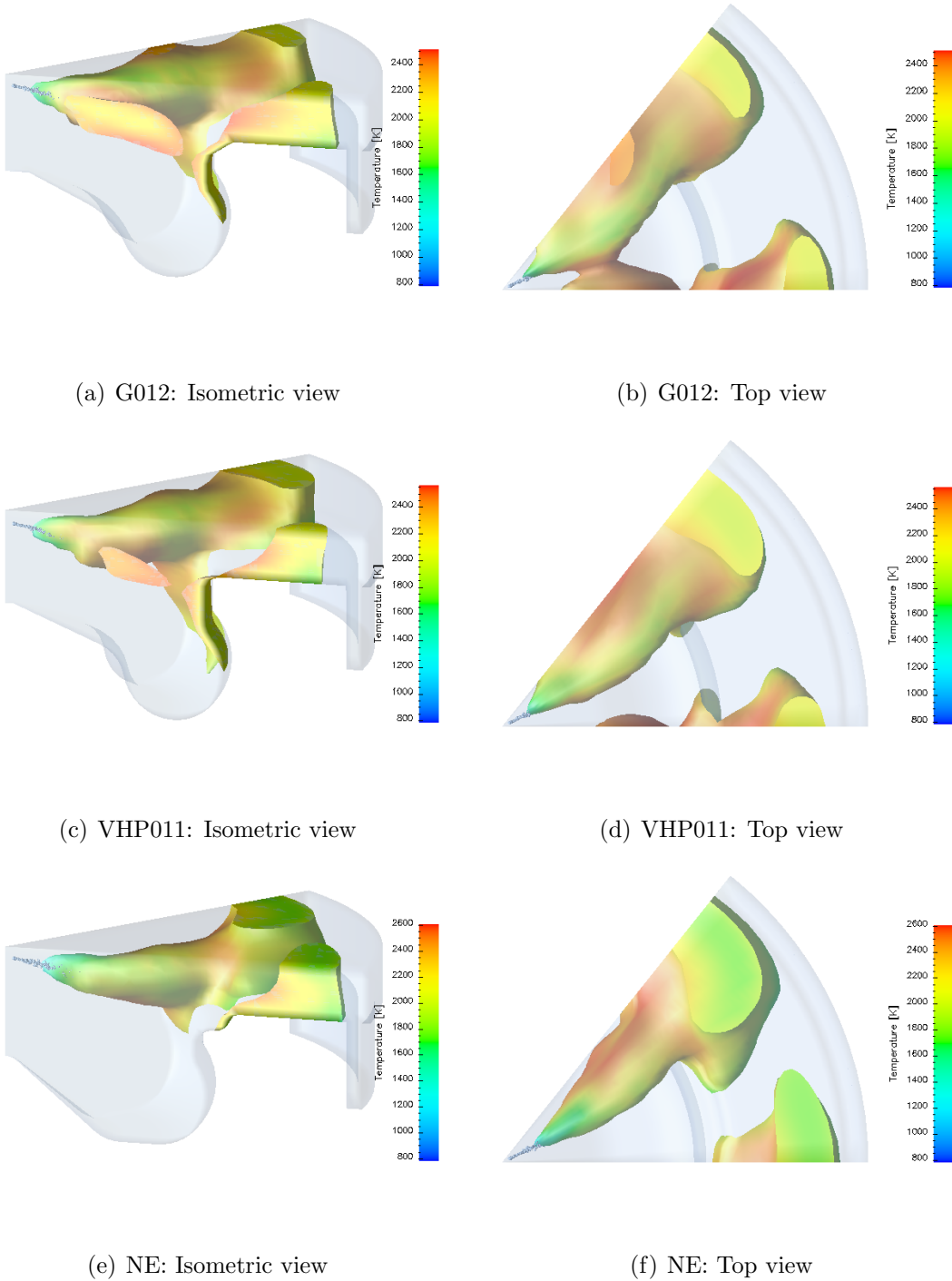


Figure 8.9. Isosurface of  $\phi = 1$  coloured by temperature at 26.0 CA deg. ATDC

### 8.3 NOx emission

Figure 8.10 shows the evolution of NOx emission in ppm.

Figure 8.11 shows the mean chamber temperature.

Figure 8.12 shows the percentage of the computational domain having a temperature above 2200 K.

Figures from 8.13 through 8.15 show an isosurface of  $T = 2200$  K coloured by oxygen mass fraction.

As a result of a better combustion between 0 CA deg. ATDC and 20 CA deg. ATDC (see 8.2), the piston bowl G012 records a higher mean chamber temperature (figure 8.11) and a higher percentage of the fluid domain having a temperature above 2200 K (figure 8.12). Then, starting from about 25 CA deg. ATDC, the piston bowl NE recorded a better combustion efficiency (see 8.2) and, thus, as could be seen in figures 8.11 and 8.12, show a higher mean chamber temperature and a higher percentage of hot spots during the tail of combustion. Particularly, during this interval, the piston bowl NE shows a higher percentage of hot spots inside the bowl volume due to a different combustion development (figure 8.15). In fact, while Piston bowls G012 and VHP011 present a more pronounced central tip which inhibits the combustion development inside the piston bowl, the central tip of the piston bowl NE allows the propagation of the combustion towards the center of the bowl (figure 8.15).

Overall, the piston bowl NE records a higher NOx concentration in ppm (figure 8.10).

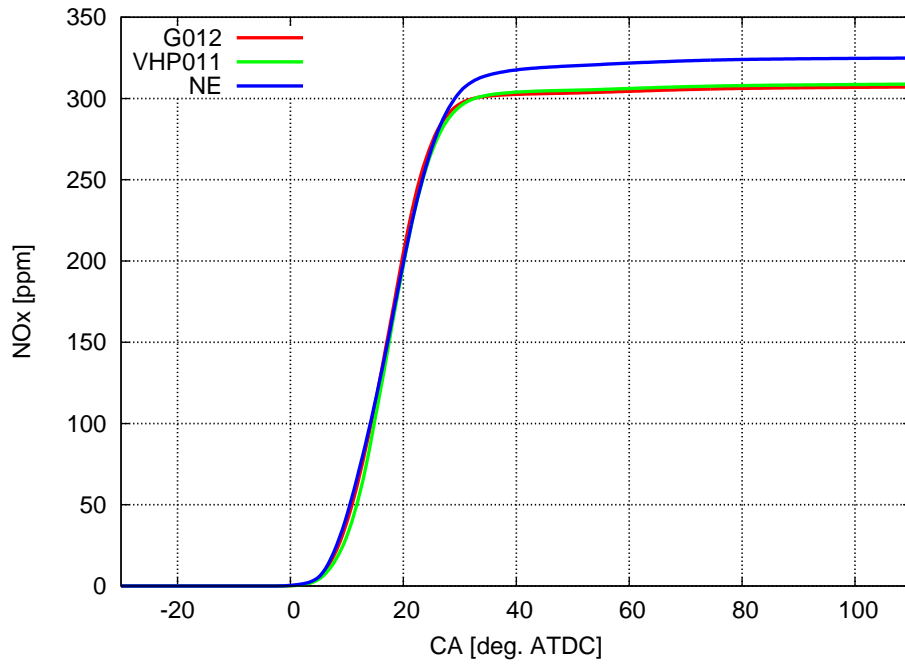


Figure 8.10. NOx emission

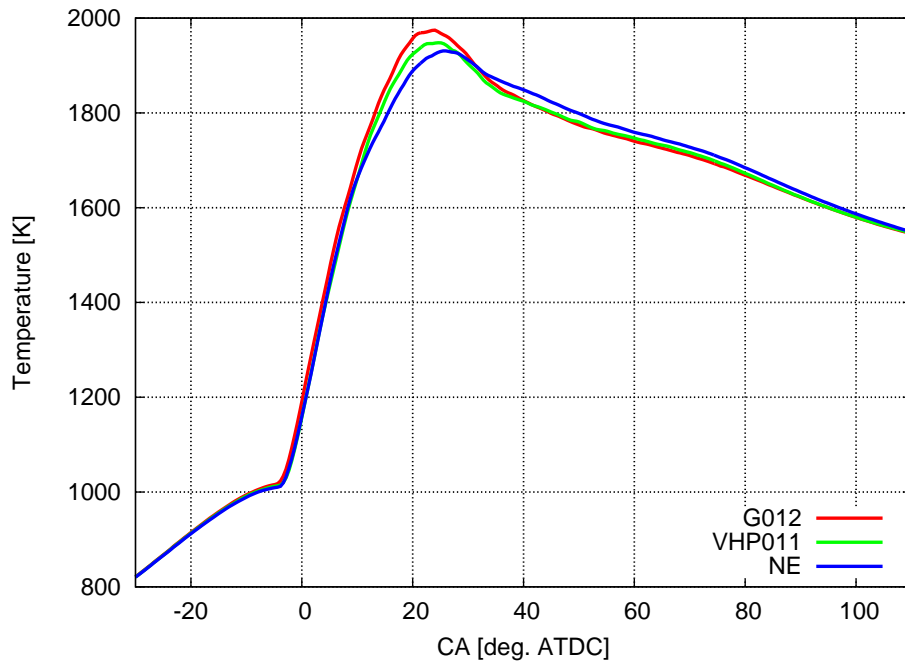


Figure 8.11. Mean chamber temperature

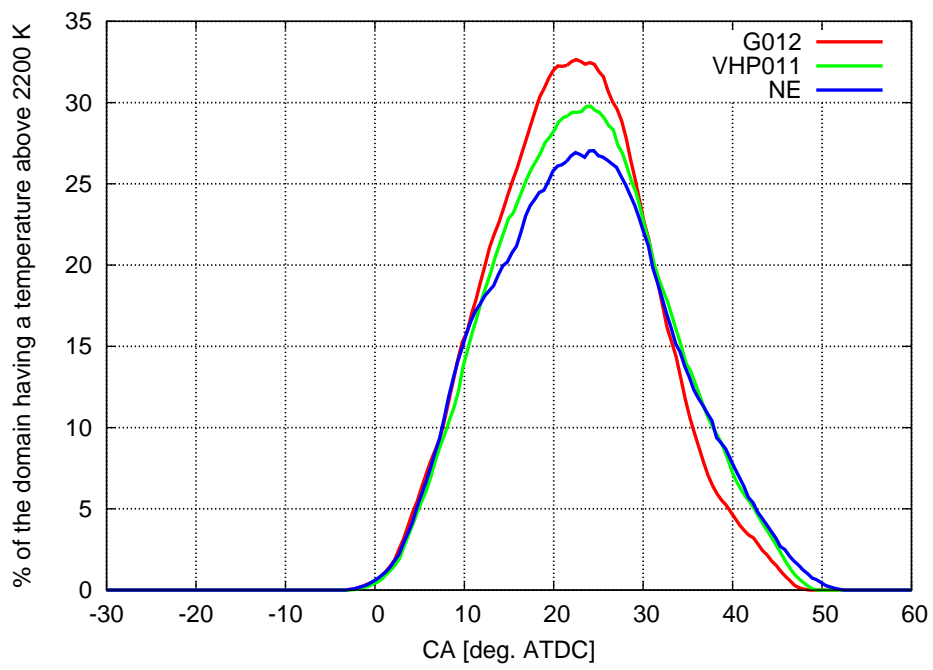


Figure 8.12. Hot spots

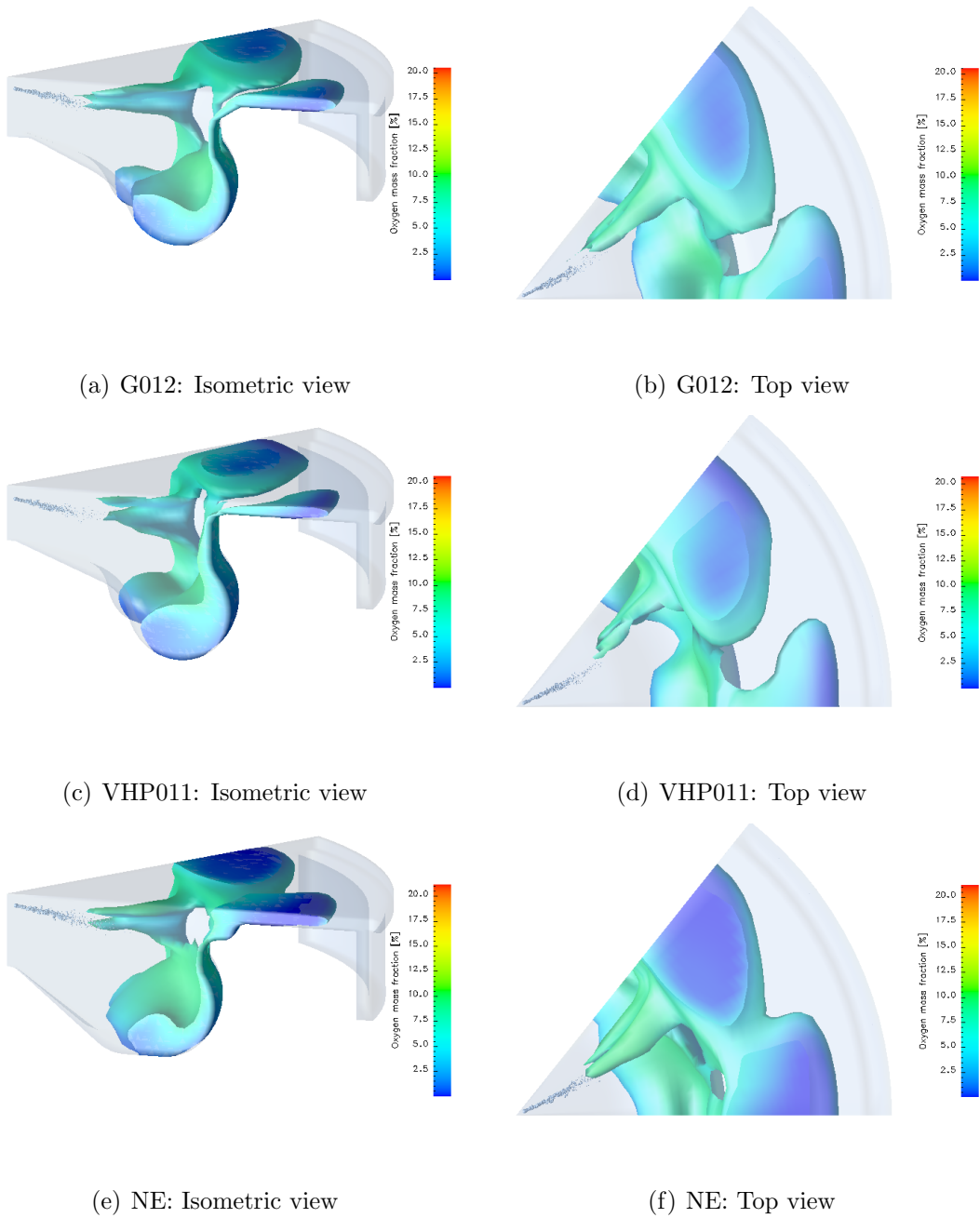


Figure 8.13. Isosurface of  $T = 2200K$  coloured by oxygen mass fraction at 11.0 CA deg. ATDC

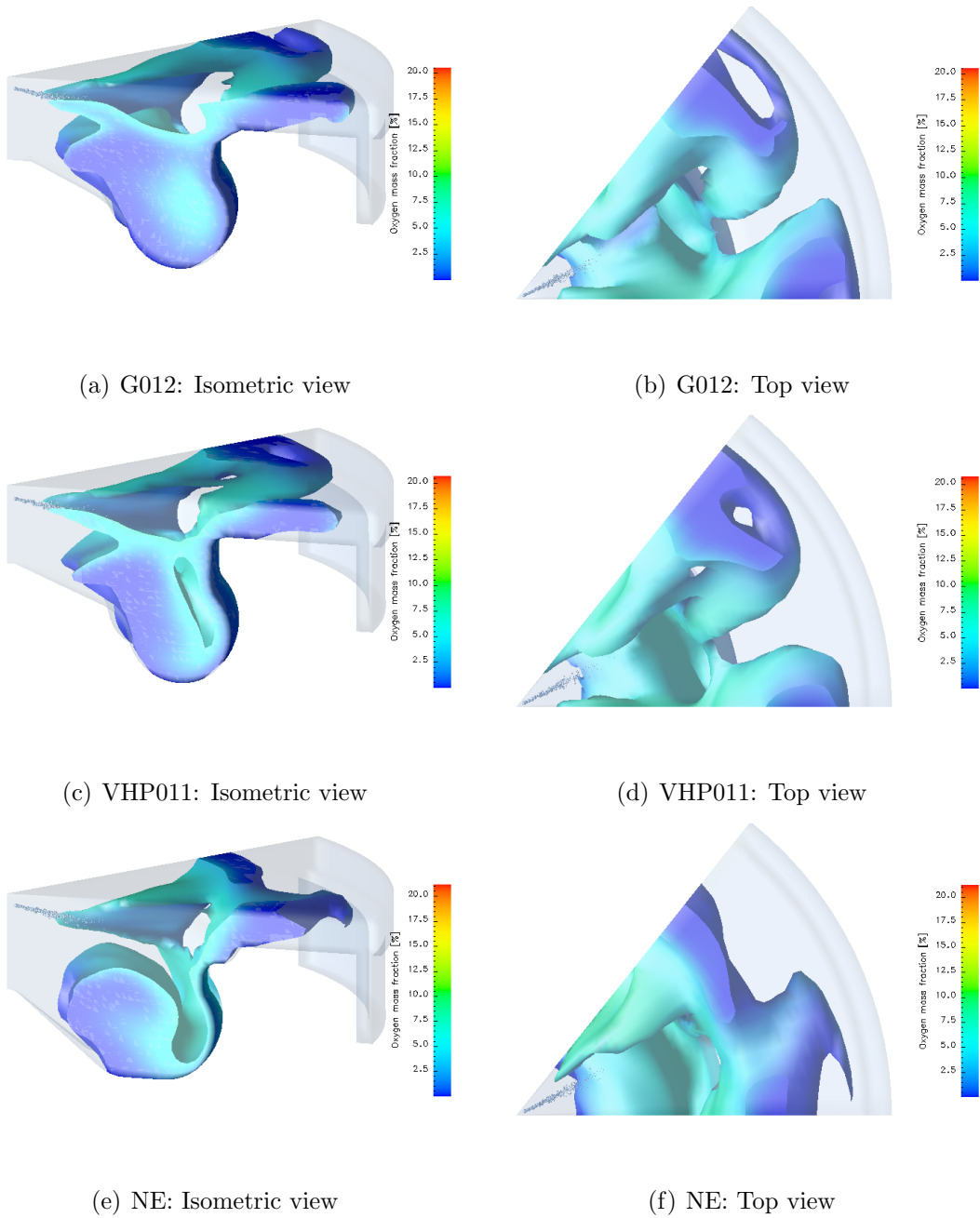


Figure 8.14. Isosurface of  $T = 2200K$  coloured by oxygen mass fraction at 21.0 CA deg. ATDC

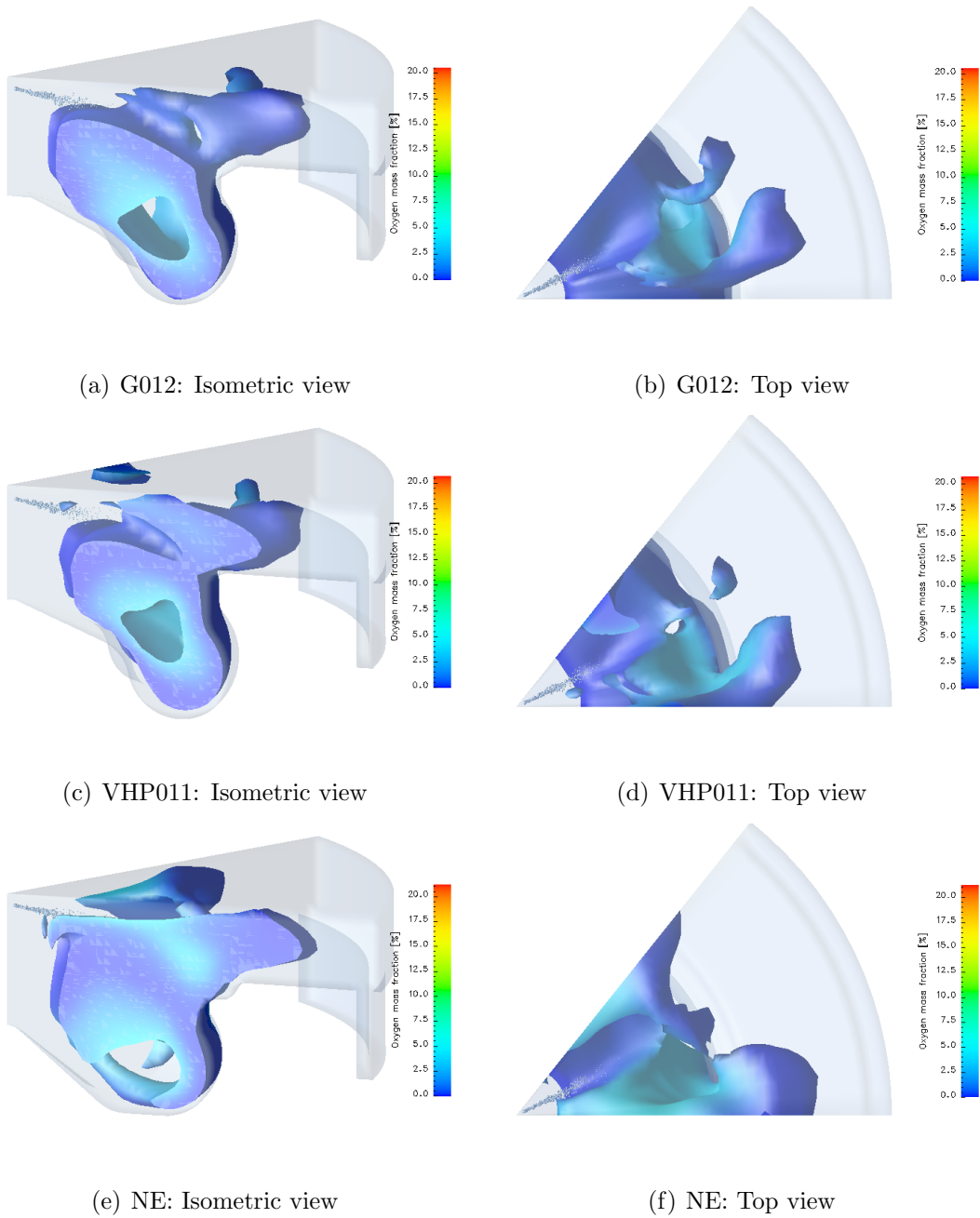


Figure 8.15. Isosurface of  $T = 2200K$  coloured by oxygen mass fraction at 31.0 CA deg. ATDC

## 8.4 Soot emission

Figure 8.16 shows the evolution of soot emission during the combustion development. Figure 8.17 shows of the computational domain having an equivalence ratio above 2.

Figure 8.18 shows the in-cylinder oxygen mass fraction evolution.

Figures from 8.19 through 8.19 show an isosurface of equivalence ratio equals to 3 at different crank angles.

Between the start of injection and 20 CA deg. ATDC, all the three investigated piston bowls shows approximately the same fuel/air mixing, as could be seen in figure 8.17, and the same soot concentration (figure 8.16). However, during the tail of combustion, the piston bowl NE records a lower percentage of fuel rich zones which results in a lower maximum soot concentration. During this interval, the shape of the bowl lip of the piston NE allows (figures 8.19, 8.20, 8.21) a better conservation of the fuel spray momentum which helps in decreasing the fuel rich zones near the point of injection and inside the piston bowl. The ability to meet the NOx euro 5 emission limit with a lower exhaust recirculation of the piston bowl NE (see table 8.1) also plays a role allowing to work with higher overall  $\lambda$  and increasing the disposable oxygen for the fuel/air mixing.

Moreover, piston bowls G012 and VHP011 show a certain overlap between neighbouring fuel plumes which limits the swirl ratio inside these piston bowls (figure 8.21). Infact, it was seen in table 8.1 that the piston bowl NE was optimized by a swirl ratio of 1.6 while the piston bowls G012 and VHP011 required a swirl ratio of 1.5 and 1.3 respectively. After the combustion end, all the three investigated piston bowls show no significant differences in soot oxydation, as testified by the trend of oxygen consumption between 40 CA deg. ATDC and exhaust valve opening (figures 8.18, 8.19, 8.20, 8.21). Overall, the piston bowl NE records a lower soot emission, at exhaust valve opening, due mainly to a better fuel/air mixing.

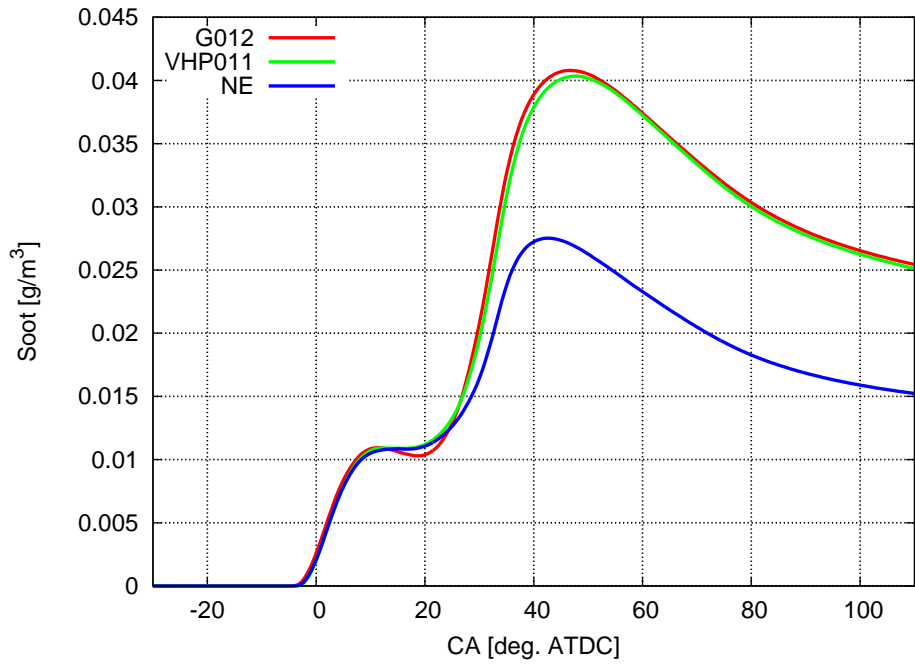


Figure 8.16. Soot emission

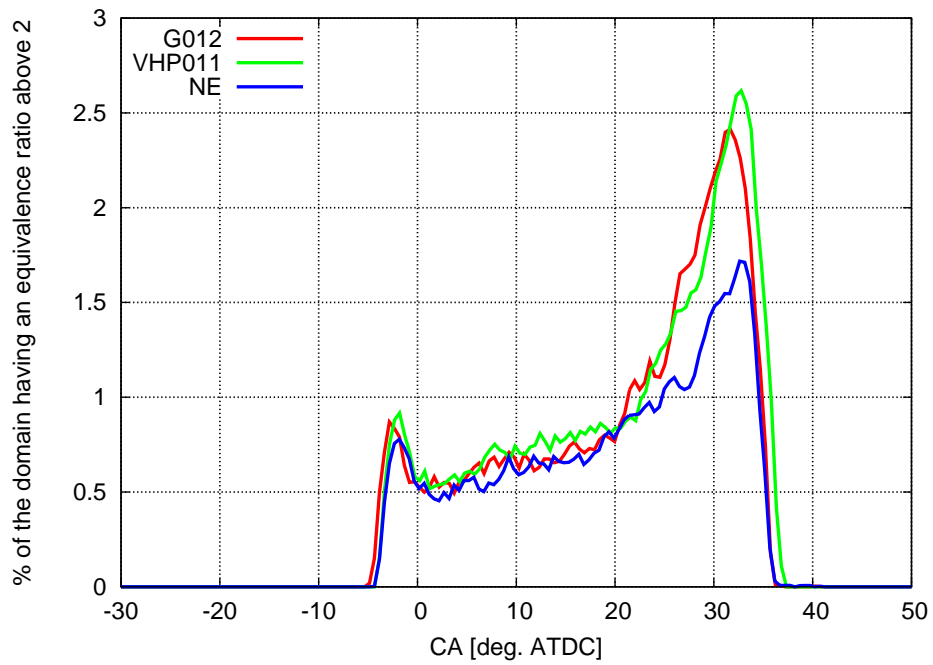


Figure 8.17. Percentage of fuel rich zones

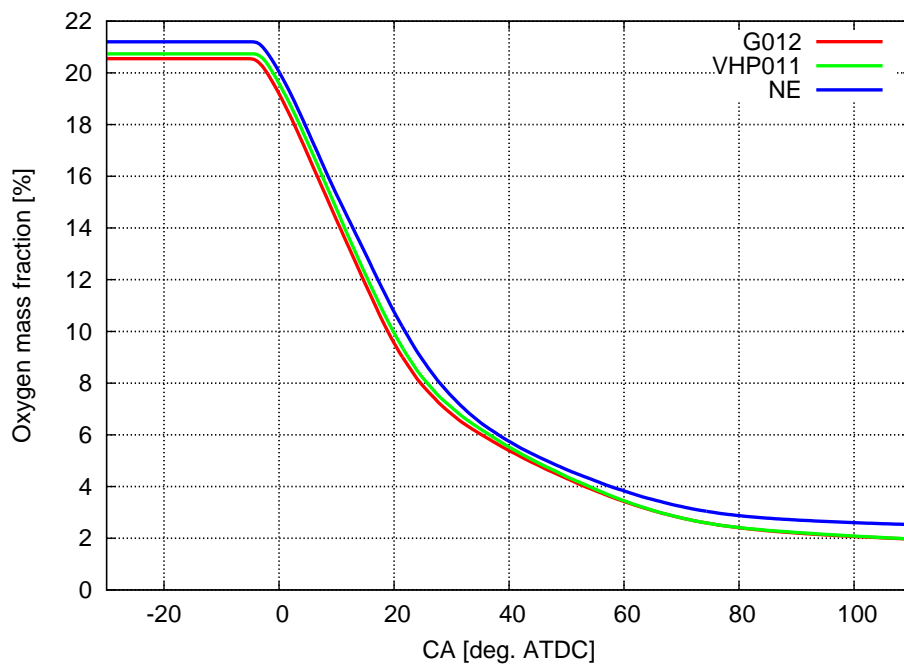


Figure 8.18. In-cylinder oxygen mass fraction

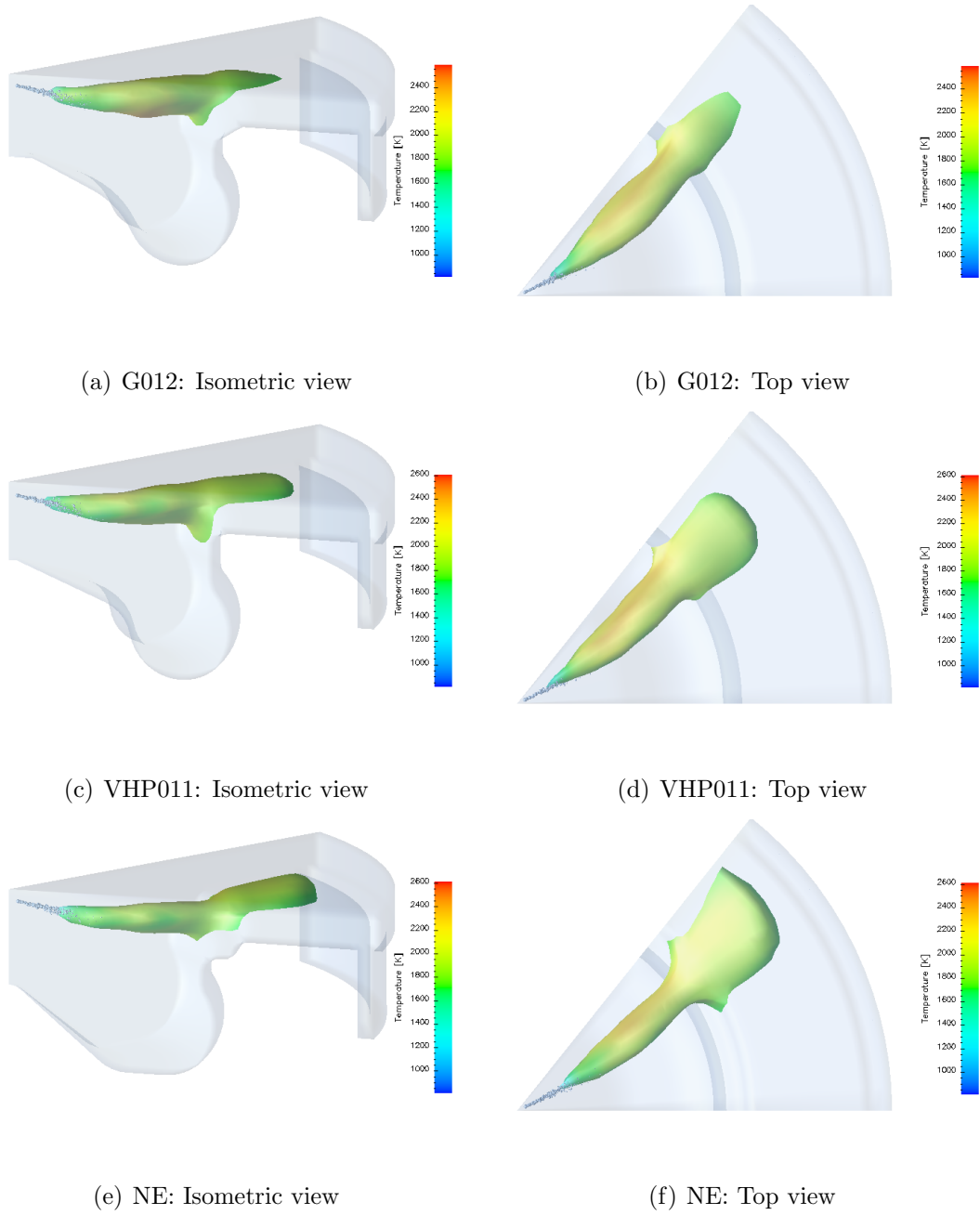


Figure 8.19. Isosurface of  $\phi = 3$  coloured by temperature at 21.0 CA deg. ATDC

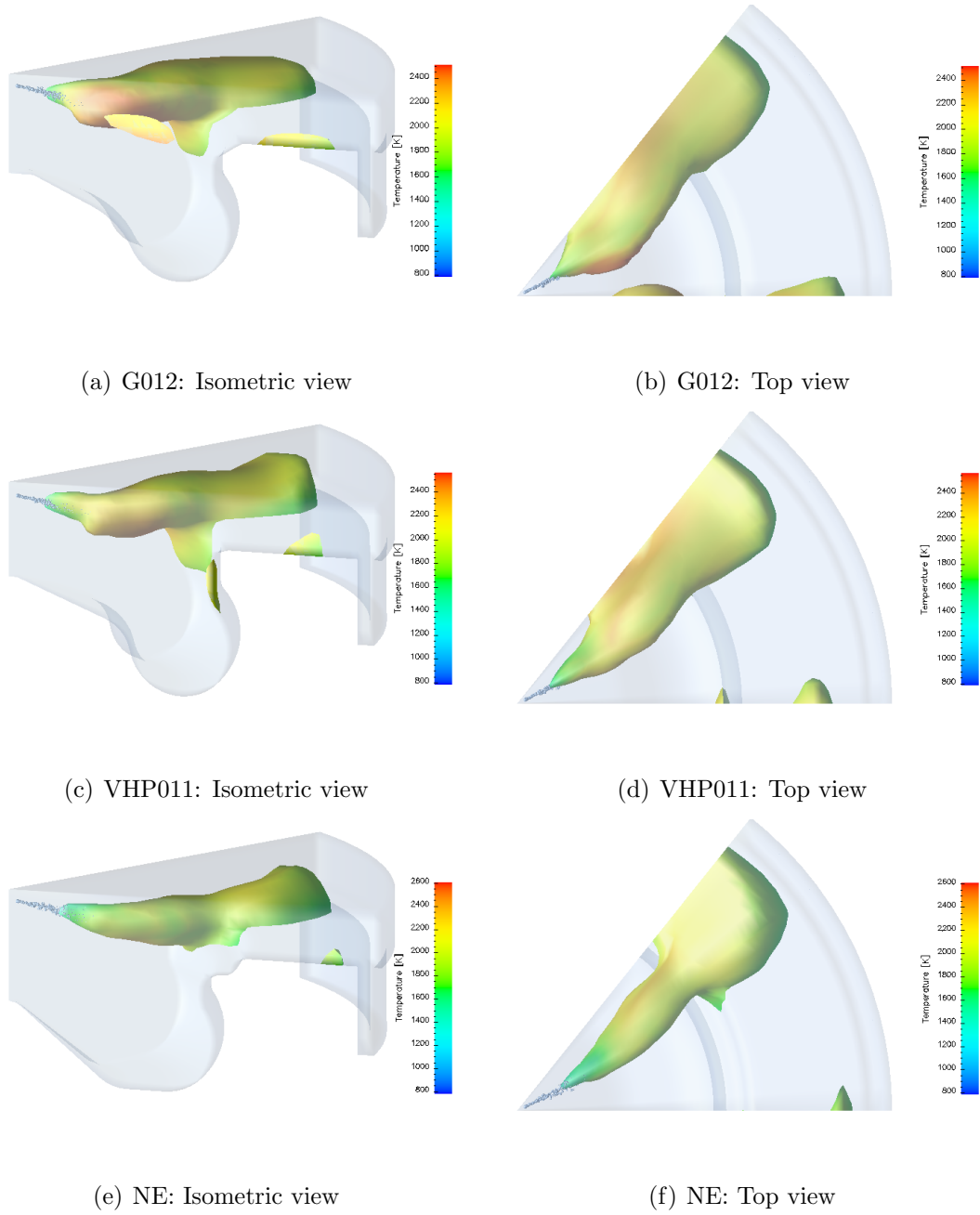


Figure 8.20. Isosurface of  $\phi = 3$  coloured by temperature at 26.0 CA deg. ATDC

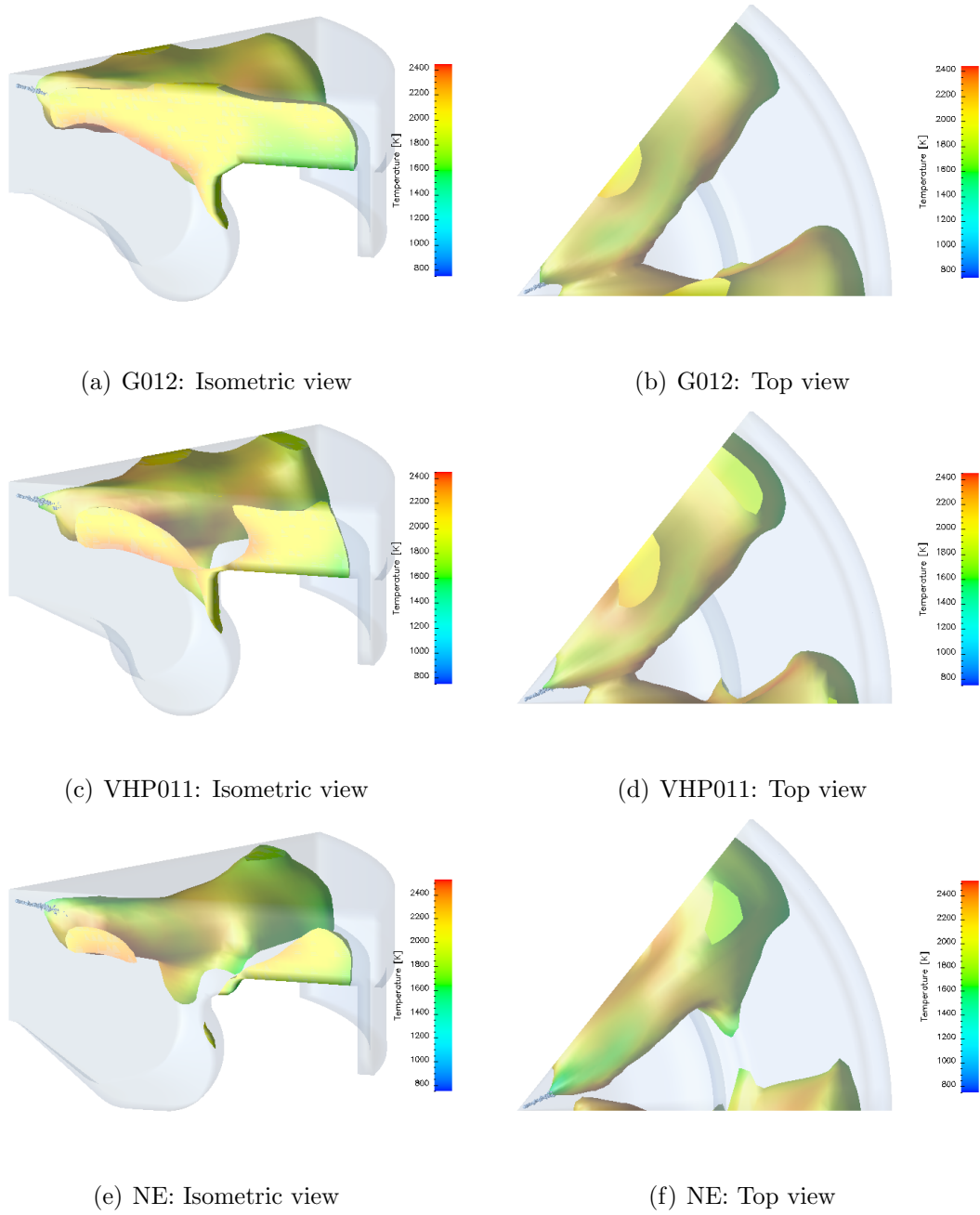


Figure 8.21. Isosurface of  $\phi = 3$  coloured by temperature at 31.0 CA deg. ATDC

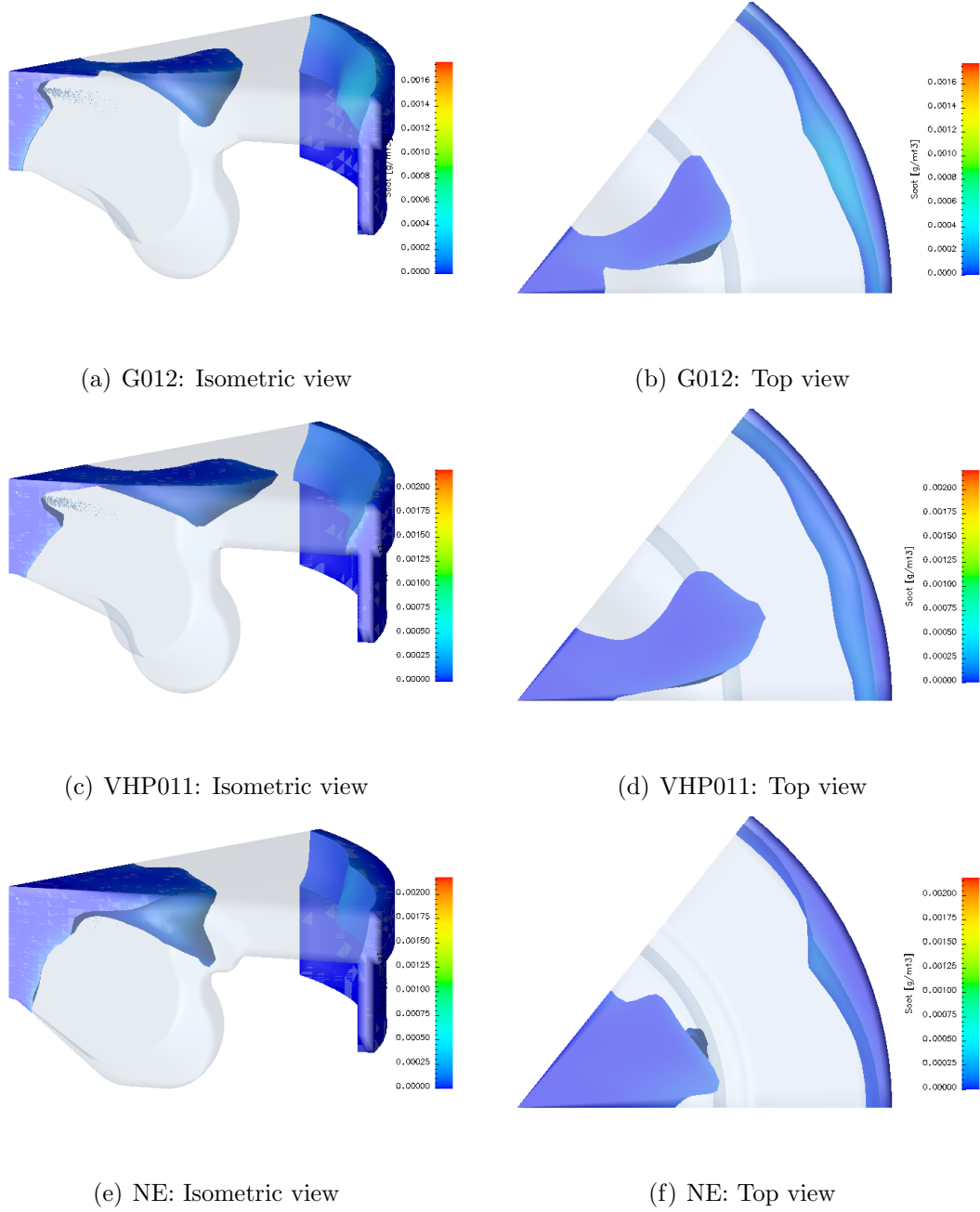


Figure 8.22. Isosurface of  $\phi = 3$  coloured by temperature at 36.0 CA deg. ATDC

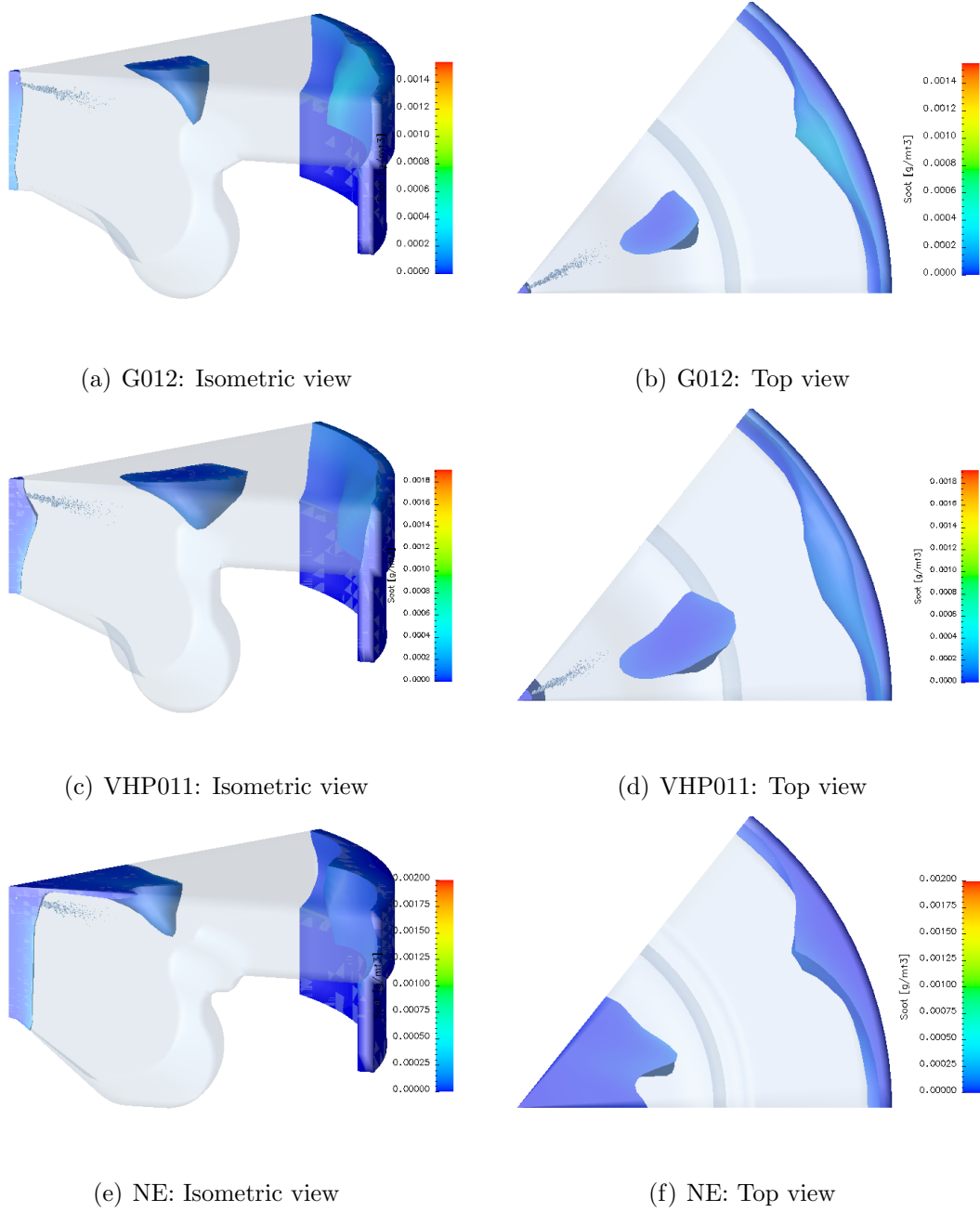


Figure 8.23. Isosurface of  $\phi = 3$  coloured by temperature at 41.0 CA deg. ATDC

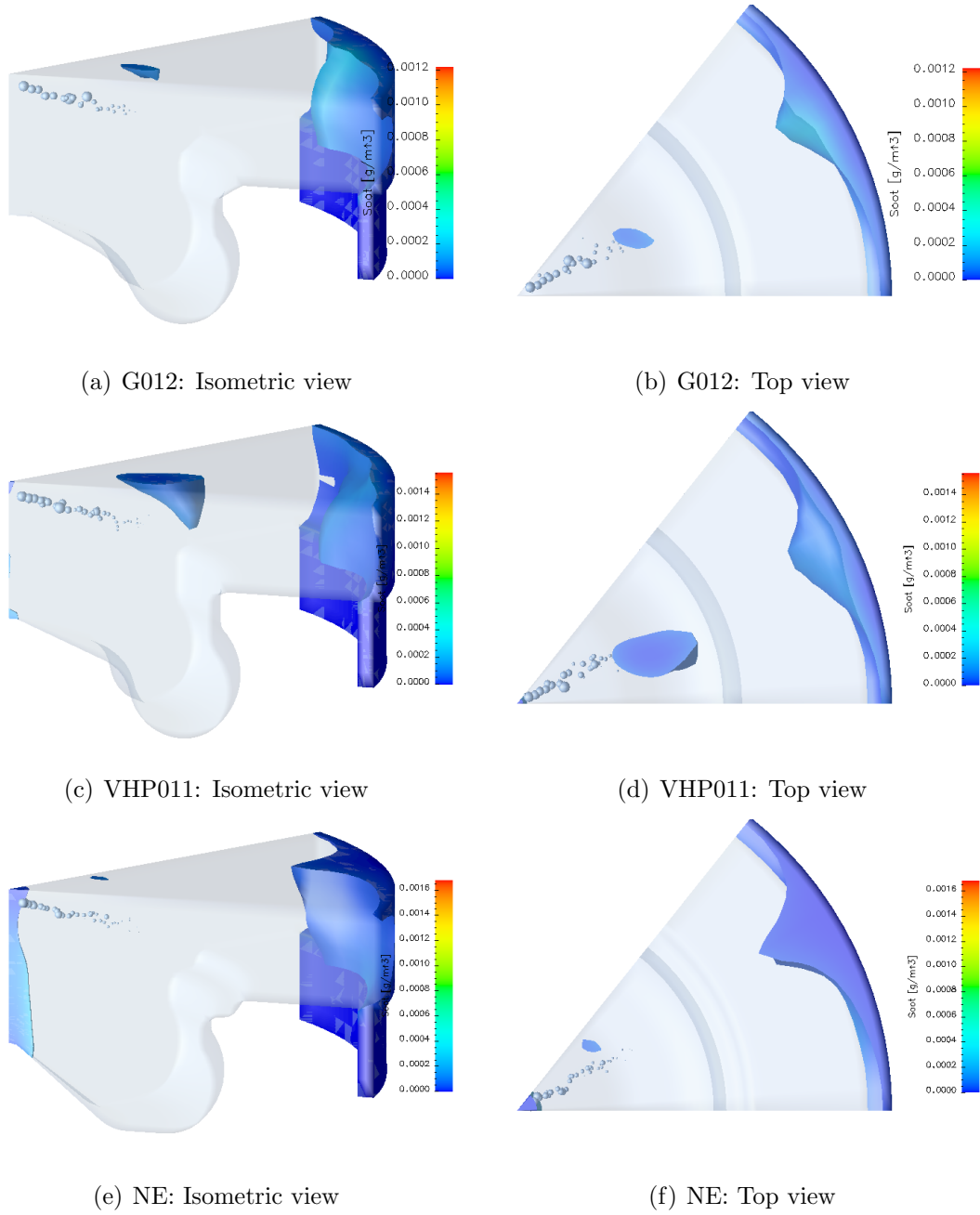


Figure 8.24. Isosurface of  $\phi = 3$  coloured by temperature at 46.0 CA deg. ATDC

# Chapter 9

## Conclusion

In order to achieve a significant combustion improvement it is mandatory, for the future DI Diesel engine, to develop a robust design methodology focused on decreasing NO<sub>x</sub> and soot emissions simultaneously while maintaining a reasonable fuel economy. However, since there are trade-off relationships between engine performance, NO<sub>x</sub> and soot emissions, numerically executed parametric searches can not find a unique solution which optimizes all the objectives of a good design at the same time.

For this kind of problem, multi-objective genetic algorithms have been successfully used, over the last few years, due to their ability to find multiple Pareto-optimal solutions in one single run as they mimic the evolutionary processes of ecosystems, which obey the Darwinian idea of *survival of the fittest*, moving the Pareto front towards the ideal optimal set of solutions as the optimization process evolves.

Nonetheless, combining GAs optimization with actual CFD three-dimensional combustion simulations can be too onerous since a large number of calculations is usually needed for the genetic algorithm to converge, resulting in a high computational cost and, thus, limiting the suitability of this method for industrial processes.

In the current work, a numerical methodology for the multi-objective virtual optimization of the combustion of an automotive DI Diesel engine, which relies on artificial neural networks and genetic algorithms, was developed.

At the base of the methodology, three-dimensional CFD calculations were used to generate valid training sets for the learning process of artificial neural networks. Artificial neural networks were chosen amongst other statistical modeling tools due to their ability to model complex relationships between inputs and outputs like those which tie up design parameters and objectives inside the DI Diesel engine. Then, once properly trained, the artificial neural networks were used during the evaluation phase of the genetic algorithm to foresee NO<sub>x</sub>, soot and gross-IMEP as a function of the input parameters. The NSGA-II genetic algorithm was used due to its ability to find Pareto optimal solutions in one single run with a low computational

cost. All the needed software for the RBF neural learning process and the multi-objective virtual optimization was written in Matlab/Octave language starting from the algorithm described in chapters 4 and 5.

The proposed methodology was used to aid the development process of a 4-cylinders/4-valve for cylinder engine with a total displacement of 2.4 liters targeted for automotive applications allowing to evaluate three different piston bowls under a wide range of operating conditions and to find out, for each piston bowl, the Pareto-optimal individuals with a small number of calculations. At the final stage of the work, the best solutions were validated through actual CFD three-dimensional calculations and their own combustion developments were deeply investigated by means of the typical CFD post-processing instruments.

The developed numerical methodology proved to be both fast and accurate and is currently successfully employed to aid the design of several DI Diesel engine.

# Bibliography

- [1] J. Abraham, F. V. Bracco, e R. D. Reitz. Comparisons of computed and measured premixed charge engine combustion. *Combustion and Flame*, 60:309–322, June 1985.
- [2] A. A. Amsden, P. J. O'Rourke, e T. D. Butler. KIVA-3: A KIVA program with block-structured mesh for complex geometries. Relazione Tecnica LA-12503-MS, Los Alamos National Labs, 1993.
- [3] G. M. Bianchi, G. Cazzoli, C. Forte, Costa. M, e M. Oliva. High efficiency two-valve di diesel engine for off-road application complying with upcoming emission limits. In *Proceedings of the ASME 2012 International Combustion Engine Division Spring Technical Conference*, pp. 577–584, Torino (Italy), 2012.
- [4] G. M. Bianchi, S. Falfari, M. Parotto, e G. Osbat. Advanced modeling of common rail injector dynamics and comparison with experiments. *SAE Paper 2003-01-0006*, 2003.
- [5] G. M. Bianchi e P. Pelloni. A cavitation-induced atomization model for high-pressure diesel spray simulations. In *32nd International ISATA Conference, Technical Paper 99SI044*, Wien, jun 1999.
- [6] G. M. Bianchi e P. Pelloni. Modeling the diesel spray breakup by using a hybrid model. *SAE Paper 1999-01-0226*, 1999.
- [7] G. M. Bianchi, P. Pelloni, F. E. Corcione, e F. Luppino. Numerical analysis of passenger car HSDI diesel engines with the 2nd generation of common rail injection systems: The effect of multiple injections on emissions. *SAE Paper 2001-01-1068*, 2001.
- [8] G. M. Bianchi, P. Pelloni, G.-S. Zhu, e R. D. Reitz. On non-equilibrium turbulence correction in multidimensional HSDI diesel engine applications. *SAE Paper 2001-01-0997*, 2001.
- [9] G. M. Bianchi, Michelassi V., e Reitz R. D. Modeling the isotropic turbulence dissipation in engine flows by using the linear  $k-\epsilon$  model. In *Proceedings of the Fall ASME ICE International Conference*, Ann Arbor (U.S.), October 1999.
- [10] L. Bruzzone e D. F. Prieto. A technique for the selection of kernel-function parameters in rbf neural networks classification of remote-sensing images. *IEEE transactions on geoscience and remote sensing*, 37(2):1179–1184, 1999.

- [11] A. E. Catania, S. d'Ambrosio, R. Finesso, E. Spessa, G. Cipolla, e A. Vassallo. Combustion system optimization of a low compression-ratio pcci diesel engine for light-duty application, 04 2009.
- [12] Giulio Cazzoli, Claudio Forte, Cristiano Vitali, Piero Pelloni, e Gian Marco Bianchi. Modeling of wall film formed by impinging spray using a fully explicit integration method. *ASME Conference Proceedings*, 2005(ICES2005-1063):271–280, 2005.
- [13] F. E. Corcione, L. Allocca, P. Pelloni, G. M. Bianchi, e F. Luppino. Modeling atomization and drop breakup of high-pressure diesel sprays. *ASME Journal of Engineering for Gas Turbine and Power*, 123(2):419–427, apr 2001.
- [14] F. E. Corcione, E. Mattarelli, G. M. Bianchi, P. Pelloni, e F Luppino. Numerical study of the combustion chamber shape for common rail HSDI diesel engines. *SAE Paper 2000-01-1179*, 2000.
- [15] A. de Risi, T. Donateo, e D. Laforgia. Optimization of high pressure common rail electro injector using genetic algorithms. *SAE Paper 2001-01-1980*, 2001.
- [16] A. de Risi, T. Donateo, e D. Laforgia. Optimization of the combustion chamber of direct injection diesel engine. *SAE Paper 2003-01-1064*, 2003.
- [17] Z. Han, R. D. Reitz, F. E. Corcione, e G. Valentino. Interpretation of  $k-\epsilon$  computed turbulence length-scale prediction for engine flows. In *Proceedings of 26th Symposium On Combustion*, pp. 2717–2723. The Combustion Institute, 1996.
- [18] H. Hiroyasu, T. Kadota, e M. Arai. Development and use of a spray combustion modeling to predict diesel engine efficiency and pollutant emissions (part i: Combustion modeling). *Bulletin of the JSME*, 26:569–575, 1983.
- [19] T. Hiroyasu, M. Miki, J. Kamiura, S. Watanabe, e H. Hiroyasu. Multi-objective optimization of diesel engine emissions and fuel economy using genetic algorithms and phenomenological model. *SAE Paper 2002-02FFL-183*, 2002.
- [20] S.-C. Kong, Z. Han, e R. D. Reitz. The development and application of a diesel engine and combustion model for multidimensional engine simulation. *SAE 950278*, 1995.
- [21] J. Moody e C. J. Darken. Fast learning in networks of locally-tuned processing unit. *Neural Computat*, 1(2):281–294, 1989.
- [22] J. Nagle e R. F. Strickland-Constable. Oxidation of carbon between 1000-2000° C. In *Proceedings of the Fifth Carbon Conference Part 1*, pp. 265–325, 1962.
- [23] Gary D. Neely, Shizuo Sasaki, e Jeffrey A. Leet. Experimental investigation of PCCI-DI combustion on emissions in a light-duty diesel engine. *SAE PAPER 2004-01-0121*, 2004.
- [24] A. Pratab, K. Deb, S. Agrawal, e T. Meyarivan. A fast elitist non-dominated sorting genetic algorithm for multi-objective optimization: Nsga-ii. *Kangal report 200001, Indian Institute of Technology, Kanpur, India*, 2000.

- [25] P. K. Senecal e R. D. Reitz. Optimization of diesel engine emissions and fuel efficiency using genetic algorithms and computational fluid dynamics. *Eighth ICLASS, Pasadena, CA*, 2000.
- [26] P. K. Senecal, J. Xin, e R. D. Reitz. Predictions of residual gas fraction in IC engines. *SAE 962052*, 1996-10-01.
- [27] Y. Shi e R. D. Reitz. Optimization study of the effects of bowl geometry, spray targeting, and swirl ratio for a heavy duty diesel engine operated at low and high load. *International Journal of Engine Research*, 9:325–346, 2008.
- [28] K. Wagstaff, C. Cardie, S. Rogers, e S. Schroedl. Constrained k-means clustering with background knowledge. In *Proceedings of the Eighteenth International Conference on Machine Learning*, pp. 577–584, Palo Alto (U.S.), 2001.